

**MODELLING OF HEAT TRANSFER IN OPEN CELL METAL FOAMS**

By

**Edmundo Cruz Ruiz**

A thesis submitted in partial fulfillment of the requirements for the degree of

**MASTER OF SCIENCE**

**in**

**MECHANICAL ENGINEERING**

UNIVERSITY OF PUERTO RICO

MAYAGÜEZ CAMPUS

2004

Approved by:

\_\_\_\_\_  
Sandra Coutín Rodicio, Ph.D.  
Member, Graduate Committee

\_\_\_\_\_  
Date

\_\_\_\_\_  
Gustavo Gutiérrez, Ph.D.  
Member, Graduate Committee

\_\_\_\_\_  
Date

\_\_\_\_\_  
Nihad Dukhan, Ph.D.  
President, Graduate Committee

\_\_\_\_\_  
Date

\_\_\_\_\_  
Basir Shafiq, Ph.D.  
Representative of Graduate Studies

\_\_\_\_\_  
Date

\_\_\_\_\_  
Paul Sundaram, Ph.D.  
Chairperson of the Department

\_\_\_\_\_  
Date

## **ABSTRACT**

High porosity metal foams are excellent candidates for high heat dissipation. They are employed in aerospace applications mainly, but their use has been widened to include cooling in Electronic Packaging. Other important applications have been found taking advantage of the thermal properties of the metal foam. These applications include compact heat exchangers for airborne equipment, regenerative and dissipative air-cooled condenser towers, and compact heat sinks for power electronics. The low relative density, open porosity and high thermal conductivity of the cell edges, as well as the large accessible surface area per unit volume, and the ability to mix the cooling fluid, all make metal foam heat exchangers efficient, compact and light weight. The purpose of this work is to provide an analytical model to determine the two-dimensional temperature distribution in open cell metal foams when they are used in a forced convective heat transfer mode. The analysis uses the typical parameters reported by the foam manufacturers such as the porosity and the area density, defined as the ratio of the surface area of the foam to the volume. The simplicity and applicability of the present approach offer a significant advantage over previous models. It eliminates the need for complex microscopic analytical or numerical modeling of the flow and the heat transfer in and around the pores. The correlations obtained experimentally through this research also have a great importance in the model proposed.

## RESUMEN

Las esponjas de metal altamente porosas son candidatos excelentes para generar gran disipación de calor. Son empleadas en la industria aeroespacial principalmente, pero su uso ha ido ampliándose para enfriamiento en dispositivos electrónicos. Se han encontrado aplicaciones importantes aprovechando las propiedades térmicas de las esponjas de metal. Estas aplicaciones incluyen intercambiadores de calor compactos para equipos de aire, torres condensadoras enfriadas por aire de tipo regenerativo y disipativo, y sumideros de calor compactos para electrónica de potencia. La baja densidad relativa, porosidad abierta y alta conductividad térmica de los bordes de la celda, así como la gran área superficial por unidad de volumen y su habilidad para mezclar el fluido refrigerante, todo junto hacen que los intercambiadores de calor creados con esponja de metal sean eficientes, compactos y de bajo peso. El propósito de este trabajo es proveer un modelo analítico para determinar la distribución de temperatura en dos dimensiones en esponjas de metal de celdas abiertas cuando son usadas en un modo de transferencia de calor por convección forzada. El análisis usa los parámetros típicos reportados por los fabricantes de la esponja de metal tales como porosidad y densidad de área, definida como la razón de área superficial de la esponja al volumen de la misma. La simplicidad y aplicabilidad de la presente aproximación ofrece significantes ventajas sobre modelos previos. Este análisis elimina la necesidad de modelación analítica a nivel microscópico o modelación numérica compleja del flujo y transferencia de calor en y alrededor de los poros. Las correlaciones obtenidas experimentalmente a través de esta investigación también tienen una gran importancia en el modelo propuesto.

## **DEDICATION**

To my parents, sisters and Esther, the most important persons in my life

## **ACKNOWLEDGMENTS**

I would like to say thanks to Dr. Nihad Dukhan, my research advisor, for his advice and encouragement throughout this research as well as to the Mechanical Engineering Department of the University of Puerto Rico for providing me with the theoretical background and financial support to develop this research.

## TABLE OF CONTENT

List of Tables.....	viii
List of Figures.....	ix
Nomenclature.....	xiii
CHAPTER 1. Introduction.....	1
1.1 Background.....	1
1.2 Applications.....	5
1.3 An Overview of the Research.....	7
CHAPTER 2. Literature Review.....	9
CHAPTER 3. Analytical Modeling.....	19
3.1 Justification for the foam local average temperature.....	19
3.2 Heat transfer model.....	29
3.3 Proposed boundary conditions at the foam exit.....	33
3.3.1 Temperature distribution with linear behavior.....	33
3.3.2 Temperature distribution with exponential behavior.....	36
3.3.3 Temperature distribution for a one dimensional model of Dukhan and Quiñones.....	37
3.3.4 Temperature distribution with zero-slope.....	39
CHAPTER 4. Experimental Work.....	41
4.1 Materials and equipment.....	41
4.1.1 Metal foam sample.....	41

4.1.2 Wind tunnel .....	44
4.1.3 Heaters.....	47
4.1.4 Power supplies.....	48
4.1.5 Data acquisition system.....	49
4.2 Experimental methodology.....	52
4.2.1 Average tunnel velocity measurement.....	52
4.2.2 Temperature measurements .....	55
4.3 Uncertainty analysis.....	58
4.3.1 Uncertainty in length.....	58
4.3.2 Uncertainty in air velocity.....	59
4.3.3 Uncertainty in temperature.....	62
CHAPTER 5. Results and Comparisons.....	66
5.1 Comparisons between experimental results and analytical solutions.....	66
5.2 Determination of the parameter M variation along the z direction.....	83
5.3 Simplified semi-analytical solution for the temperature field in metal foam.....	90
CHAPTER 6. Conclusions and Recommendations.....	98
References.....	101
APPENDIX A.....	104
APPENDIX B.....	111

## LIST OF TABLES

Table 2.1. Literature Review Summary Table.....	18
Table 3.1. Temperature difference between the surface filament and the air at one inch from the entrance.....	29
Table 4.1. Average velocity in the wind tunnel for each flow rate.....	55
Table 4.2. Thermocouple locations.....	57
Table 5.1. Flow rates and air velocity.....	67
Table 5.2. Coefficient $a_{jm}$ for different flow rates.....	85

## LIST OF FIGURES

Figure 1.1. Actual foam structure.....	2
Figure 1.2. Representation of metal foam cell.....	2
Figure 1.3. 10, 20 and 40 PPI metal foam samples.....	3
Figure 1.4. Compact heat exchanger using metal foam.....	6
Figure 3.1. Metal foam representations.....	20
Figure 3.2. Tube arrangements in a bank.....	21
Figure 3.3. Analyzed metal foam zone and representation as a bank of cylinders.....	26
Figure 3.4. Bank of cylinders arrangements to model metal foam.....	28
Figure 3.5. Foam dimensions and heat flow directions.....	30
Figure 3.6. Control volume defined inside metal foam.....	31
Figure 3.7. Two-dimensional model.....	34
Figure 3.8. Superposition applied to the model (linear case).....	35
Figure 3.9. Superposition applied to the model (exponential case).....	36
Figure 3.10. Superposition (case of the 1D model boundary condition).....	38
Figure 3.11. Two-dimensional model for the zero slope case.....	40
Figure 4.1. Metal foam sample.....	42
Figure 4.2. Foam sample dimensions and coordinate system.....	42
Figure 4.3. Wind tunnel.....	45
Figure 4.4. Diagram of wind tunnel.....	46

Figure 4.5. Diagram of Pitot tube.....	47
Figure 4.6. Heaters.....	48
Figure 4.7. Power supplies.....	49
Figure 4.8. Data acquisition system.....	52
Figure 4.9. Pitot tube.....	53
Figure 4.10. Velocity measurement methodology.....	54
Figure 4.11. Schematic of the experimental set-up.....	56
Figure 5.1. Variation of the temperature distribution along z direction for $Re=84.735$ ...	67
Figure 5.2. Variation of the temperature distribution along z direction for $Re=27.378$ ...	68
Figure 5.3. Variation of the temperature distribution for different Reynolds numbers at 1 inch from the entrance.....	69
Figure 5.4. Variation of the temperature distribution for different Re at 3.75 inches from the entrance.....	70
Figure 5.5. Two-dimensional plot of proposed solutions.....	71
Figure 5.6. Comparison between analytical and experimental data for $Re=84.375$ at 1 inch from the entrance (first boundary condition case).....	73
Figure 5.7. Comparison between analytical and experimental data for $Re=27.378$ at 1 inch from the entrance (first boundary condition case).....	74
Figure 5.8. Comparison between analytical and experimental data for $Re=84.735$ at 2 inches from the entrance (first boundary condition case).....	75
Figure 5.9. Comparison between analytical and experimental data for $Re=27.378$ at 2 inches from the entrance (first boundary condition case).....	76

Figure 5.10. Comparison between analytical and experimental data for $Re=84.735$ at 3 inches from the entrance (first boundary condition case).....	77
Figure 5.11. Comparison between analytical and experimental data for $Re=27.378$ at 3 inches from the entrance (first boundary condition case).....	77
Figure 5.12. Comparison between analytical and experimental data for $Re=27.378$ at 3 inches from the entrance (second boundary condition case).....	78
Figure 5.13. Comparison between analytical and experimental data for $Re=27.378$ at 3 inches from the entrance (third boundary condition case).....	79
Figure 5.14. Comparison between analytical and experimental data for $Re=27.378$ at 3 inches from the entrance (fourth boundary condition case).....	79
Figure 5.15. Comparison between analytical and experimental data for $Re=27.378$ at 3.75 inches from the entrance (first boundary condition case).....	80
Figure 5.16. Comparison between analytical and experimental data for $Re=27.378$ at 3.75 inches from the entrance (second boundary condition case).....	81
Figure 5.17. Comparison between analytical and experimental data for $Re=27.378$ at 3.75 inches from the entrance (third boundary condition case).....	82
Figure 5.18. Comparison between analytical and experimental data for $Re=27.378$ at 3.75 inches from the entrance (fourth boundary condition case).....	82
Figure 5.19. Plot of the analytical solution (fourth case) data for $Re=27.378$ .....	83
Figure 5.20. Plot of the analytical solution (fourth case) with the parameter $M$ varying along the $z$ direction.....	86
Figure 5.21. Comparison between analytical and experimental data for $Re=27.378$ at 1 inch from the entrance (fourth boundary condition case with $M(Z)$ ).....	87

Figure 5.22. Comparison between analytical and experimental data for $Re=27.378$ at 2 inches from the entrance (fourth boundary condition case with $M(Z)$ ).....	88
Figure 5.23. Comparison between analytical and experimental data for $Re=27.378$ at 3 inches from the entrance (fourth boundary condition case with $M(Z)$ ).....	88
Figure 5.24. Comparison between analytical and experimental data for $Re=27.378$ at 3.75 inches from the entrance (fourth boundary condition case with $M(Z)$ ).....	89
Figure 5.25. Comparison between semi-analytical and experimental data for $Re=84.375$ at 1 inch from the entrance.....	93
Figure 5.26. Comparison between semi-analytical and experimental data for $Re=84.375$ at 2 inches from the entrance.....	94
Figure 5.27. Comparison between semi-analytical and experimental data for $Re=84.375$ at 3 inches from the entrance.....	94
Figure 5.28. Comparison between semi-analytical and experimental data for $Re=84.375$ at 3.75 inches from the entrance.....	95
Figure 5.29. Comparison between semi-analytical and experimental data for $Re=27.378$ at 1 inch from the entrance.....	95
Figure 5.30. Comparison between semi-analytical and experimental data for $Re=27.378$ at 2 inches from the entrance.....	96
Figure 5.31. Comparison between semi-analytical and experimental data for $Re=27.378$ at 3 inches from the entrance.....	96
Figure 5.32. Comparison between semi-analytical and experimental data for $Re=27.378$ at 3.75 inches from the entrance.....	97

## NOMENCLATURE

$a_{fm}$	coefficient found from experiments to set boundary condition
$A_c$	total cross sectional area
$A_{cond}$	area for heat transfer by conduction
$A_{cond(x)s}$	area for heat conduction in the x direction (solid part)
$A_{cond(x)f}$	area for heat conduction in the x direction (fluid)
$A_{cond(z)s}$	area for heat conduction in the z direction (solid part)
$A_{cond(z)f}$	area for heat conduction in the z direction (fluid)
$A_p$	area occupied by the pores.
Bi	Biot number
$c_p$	specific heat at constant pressure for air
$d$	filament diameter
$dx$	height of the control volume
$dz$	thickness of the control volume
$D$	cylinder diameter in a bank of cylinders
$g$	gravitational acceleration
$h$	elevation in a Bernoulli equation
$h_{fm}$	convection heat transfer coefficient inside the pores
$k_s$	conductivity coefficient for solid part
$k_f$	conductivity coefficient for fluid
$L$	length of foam sample

$m_{fm}$	foam parameter
$m_{foam}$	mass of foam sample
$M$	dimensionless foam parameter
$N$	number of cylinders in a bank
$N_T$	number of cylinders in the transverse direction of a bank
Nu	Nusselt number
$p_d$	dynamic pressure
$p_e$	static pressure
$p_0$	stagnation pressure
PPI	number of pores per inch
Pr	Prandtl number
$q_{conv}$	heat transferred by convection in the foam sample
$q_x$	conduction heat flux in the x direction
$q_z$	conduction heat flux in the z direction
Re	Reynolds number in the pores
$S_T$	transverse pitch in a bank of cylinders
$S_L$	longitudinal pitch $S_L$ in a bank of cylinders
$t$	thickness of foam sample
$T_b$	temperature at the base of the foam
$T_{fm}$	average temperature in the foam
$T_i$	temperature of fluid at the entrance of a bank of cylinders
$T_o$	temperature of fluid at the exit of a bank of cylinders

$T_s$	temperature of cylinder surface in a bank of cylinders
$T_\infty$	temperature of the fluid
$u$	average pore velocity
$u_0$	zero-order uncertainty
$u_B$	uncertainty in terminal block
$u_c$	uncertainty in calibration
$u_L$	uncertainty in length
$u_{pd}$	uncertainty in dynamic pressure
$u_U$	uncertainty in air velocity
$u_T$	uncertainty in temperature
$u_{Th}$	uncertainty in thermocouple
$U$	fluid velocity inside the wind tunnel
$\nu$	kinematic viscosity of the fluid
$V_{air}$	volume of the air inside the foam sample
$V_{foam}$	volume of the foam sample
$V_{ss}$	volume of solid part of the sample
$W$	width of foam sample
$x$	axial direction along the foam sample
$X$	dimensionless axial direction along the foam sample
$z$	fluid flow direction trough the foam sample
$Z$	dimensionless fluid flow direction trough the foam sample

### Greek symbols

$\alpha$	thermal diffusion coefficient of the fluid
$\varepsilon$	porosity = $1 - \left(\frac{V_s}{V_{tot}}\right)$
$\lambda$	coefficient determined by experimentation to correct $h_{fm}$
$\theta_{fm}$	dimensionless temperature in the foam = $\frac{T - T_\infty}{T_b - T_\infty}$
$\rho$	relative density of foam = $\rho_{fm}/\rho_s$
$\rho_a$	density of the air
$\rho_{foam}$	density of the foam sample
$\rho_{material}$	density of the base material of the foam sample
$\sigma$	surface area per unit volume of foam
$\Psi$	auxiliary temperature variable used in the superposition model
$\Phi$	auxiliary temperature variable used in the superposition model
$\eta_n$	eigenvalues of the temperature equation
$\kappa$	auxiliary temperature variable used in the separation of variables solution
$\chi$	auxiliary temperature variable used in the separation of variables solution

# **CHAPTER 1**

## **INTRODUCTION**

### **1.1 BACKGROUND**

Metal foams are a relatively new class of materials with low densities and novel thermal, mechanical, electrical and acoustic properties. They are used to construct lightweight structures, to develop energy absorption devices and for thermal applications, which is the focus of this thesis. Also, they are recyclable and nontoxic. At present, metal foams have not been completely characterized, and the processes to manufacture them are imperfectly controlled, therefore the properties of the metal foams suffer variability. However, all these issues are improving rapidly.

Metal foams consist of small filaments that are continuously connected in an open-celled foam structure. The strength of the foam depends mostly on the base material and the relative density of the foam. Other properties, such as pore size, filament size, and cell shape influence certain foam characteristics, such as the heat transfer through them. In order to define a foam material for an application, it is necessary to specify two characteristics; pore size and relative density. These characteristics are independent foam variables which provide great flexibility in product design. Figure 1.1 is a picture of the metal foam structure similar the one used in this research.

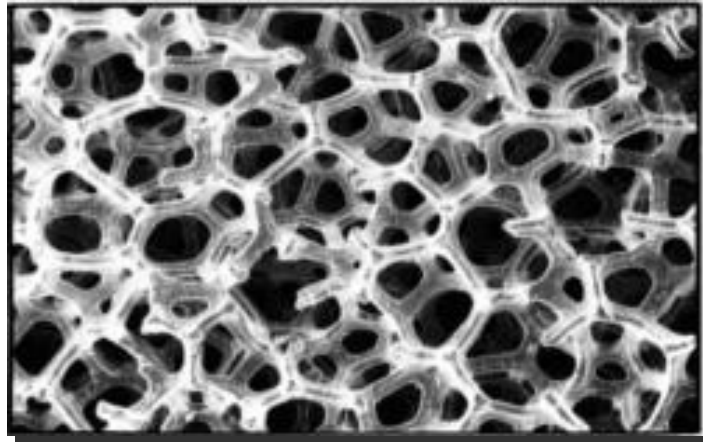


**Figure 1.1 Actual foam structure.**

The cells of metal foam are conformed by polyhedrons of 12 to 14 faces. Likewise, each face has a pentagonal or hexagonal shape, and therefore, each one is formed by five or six filaments. Figure 1.2 is a very simple representation of the metal foam cell described above.

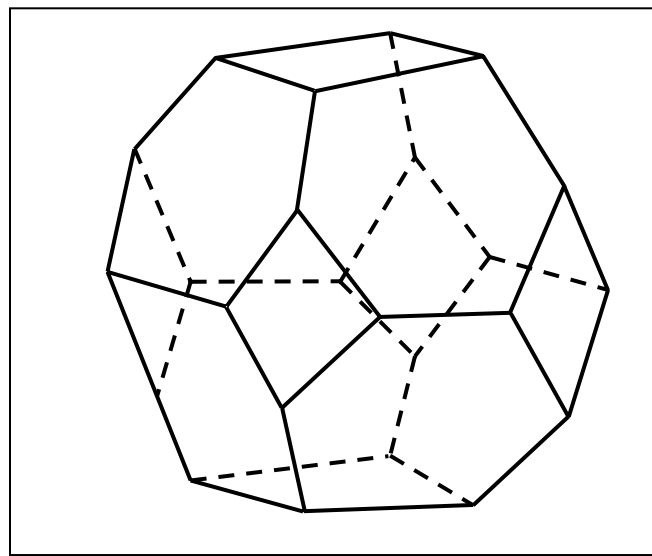


**Figure 1.2 Representation of metal foam cell.**

The most important characteristic of the metal foams, the pore size, is defined by the diameter of the open window in each of the faces that compose the cell. The pore density is the number of pores that can be measured in a linear inch and its unit is PPI (pores per linear inch). The available pore densities vary depending upon the base foam material, but their overall uncompressed range is 5-100 PPI. Figure 1.3 shows some samples of open-cell metal foams of different densities.



**Figure 1.3 10, 20 and 40 PPI metal foam samples.**

The second most important characteristic, the relative density, is defined as a percentage (%) of solid material. In other words, it is the volume of solid foam material relative to the total volume of metal foam. It is known that when the relative density is increased, the filaments become larger in diameter and stronger, increasing the strength of the foam structure.

Most commercially available metal foams are based on aluminum or nickel. Our research uses open-cell aluminum foam. This kind of metal foam will be better described in Section 4.1.

The focus of this thesis is the study of the heat transfer through a commercially available metal foam sample. As it was explained before, metal foam is composed of a porous matrix that consists of tortuous, irregular shaped flow passages. Heat transfer takes place between the surface of the solid matrix and the fluid. The flow re-circulates at the back of the solid fibers. Turbulence and unsteady flows occur when a Reynolds number greater than 100 is presented in the pore-scale. Due to the geometric complexity and the random orientation of the solid phase of the porous medium, the exact solutions of the transport equations inside the pores are difficult to obtain.

A number of studies were undertaken to try to characterize metal foams. Next Chapter presents a literature review that was made at the earlier stages of this research. This review summarizes a lot of works that compose a contribution to the concurrent development of the science and uses of the metal foams.

The present work provides an analytical model to determine the two-dimensional temperature distribution in open cell metal foams when they are used in a forced convective heat transfer mode. Two of the most important characteristics of the metal foams were mentioned before. However, there exist other typical parameters reported by the foam manufacturers such as the porosity and the area density, which are used in the

analysis. The area density is defined as the ratio of the surface area of the foam to the volume. The simplicity and applicability of the present approach offer a significant advantage over previous models. It eliminates the need for rigorous microscopic analytical or numerical modeling of the flow and the heat transfer in and around the pores. Another advantage is that the current model is easily verified by simple experiments, as described in Chapter 4.

## **1.2 APPLICATIONS**

Metal foams have been used as lightweight supporting structure in aerospace applications, especially in the cryogenic field [1, 2]. Different types of metal foams are used as cladding on buildings, strain isolation and as a buffer between a stiff structure and a fluctuating temperature field. They are also used in geothermal operations and in petroleum reservoirs [15]. Ceramic foams are used in advanced burners and heat pipes. And nickel foams have been used to improve the performance of high-power batteries, such as those used in lightweight cordless electronics [14]. Thermal management applications of foams include compact heat exchangers for airborne equipment, air-cooled condenser towers, both the regenerative and the dissipative type, and compact heat sinks for power electronics [4]. The open porosity, low relative density and high thermal conductivity of the cell edges, the large accessible surface area per unit volume, and the ability to mix the cooling fluid by promoting eddies [8]; all make metal foam heat exchangers efficient, compact and light weight.

Focusing on the open-cell foams made out of metal, especially aluminum; it is found that they have been used to construct fluid flow control devices as gas diffusers and mixers as well as separators of liquid and gas. The capacity of the metal foams to absorb a great quantity of energy produced by impact when they are used in materials type sandwich is well known. So, the stress-strain response of metal foams can be customized for some specific applications varying the density and alloy of the foam, while its isotropic properties provide identical response without considering the impact angle.

As previously mentioned, one of the most important applications of the aluminum metal foams is to build compact heat exchangers. The high surface area to volume ratio allows a more compact design than provided by any other materials. A compact heat exchanger made using aluminum metal foam can be observed in Figure 1.4.



**Figure 1.4 Compact heat exchanger using metal foam.**

### **1.3 AN OVERVIEW OF THE RESEARCH**

This research consists of the study of the temperature distribution in open-cell metal foams when these foams are in a convective heat transfer mode. A mathematical model is developed and validated with experimental work. The whole research work has been divided into several parts to achieve the objectives. The first part of the research consists of a literature review of the works related to this research topic. This has a great value because it allows getting a strong background in the topic.

A two-dimensional analytical heat transfer model is developed and some solutions are obtained for different conditions. A justification to consider a local average temperature between the solid and fluid parts inside the metal foam is given, and correlations developed by different authors in some related works are used in the mathematical model. Boundary conditions in the model will be carefully determined because the temperature behavior at the face where the air exits the foam is unknown. Thus, four different mathematical solutions will be obtained varying the boundary conditions at the face where the air exits the foam. All the details of these mathematical solutions are given in the Chapter 3 and Appendix B.

To validate the analytical model and to find the real boundary condition at the exit of the foam, a series of experiments is carried out using a sample of open cell aluminum foam and a heater attached to it. To perform these experiments, a wind tunnel and a data acquisition system was employed. The heater generates a constant heat flux at the base of

the foam which is conducted along the filaments of the foam and through the air. The foam is located inside the wind tunnel in order to pass air through it. When the air passes through the metal foam, heat transfer by convection from the filaments to the air begins to happen and the heat is dissipated in a very small space along the axial direction. This information is revealed by employing some thermocouples to measure the actual temperature distribution in the metal foam along two directions. All the details about the foam and the equipment employed for the experimental work are given in Chapter 4.

Once the mathematical model has been developed and the experiments are run, the next step is to compare the results generated and to analyze if these have a good agreement. It was useful to find a mathematical model that could be adjusted to the experiments and to develop some interesting conclusions.

## **CHAPTER 2**

### **LITERATURE REVIEW**

Heat transfer in porous media is an interesting topic which has been studied in the recent years. Literature review indicates that some investigators have tried to find an effective conductivity coefficient considering the two elements present in the foam: solid aluminum and air as a single phase. Experimental, analytical and numerical works about the topic of porous media has been carried out.

In 1998, Bastawros [1] demonstrated the efficiency of metallic foams in forced convection heat removal. Bastawros showed that a high performance cellular aluminum heat sink removed 2-3 times the usual heat flux removed by a pin-fin array, at a third of the weight and with only a moderate increase in the pressure drop. When the air flow was at low velocities, the heat flux was governed by the convective heat transfer to the flowing fluid. At higher velocities, the heat flux was limited by heat conduction from the substrate to the foam block through the constricted nodal passages of the foam.

An important application of metal foams, as it has been mentioned in multiple occasions, is to construct compact heat exchangers. An interesting study carried out by Boomsma et al. [2] where open-cell aluminum foams were compressed by various factors and then fashioned in to heat exchangers for electronic cooling applications, which dissipate large amounts of heat. Some parameters that describe the heat exchangers were evaluated through experiments, which included the hydraulic characterization, the heat transfer performance and a study to determine the most efficient heat exchanger for

particular heat transfer necessities. It was seen that the compressed aluminum foams made a significant improvement in the efficiency over several commercially available heat exchangers, which operate under nearly identical conditions.

Zhao et al. [3] studied the dependence of the effective thermal conductivity on the temperature in metal foams. In their work, the effective thermal conductivity of five FeCrAlY foam samples with different pore sizes and relative densities were measured using a guarded-hot-plate apparatus under both vacuum and atmospheric conditions. The results showed that the effective thermal conductivity increased rapidly as the temperature increased, particularly in the higher temperature range (500-800 K) where the thermal radiation dominated the transport. The results showed that the contribution of the heat transfer by natural convection was also significant. The effective thermal conductivity increased as the pore size or relative density increased. In addition, relative density had a great effect on the natural convection in the metal foam.

Some purely analytical works has been developed. Between the first works of this kind we found the one developed by Vafai and Tien [4] who showed the nature and importance of the boundary and inertial effects upon flow and heat transfer in porous media. The effect of the boundary on the heat transfer was quite important and more pronounced for the thermal boundary layer with a thickness less than or of the same order as the momentum boundary layer.

Writz [5] developed a semi-empirical model for the combined conduction and convection heat transfer in a thin porous wall. The model assumed a one-dimensional

conduction in the porous matrix and a one-dimensional flow of the coolant through the foam wall. For the same volume of the heat exchanger, the porous matrix provided approximately 1.5 times more heat transfer surface than the offset strip fin array.

Lu et al. [6] studied the use of open-celled metal foams as heat sinks for high power electronic devices and multi-layered heat exchangers for aeronautical applications. An analytical model was developed with simple cubic unit cells consisting of heated slender cylinders, based on existing heat transfer data on convective cross flow through cylinders banks. A foam-filled channel having constant wall temperatures was analyzed to obtain the temperature distribution inside the channel as a function of foam density, cell size and other heat transfer parameters. The overall heat transfer coefficient of the heat exchanging system was calculated, and the pressure drop experienced by the fluid flow was obtained.

A purely numerical work also was found. Regarding the improvement the heat transfer using porous media as heat sinks, Kiwan and Al-Nimr [7] numerically simulated the thermal performance of porous fins. They established a comparison between their performance and that of solid fins. It was found that using porous fins may enhance the performance of an equal size conventional solid fin and, as a result, save one hundred percent of the fin material. This model was used to study the effect of several operating and design parameters on the thermal performance of the fin, like the Rayleigh number, Darcy number and the thermal conductivity ratios.

It is obvious that analytical and numerical methods to model the heat transfer in porous media validated experimentally composes the biggest group of works related to the topic. First, a description of the works that involves numerical models validated experimentally will be given.

Younis and Viskanta [8] designed an apparatus to determine the volumetric heat transfer coefficient between a stream of air and ceramic foam. The governing conservation equations of energy for both the gas and the solid phases with appropriate boundary conditions were solved using a finite-difference procedure. Heat transfer correlations were developed for each different mean pore diameter of ceramic foam and for different values of air velocity entering to the foam sample.

Decker et al. [9] provided detailed experimental characterization and numerical modeling of the heat and mass transport properties of highly porous media for solar receivers and porous burners. They considered the foam as a pseudo-homogeneous (locally-volume-averaged) medium, where the solid and the fluid phases were treated as an artificial single phase with effective properties.

Calmidi and Mahajan [10] quantify thermal dispersion and thermal non equilibrium effects in metal foams. To this end, both experimental and numerical methods were employed. Experiments were performed with a variety of aluminum metal foams. Their results indicated that for foam-air combinations, the thermal dispersion was extremely low. However, for foam-water combinations, results indicated that the thermal dispersion was very high.

Phanikumar and Mahajan [11] performed numerical and experimental studies for flows in high porosity metal foam heated from below. Experiments were conducted under natural convection for the same configuration and these were used to test the numerical model, and the validity of the thermal equilibrium assumption for metal foams. Several metal foam-fluid combinations were used to study the heat transfer enhancement relative to the base in which there was no metal foam but only a heated plate. Thermal dispersion effects and the effect of Darcy number on heat transfer were reported.

Related to the non-metallic foams, some numerical-experimental works were also founded and reviewed, as the developed by Pan et al. [12], who presented experimental investigations on the effective heat conductivity of ceramic foams. Guessing the radial and axial effective heat conductivities, the temperature profiles in the porous media were solved under local averaged temperature assumption using a finite-volume code. The best combination of radial and axial effective heat conductivities was found when the minimal error, based on the least-squares method, between the measured and two-dimensionally simulated temperature fields were reached.

Sullines and Daryabeigi [13] measured the thermal conductivity of this kind of foam for a pressure difference range of  $10^{-4}$  to 750 mm Hg. They developed a numerical model to predict the behavior of the effective thermal conductivity at various temperatures and pressures. When numerical results and experimental values were compared, they realized that numerical values required the introduction of a conducting coupling term to the gas/solid conduction model in order to have a good approach. When

the coupling term was introduced, calculated values corresponded to within an average of nine percent to the experimental values.

The most similar works to ours, this is, these that includes analytical models validated experimentally will be mentioned next. Zumbrunnen et al. [14] made several experimental studies using porous solids with complex internal geometries. They developed a thermal conductance model for the heat transfer in the porous solid. They also designed an apparatus to measure the overall thermal conductances of porous solids over a wide temperature range. Good agreement between the model and the experiments was determined. It was also found that when radiation is significant, the overall thermal conductance increased with the temperature difference across the porous solid, and was independent of thickness, when the thickness is much larger than the characteristic pores size.

Hunt and Tien [15] demonstrated the increase in heat transfer with thermal dispersion. The model developed a relation for the dispersion by equating the dispersion conductivity to a product of the velocity, square root of the permeability and an experimental constant determined from seven different pieces of fibrous media.

In 1999, Bastawros et al. [16] performed some experiments using open cell foams attached to an aluminum substrate and subject to a cross flow of air. The foam thermal performance was characterized through sets of steady-state experimental measurements. The thermal measurements were correlated with models of the thermal dispersion in porous media. These correlations revealed that the filaments normal to the flow direction

transmitted most of the heat flux. It is important to notice that these correlations were used in the analytical model developed in this thesis. In their work, Bastawros et al. also conducted some hydraulic measurements to study the pressure drop through the foam sample.

Boomsma, K. and Poulikakos, D. [17] developed a one-dimensional heat conduction model for open celled metallic foams. It was based on a three dimensional description of the foam geometry. It demonstrated that for metallic foams, in which the solid conductivity is markedly higher than the fluid conductivity, improvements in the overall effective thermal conductivity are best made by increasing the thermal conductivity of the solid phase through manipulation of the foam solid structure at the manufacturing phase, since the solid phase appeared to govern the effective thermal conductivity value, even at a very high porosity.

Ozmat et al. [18] developed analytical and experimental studies to characterize the structural and thermal properties of Retriculated Metal Foams (RMF) based heat exchangers. It was pointed out that increasing the as fabricated specific density of the foam by successive compression steps was one of the key features of the RMF based heat exchanger technology.

Bhattacharya et al. [19] provided analytical and experimental results for the effective thermal conductivity for high porosity metal foams. The analytical model represented the foam by a two-dimensional array of hexagonal cells. The porosity and the pore density were used to describe the porous media. Experimental data with

aluminum foams using air and water as the fluid media were used to validate the analytical solutions.

Continuing with their work, Bhattacharya and Mahajan [20] carried out an interesting research which was presented in their paper “Finned metal foam heat sinks for electronics cooling in forced convection”. These heat sinks can be thought to be similar to longitudinal finned heat sinks where the air gap between two adjacent fins is replaced by high porosity metal foams. Experiments were conducted on aluminum foams of 90 percent porosity and pore density corresponding to 5 and 20 PPI. The forced convection results showed that the heat transfer was considerably enhanced when fins were incorporated in metal foams.

Dukhan and Quinones [21] used a one-dimensional heat transfer model for open-cell metal foam. Aluminum foams with different areas, relative densities, filament diameters, and number of pores per inch were analyzed. They found that the effective thermal conductivity of the foams can be up to four times higher than that of solid aluminum and that the heat transfer can be improved by a factor of 1.5. The maximum heat transfer for the aluminum foam occurred at a pore Reynolds number of 52.

All the literature reviewed is about thermal and hydraulic characterization of porous media in natural and forced convective flow conditions. However, at the moment there are not any universal correlations to characterize the porous media due to the great variability of geometry and the materials of which they are constructed. The base material of the porous media can be metallic and non-metallic. These reasons in addition to the

flow conditions under which porous media are put to work generate different thermal and hydraulic behaviors. This thesis gives a novelty way not addressed in the past to characterize the thermal behavior of aluminum metal foams using a model of one equation to predict the temperature distribution of the solid and fluid phases present inside the foam. This equation is easy to solve and the temperature distribution generated by it can be used to calculate some effective parameters in this kind of materials that could be used as design parameters in thermal applications where metal foam is used.

<b>Author</b>	<b>Type of Model</b>	<b>Relevant Parameters</b>
Boomsma, K et al. (2003)	Open cell metal foams into heat exchangers	Hydraulic characterization, Heat transfer performance
Boomsma, K et al. (2000)	Steel alloy foams in guarded-hot-plate apparatus	Effective thermal conductivity (steel alloy foams)
Lu et al. (1997)	Model of foam as simple cubic unit cells	Overall heat transfer coefficient, pressure drop of fluid flow
Calmidi V. V. et al. (2000)	Numerical study, semi-empirical volume-averaged form of governing equations	Thermal dispersion conductivity, interstitial heat transfer coefficient
Bastawros, A.F. et al. (1999)	Model of thermal dispersion in porous media subjected to local volume averaging	Foam thermal performance, foam morphology influence, hydraulic characterization
Boomsma, K et al. (2000)	1-D heat conduction based on a three dimensional description of metal foam	Effective thermal conductivity
Bhattacharya, A. et al. (2001)	2-D array of hexagonal cells where the fibers form the sides of the hexagons	Effective thermal conductivity, permeability, inertial coefficient
Bhattacharya, A. et al. (2002)	Empirical correlation for Nusselt number in terms of Peclet number	Heat transfer coefficient, pressure drop
Dukhan, N. et al (2003)	1-D model for conduction and convection in open cell metal foams	Effective conductivity, Reynolds number
Present Work	2-D model for conduction and convection in open cell metal foams	Effective conductivity, Reynolds number

**Table 2.1 Literature Review Summary Table**

## **CHAPTER 3**

### **ANALYTICAL MODELING**

The objective of this Chapter is to present a justification for assuming a local averaged temperature in open cell metal foams. Also, it presents the mathematical procedure followed to obtain solutions that could provide an accurate representation of the heat transfer through the foam.

#### **3.1 JUSTIFICATION FOR THE FOAM LOCAL AVERAGE TEMPERATURE**

Heat transfer in porous media has been generally studied under the assumption of local averaged temperature among the two phases present in the medium: fluid and solid. We know that temperature of solid phase and temperature of fluid phase are never exactly equal, but the assumption is taken in order to facilitate the modeling of the heat transfer in the metal foams. A strong reference to consider this assumption as valid is the work developed by Dae-Young Lee et al. [22] in which a validation of the local averaged temperature assumption is carried out based in physical parameters of the metal foams and physical conditions under which they work. Some works mentioned in the literature review used two separate energy equations to model the temperature in each. In this thesis, like in other research works, a single homogenous equation is used to describe the heat transfer under the assumption that the solid and fluid phases have the same local temperature. Keeping in mind that the main goal of this thesis is to find a simple method

to model the heat transfer in metal foams, only one transport equation is proposed. But, what is the justification to do it? Below, some arguments will be given to justify such assumption.

In the literature related to heat transfer in porous media, various ways to represent the metal foam structure are found with the purpose of studying its thermo-physical properties. For example, Bhattacharya [19] proposed a representation of the foam structure (Figure 3.1 (a)) as an array of cubes of unit volume, as shown in Figure 3.1 (b). Holman [24] considered the metal foam structure as a bank of cylinders (Figure (c)), and it will be the array that we will use in our model.

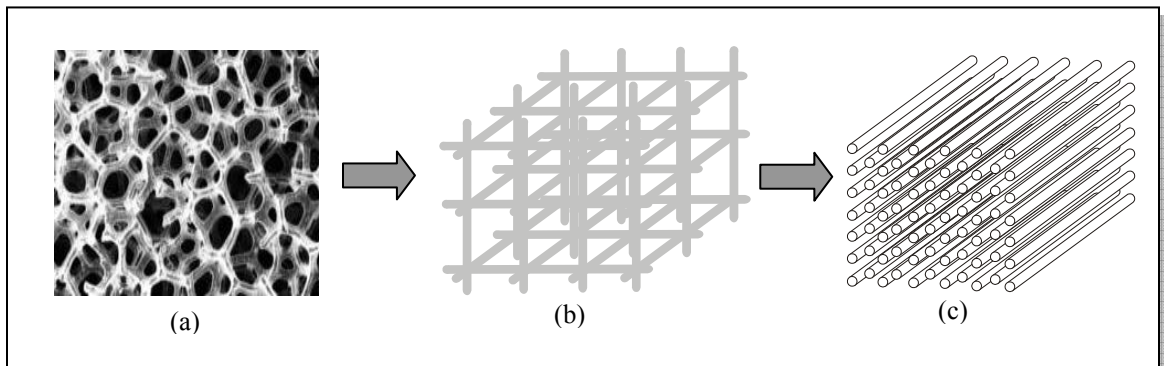


**Figure 3.1 Metal Foam Representations. (a) Actual metal foam structure. (b) Metal foam as an arrangement of cubes. (c) Metal foam as a staggered bank of cylinders.**

Figure 3.1 (c) is the model for the foam structure that is adopted in this work. For the bank of cylinders, there exists an extensive set of correlations. Some of these correlations are used to explain why the temperature of the solid and the fluid can be

considered the same. At the same time, they are used to find the convective heat transfer coefficient  $h_{fm}$  inside the foam structure.

The cylinders of a bank are either staggered or aligned in the direction of the fluid velocity  $U$ . The configuration is characterized by the cylinder diameter  $D$  and by a transverse pitch  $S_T$  and longitudinal pitch  $S_L$ , measured between cylinder centers. Figure 3.2 show all the physical characteristics mentioned. Let  $T_\infty$  represents the temperature of the fluid when it enters the bank of cylinders and it rapidly increases until it almost reaches the surface temperature of the cylinders. Since the random structure of the foam, a staggered bank of cylinders is considered in this work.

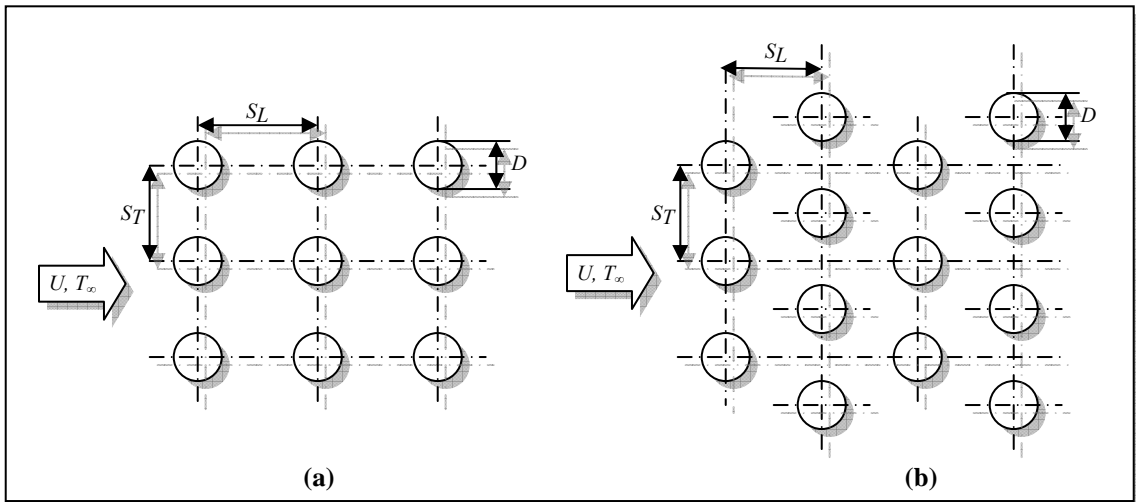


**Figure 3.2 Tube arrangements in a bank. (a) Aligned. (b) Staggered.**

First, the fluid velocity  $U$  must be known. This is an input data that is used to calculate the average pore velocity. The fluid velocity is known through experiments; these experiments will be described in the next Chapter. Correlations developed by

Bastawros [16] have an important role in the development of the heat transfer equations of this thesis. He proposes an average pore velocity,  $u$ , in an open cell metal foam sample defined as,

$$u = \frac{U}{1 - \rho} \quad (3.1)$$

where,  $\rho$  represents the relative density of the foam sample. Once the average pore velocity has been calculated, it is used to calculate the Reynolds number in the pores.

$$\text{Re} = \frac{ud}{\nu} \quad (3.2)$$

where  $d$  is the filament diameter and  $\nu$  is the kinematic viscosity of the fluid. It is important to note that the filament diameter is the characteristic length for the bank of cylinders. An important parameter in the study of convection heat transfer is the Nusselt number  $Nu$ . The Nusselt number ( $Nu$ ) is equivalent to the dimensionless temperature gradient at the surface, and it provides a measure of the convective heat transfer occurring at the surface.

$$Nu = \frac{h_{fm}d}{k_f} \quad (3.3)$$

where  $k_f$  is the fluid thermal conductivity of the fluid and  $h_{fm}$  is the convective heat transfer coefficient inside the foam structure.

The Nusselt number is experimentally correlated with the flow conditions using power law relations. This is done for a wide range of porous media, specially packed beds of spherical particles and ordered banks of cylinders. For airflow across tube bundles composed of 10 or more rows, Grimison [23] has obtained a correlation of the form,

$$Nu = C_1 Re^m$$

where  $C_1$  and  $m$  depend on the physical parameters of the bank, like the transverse and longitudinal pitches. More recent results have been obtained by Zhukauskas [23], who proposed the following correlation.

$$Nu = C Re^m Pr^{0.36} \left( \frac{Pr}{Pr_s} \right)^{1/4} \quad (3.4)$$

where

$$Pr = \frac{\nu}{\alpha}$$

For air, the Prandtl number is approximately equal to 0.707 [23]. There are other important parameters in the study of heat transfer that need to be defined in this Section. The Biot number,  $Bi$ , is a non-dimensional measure of the combined effects of conduction along the cell borders and heat transfer into the fluid.

$$Bi = \frac{h_{fm}d}{k_s} = \left( \frac{k_f}{k_s} \right) Nu \quad (3.5)$$

where  $k_s$  is the conductivity of the solid part of the foam.

The correlation that has been adopted in this research, is the one developed by Holman [23], who established equations for a micro staggered bank of cylinders. These equations are shown next.

$$Bi = 0.91 Pr^{0.36} Re^{0.4} (k_f / k_s) \quad (Re \leq 40) \quad (3.6)$$

$$Bi = 0.62 Pr^{0.36} Re^{0.5} (k_f / k_s) \quad (Re > 40) \quad (3.7)$$

Equations 3.8 and 3.9 are the same as the equations 3.6 and 3.7 in term of the Nusselt number.

$$Nu = 0.91 Pr^{0.36} Re^{0.4} \quad (Re \leq 40) \quad (3.8)$$

$$Nu = 0.62 Pr^{0.36} Re^{0.5} \quad (Re > 40) \quad (3.9)$$

Once the Nusselt number is calculated, the convective coefficient inside the pores of the metal foam can be obtained taking it from Eqn. 3.3. However, following the method developed by Bastawros [1], Eqns. 3.8 and 3.9 need a connection factor  $\lambda$ . So, the effective convective coefficient inside the foam is

$$h_{fm} = \lambda h \quad (3.10)$$

The coefficient  $\lambda$  is determined by experimental calibration and for low density foams it is

$$\lambda = 0.42 \pm 0.09$$

Once that the convective coefficient has been found, it is proceeded with the analysis of the local averaged temperature assumption. From the bank of cylinders theory, it is known that the exit temperature of a fluid once it has passed along the bank can be calculated. The dimensionless temperature difference between the surface cylinder temperature and the air leaving is given in [23].

$$\frac{T_s - T_o}{T_s - T_i} = \exp\left(-\frac{\pi d N h_{fm}}{\rho u N_T S_T c_p}\right) \quad (3.11)$$

The analysis to verify the local averaged temperature assumption is carried out in a small portion of foam. This portion is located in the most critical zone of heat transfer analysis, due to it is very close to the heated base, figure 3.3.

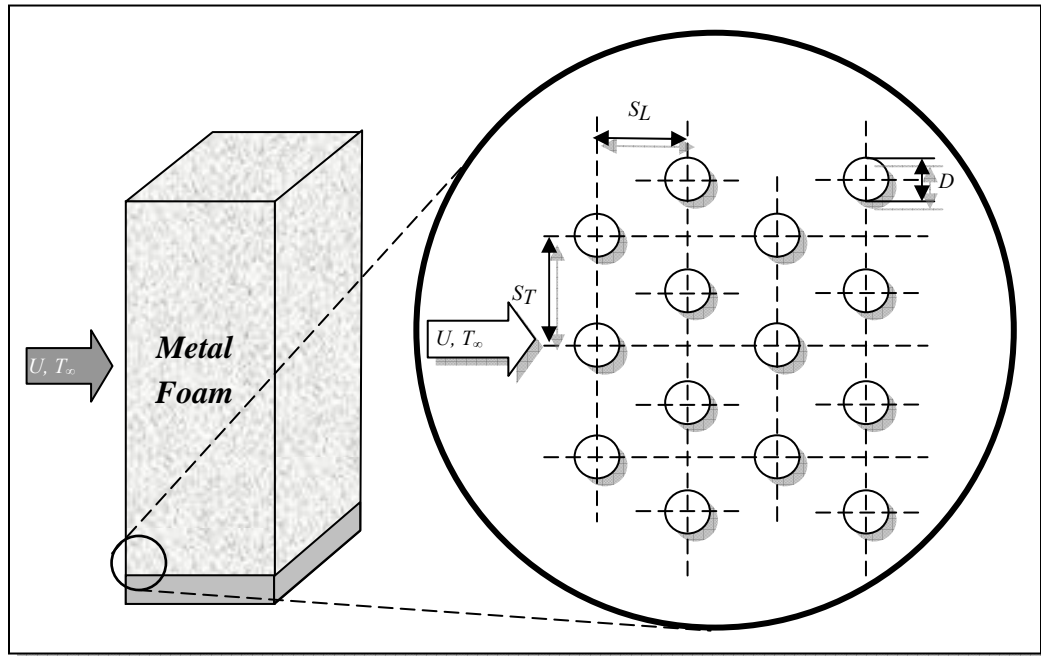


**Figure 3.3 Analyzed metal foam zone and representation as a bank of cylinders.**

Figure 3.3 shows the representation of foam zone as a bank of cylinders. The diameter of the cylinders presented in Figure 3.3 is equivalent to the diameter of the foam filaments.

The value of the filament diameter is taken from Calmidi and Mahajan [10]. They employed a microscope to measure the filament diameter of a metal foam sample similar to the one used in this research. It was found that the filament diameter for a 40 *PPI* sample is equal to 0.00025 m. To estimate the measured pitch, the definition of *PPI* is used, which establishes that the pore size is equal to the number of pores that can be counted in a length of one inch. The transversal pitch is calculated as,

$$S_T = \frac{1''}{40} = 0.025'' = 0.000635 \times 10^{-3} m$$

The density and the specific heat at constant pressure for the air are obtained interpolating between values given by Incropera [23] in the table of thermo physical properties of gases at atmospheric pressure. These values are taken at a temperature of 22°C, which was the air temperature entering to the foam sample during the experiments.

$$\rho_a = 1.1847 \text{ kg} / \text{m}^3$$

$$c_p = 1007 \text{ J} / \text{kg} \cdot \text{K}$$

Previously mentioned, the meet temperature employed was obtained experimentally, as well as the filament surface temperature, which was the highest base temperature observed (85°C) during experimentation.

A length of one inch along the fluid flow direction and a height of 0.05 inches (0.00127 m) are considered in this work. These parameters allow having a total of 82 cylinders and 2 cylinders in the transverse plane. So far, it has only been considered the filaments that are in the horizontal position but, what about the filaments that have vertical position? These filaments also conduct heat and dissipate it into the air. They generate a warming up of the air similar to the horizontal ones. Keeping this in mind, these filaments are considered by doubling the number of cylinders in the horizontal position. Figure 3.4 shows these two possible representations.

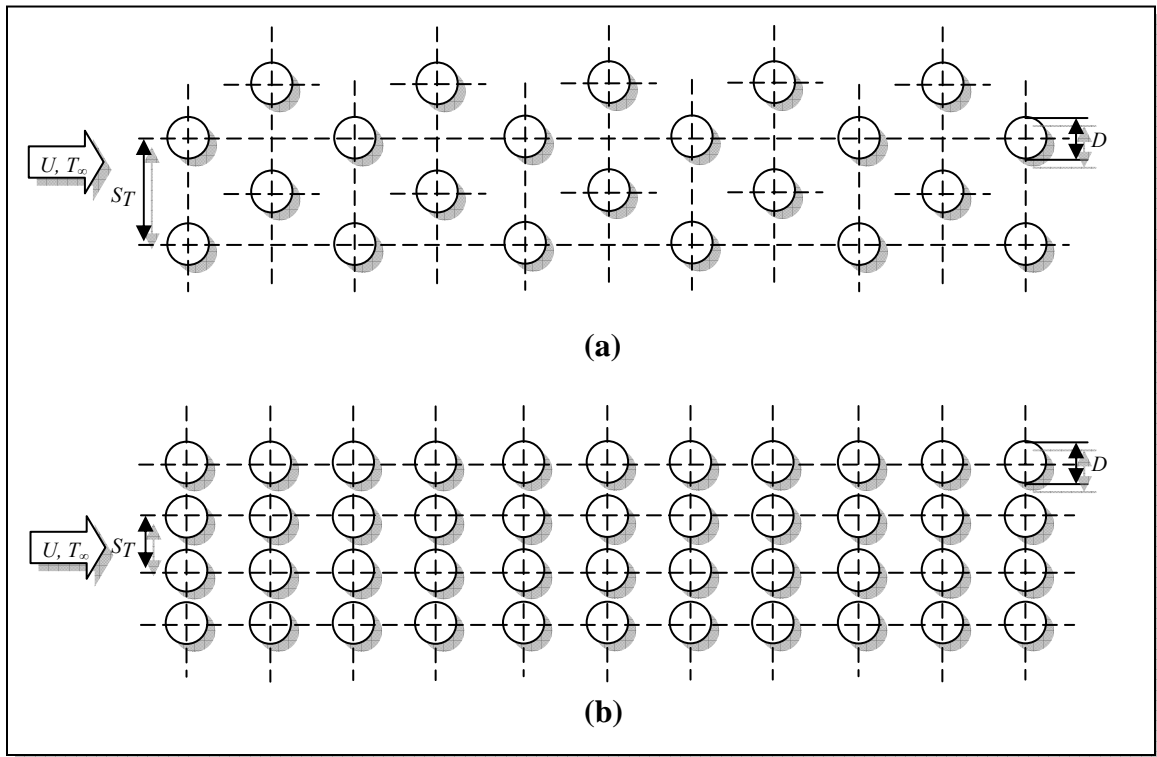


**Figure 3.4 Bank of cylinders arrangements to model metal foam. (a) Modeling with foam filaments only in horizontal position. (b) Considering metal foam filaments in vertical as in horizontal position.**

Thus, the transverse pitch is reduced to one half of its original length. The total number of cylinders is equal to 164 and the number of cylinders in the transverse plane is equal to 4. All these parameters and the convective coefficient given by Eqn. 3.10 are substituted into Eqn. 3.11. Table 3.1 presents the temperature difference between the surface of the filament and the air at one inch of distance from the entrance. These differences were obtained for different pore Reynolds' numbers. The third column of this table gives the percentage difference in temperature at one inch of distance from the entrance against the temperature difference that exists between the solid and fluid phases when the air is entering to the metal foam.

Pore Reynolds Number	Temperature Difference (°C)	Percentage of the temperature difference at the exit relative to the temperature difference at the entrance (%)
27.378	0.099	0.159
49.528	0.626	1.010
66.994	1.192	1.923
74.904	1.478	2.383
84.735	1.848	2.980

**Table 3.1 Temperature difference between the surface filament and the air at one inch from the entrance.**

These temperature differences are indeed very small. The maximum temperature difference between the surface of the filament and the air was of 1.848°C, corresponding to the highest pore Reynolds number. This represented only 2.98% of the temperature difference at the entrance, which means that the temperature difference between the solid and fluid phases can be considered negligible. If the analysis is made at two and three inches of distance from the entrance, the percentage presented in Table 3.1 is still smaller, this is due to the fact that at these distances, the number of cylinders  $N$  would increase and when substituted into Eqn. 3.11, the power on the right side of this equation will be a higher negative number and the difference lower. This analysis proves that the assumption of the local averaged temperature is valid for the kind of foams considered in this work.

### **3.2 HEAT TRANSFER MODEL**

Once the justification for the local thermal assumption has been presented, the next sections are dedicated to the analysis developed to model the heat transfer in the

metal foam. The directions, in which the temperature distribution is studied, and the dimensions of the foam are shown in Figure 3.5.

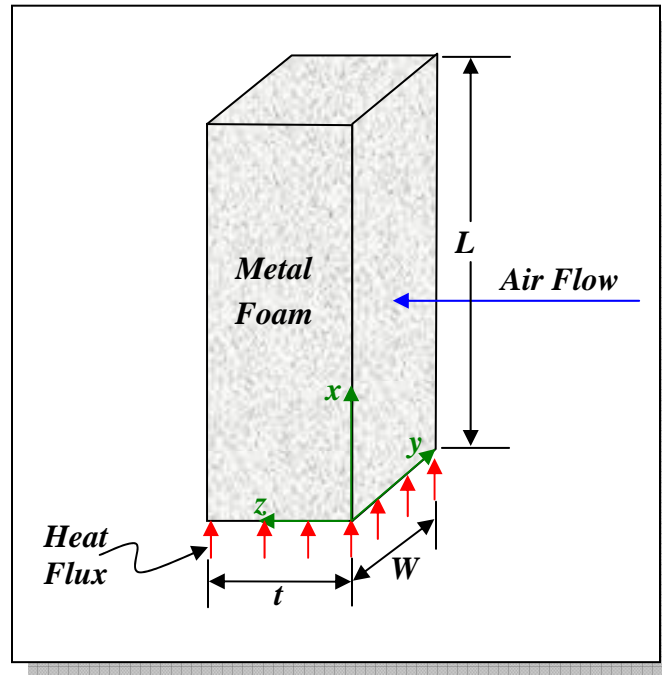


**Figure 3.5 Foam dimensions and heat flow directions.**

To begin the analysis of the heat transfer in the foam, a control volume is defined and the law of conservation of energy is applied to it. In this balance, the heat transfer by conduction through the aluminum filaments and the air is combined with the heat transfer by convection that takes place inside the pores of the foam. Figure 3.6 shows the control volume defined inside the metal foam and used for the analysis, where  $W$  represents the width of the foam and  $dx$  and  $dz$  are small thicknesses in the  $x$  and  $z$  directions, respectively. The energy fluxes due to the conduction and convection heat transfer are considered in Figure 3.6.

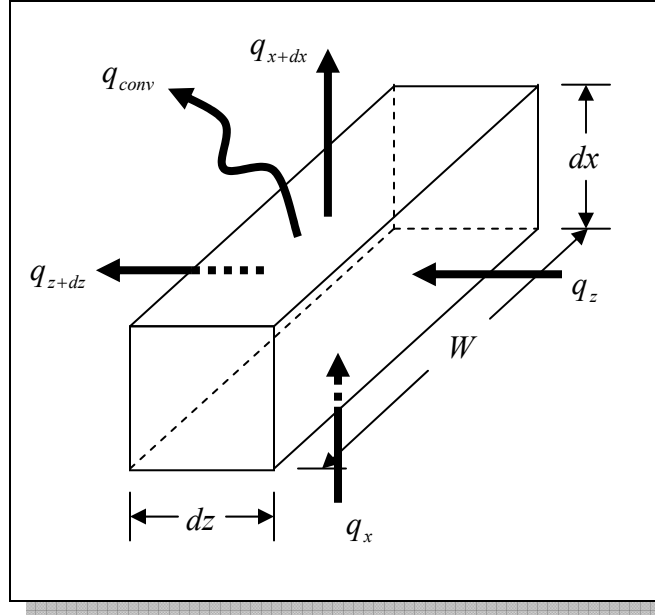


Figure 3.6 Control volume defined inside metal foam.

Applying an energy balance in the control volume, yields,

$$q_x + q_z = q_{x+dx} + q_{z+dz} + q_{conv} \quad (3.12)$$

Heat fluxes by conduction and convection are introduced in Eqn. 3.12. All substitutions of the fluxes and the areas by which these are going to take place, as well as the algebraic manipulations to obtain the energy equation for metal foam are detailed in Appendix A. The energy equation is,

$$\frac{\partial^2 T_{fm}}{\partial x^2} + \frac{\partial^2 T_{fm}}{\partial z^2} - \frac{h_{fm} \sigma}{k_s(1-\varepsilon) + k_f \varepsilon} (T_{fm} - T_\infty) = 0 \quad (3.13)$$

Gathering of terms and introduction of dimensionless variables are applied in Eqn. 3.13. Details are also given in Appendix A. Thus, a dimensionless form of Eqn. 3.13 is obtained as,

$$\frac{\partial^2 \theta_{fm}}{\partial X^2} + \frac{\partial^2 \theta_{fm}}{\partial Z^2} - M^2 \theta_{fm} = 0 \quad (3.14)$$

A boundary condition of a constant temperature  $T_b$  is considered at  $x=0$  ( $X=0$ ). An explanation to consider this assumption is given in Appendix A.

$$\theta_{fm}(0, Z) = \frac{T_b - T_\infty}{T_b - T_\infty} = 1 \quad @ X = 0 \quad (3.15)$$

The foam sample is insulated at the tip in the  $x$  direction ( $x=L$ ,  $X=1$ ),

$$\frac{\partial \theta_{fm}}{\partial X}(1, Z) = 0 \quad @ X = 1 \quad (3.16)$$

The air enters at  $z=0$ ,  $Z=0$  where an assumption of local averaged temperature between fluid and solid phases prevails. Therefore, the temperature at this boundary equals the inlet temperature of the fluid.

$$\theta_{fm}(X, 0) = \frac{T_\infty - T_\infty}{T_b - T_\infty} = 0 \quad @ Z = 0 \quad (3.17)$$

### 3.3. PROPOSED BOUNDARY CONDITIONS AT THE AIR EXIT OF FOAM

At  $z=t$ , some assumptions are made in order to find a good approximation of the variation of temperature at this boundary. These assumptions are listed next:

- ✚ Case 1. Temperature Distribution with linear behavior
- ✚ Case 2. Temperature Distribution with exponential behavior
- ✚ Case 3. Temperature Distribution for a one dimensional model developed by Dukhan and Quiñones [21]
- ✚ Case 4. Temperature Distribution with zero-slope

#### 3.3.1. Temperature distribution with linear behavior

This Section proposes a model in which the temperature distribution has a linear behavior at the border  $z=t$ . It is known that the temperature at  $x=0$  for any  $z$ , is equal to  $T_b$ . For the upper part of this border, the assumption was that the temperature is equal to the fluid temperature  $T_\infty$  coming from the fan. So, Eqn. 3.18 defines the variation of the temperature at the boundary  $z=t$ .

$$\theta_{jm}(X, \frac{z}{L}) = 1 - X \quad (3.18)$$

Once that the condition for the boundary at  $z=t$  has been defined, it is considered the face of the foam where the temperature distribution is been studied. This face is represented in Figure 3.7 with its respective boundary conditions.

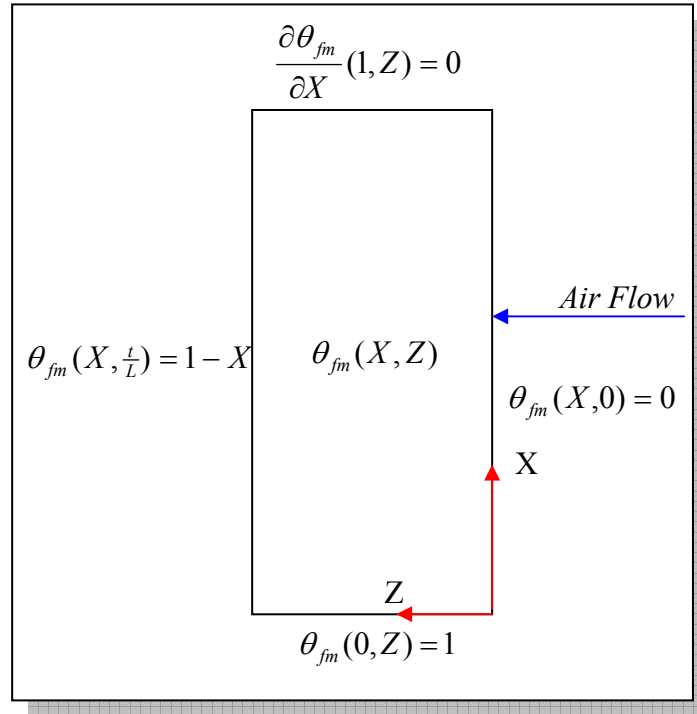


**Figure 3.7 Two-dimensional model.**

As it can be seen, there are two non-homogenous boundary conditions in the model. So, the superposition principle is applied in order to find a solution for  $\theta_{fm}$ . Applying superposition,  $\theta_{fm}$  is defined as the sum of two different variables that depends on  $X$  and  $Z$ :

$$\theta_{fm}(X, Z) = \Psi(X, Z) + \Phi(X, Z) \quad (3.19)$$

Figure 3.8 shows how the model can be separated in two arrangements with only one non-homogeneous boundary condition in each case.

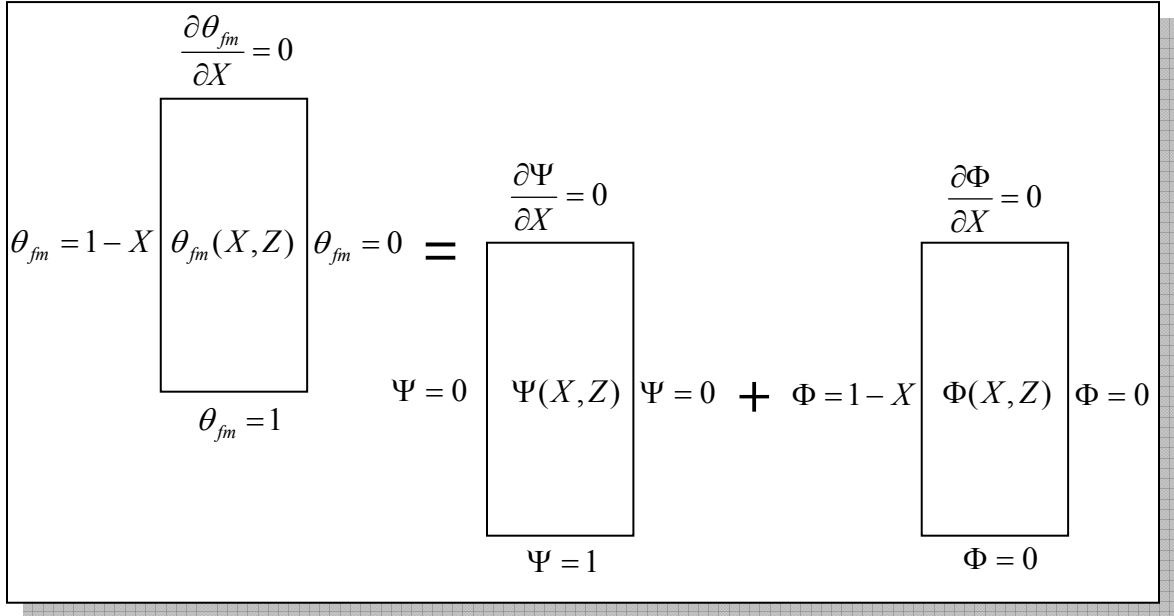


Figure 3.8 Superposition applied to the model (linear case).

Details of the application of superposition and separation of variables methods to obtain the solution are given in Appendix B. The final solution for the dimensionless temperature for this case is given as,

$$\theta_{fm}(x, z) = \sum_{n=0}^{\infty} \frac{2(1-(-1)^n)}{n\pi} \left\{ \cosh \left[ \sqrt{\left( M^2 + \frac{L^2 n^2 \pi^2}{t^2} \right)} X \right] - \tanh \left[ \sqrt{\left( M^2 + \frac{L^2 n^2 \pi^2}{t^2} \right)} \right] \sinh \left[ \sqrt{\left( M^2 + \frac{L^2 n^2 \pi^2}{t^2} \right)} X \right] \right\} \sin \left[ \frac{Ln\pi}{t} Z \right] + \frac{1 - \frac{(-1)^n}{\pi \left( n + \frac{1}{2} \right)}}{\sinh \left[ \sqrt{\left( M^2 + \pi^2 \left( n + \frac{1}{2} \right)^2 \right)} \left( \frac{t}{L} \right) \right] \left[ \frac{\pi}{2} \left( n + \frac{1}{2} \right) \right]} \sin \left[ \pi \left( n + \frac{1}{2} \right) X \right] \sinh \left[ \sqrt{\left( M^2 + \pi^2 \left( n + \frac{1}{2} \right)^2 \right)} Z \right] \quad (3.20)$$

### 3.3.2. Temperature distribution with exponential behavior

To model the exponential variation of the temperature on the border  $z=t$ , the temperature in the lower and upper part of the border are considered. The temperature at  $x=0$  for any  $z$ , is equal to  $T_b$  ( $X=0, \theta_{fm}=1$ ) and at  $x=L$ , the temperature is equal to the inlet temperature  $T_\infty$ . ( $X=1, \theta_{fm}=0$ ) The exponential equation that defines the variation of the dimensionless temperature is:

$$\theta_{fm}(X,Z) = \frac{(e^{1-X} - 1)}{(e-1)} \quad (3.21)$$

This is the new boundary condition at  $z=t$ .

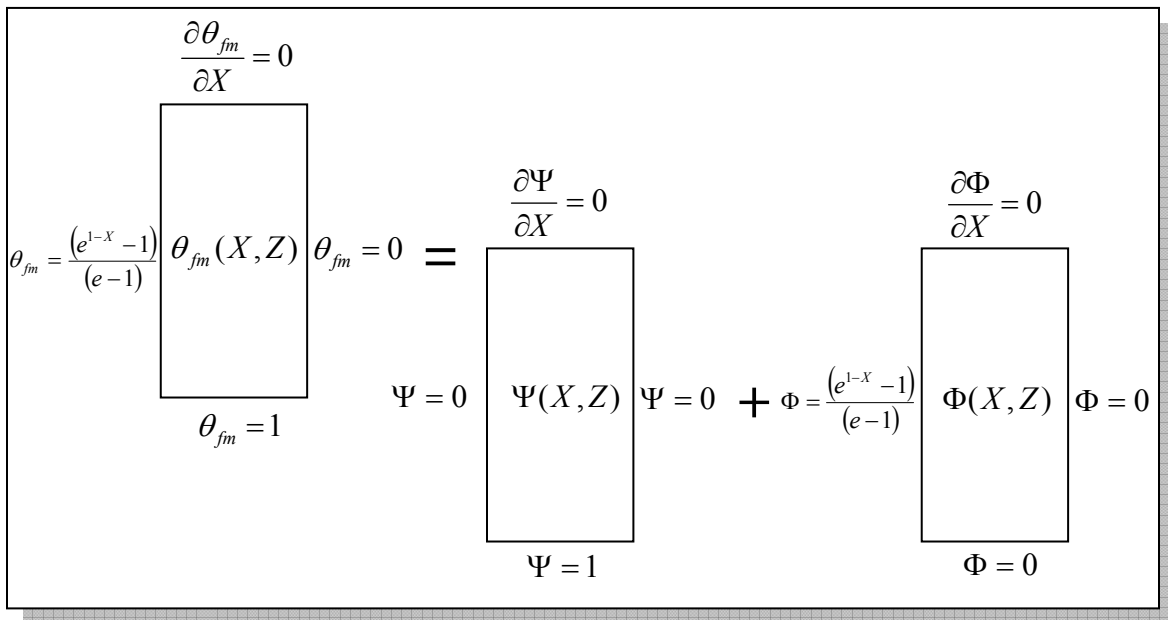


Figure 3.9 Superposition applied to the model (exponential case).

As observed from Figure 3.9, the first individual model of the two models generated after applying superposition is identical to the first individual model generated for case one after superposition. So, it will have the same solution for the first model and the effort is dedicated to solve the second model of the present case. Details of the solution obtained are given in Appendix B. The final solution for the exponential variation case is given as,

$$\theta_{fm}(x, z) = \sum_{n=0}^{\infty} \frac{2(1-(-1)^n)}{n\pi} \left\{ \cosh \left[ \sqrt{\left( M^2 + \frac{L^2 n^2 \pi^2}{t^2} \right)} X \right] - \tanh \left[ \sqrt{\left( M^2 + \frac{L^2 n^2 \pi^2}{t^2} \right)} \right] \sinh \left[ \sqrt{\left( M^2 + \frac{L^2 n^2 \pi^2}{t^2} \right)} X \right] \right\} \sin \left[ \frac{Ln\pi}{t} Z \right] +$$

$$+ \frac{2}{e-1} \left\{ \frac{1}{\pi^2 \left( n + \frac{1}{2} \right)^2 + 1} \left[ e^{\pi \left( n + \frac{1}{2} \right)} - (-1)^n \right] - \frac{1}{\pi \left( n + \frac{1}{2} \right)} \right\} \frac{\sin \left[ \pi \left( n + \frac{1}{2} \right) X \right] \sinh \left[ \sqrt{\left( M^2 + \pi^2 \left( n + \frac{1}{2} \right)^2 \right)} Z \right]}{\sinh \left[ \sqrt{\left( M^2 + \pi^2 \left( n + \frac{1}{2} \right)^2 \right)} \left( \frac{L}{t} \right) \right]} \quad (3.22)$$

### **3.3.3. Temperature distribution for a one dimensional model of Dukhan and Quiñones**

For this case, the equation developed by Dukhan and Quinones [21] for the characterization of the heat transfer in a foam using a one dimensional model is employed.

$$\theta_{fm}(x, t) = \frac{\cosh m_{fm}(L-x)}{\cosh m_{fm}L} \quad (3.23)$$

Taking the dimensionless parameters defined in this research, Eqn. 3.23 is non-dimensionalized obtaining Eqn. 3.24.

$$\theta_{fm}(X, \frac{t}{L}) = \frac{\cosh M(1-X)}{\cosh M} \quad (3.24)$$

Again, the problem is separated into two easier problems to solve. The boundary conditions are distributed between the two models. Figure 3.10 shows the models generated once the superposition principle has been applied.

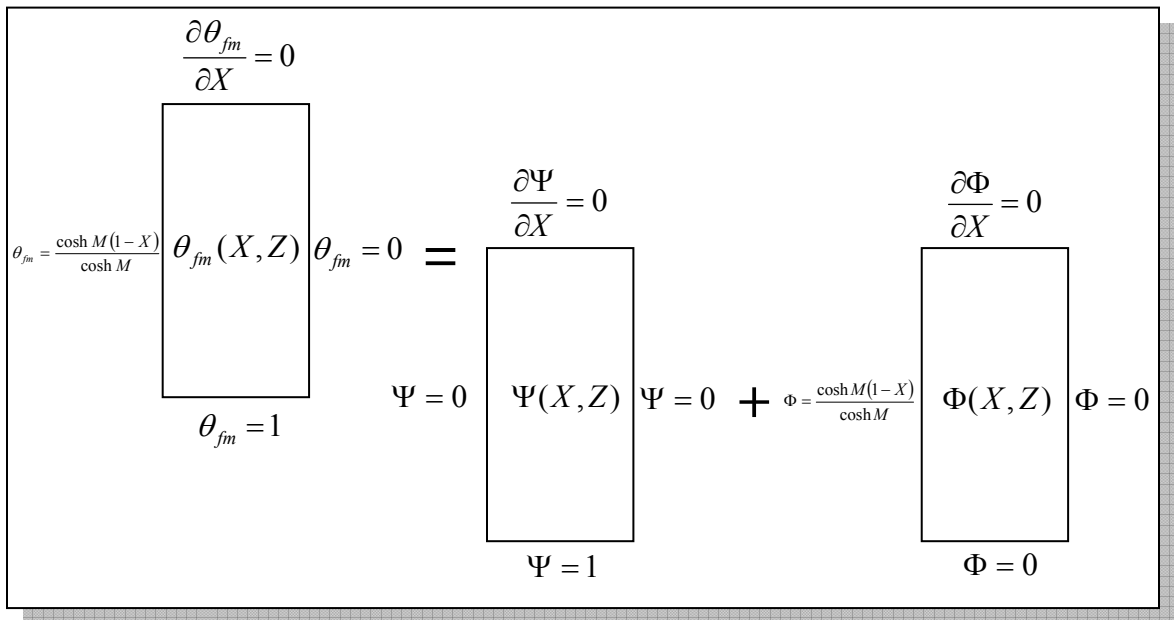


**Figure 3.10 Superposition (case of the 1D model boundary condition).**

The final solution for the dimensionless temperature in the metal foam under the boundary condition specified in this case is given by Eqn. 3.25. Details of deduction are given in Appendix B.

$$\theta(X, Z) = \sum_{n=0}^{\infty} \frac{2(1-(-1)^n)}{n\pi} \left\{ \cosh \left[ \sqrt{\left( M^2 + \frac{L^2 n^2 \pi^2}{t^2} \right)} X \right] - \tanh \left[ \sqrt{\left( M^2 + \frac{L^2 n^2 \pi^2}{t^2} \right)} \right] \sinh \left[ \sqrt{\left( M^2 + \frac{L^2 n^2 \pi^2}{t^2} \right)} X \right] \right\} \sin \left[ \frac{Ln\pi}{t} Z \right] + \frac{2 \left[ \pi \left( n + \frac{1}{2} \right) \right]}{\left( \pi^2 \left( n + \frac{1}{2} \right)^2 + M^2 \right) \sinh \left[ \sqrt{\left( M^2 + \pi^2 \left( n + \frac{1}{2} \right)^2 \right)} \left( \frac{t}{L} \right) \right]} \sin \left[ \pi \left( n + \frac{1}{2} \right) X \right] \sinh \left[ \sqrt{\left( M^2 + \pi^2 \left( n + \frac{1}{2} \right)^2 \right)} Z \right] \quad (3.25)$$

### **3.3.4. Temperature distribution with zero-slope**

For this case the slope of the temperature variation at  $z=t$  is zero is analyzed; is where the temperature reaches its maximum value in the  $z$  direction at this point. When air leaves the foam, it is at the maximum temperature and then it begins to drop off. So, after air leaves the foam, the temperature of the air keeps decreasing until it reaches the ambient conditions. Therefore, the boundary condition at  $z=t$  is considered as,

$$\frac{\partial \theta_{fm}}{\partial Z} = 0$$

Figure 3.11 represents the surface in which the variation of the temperature is analyzed using the boundary condition described above.

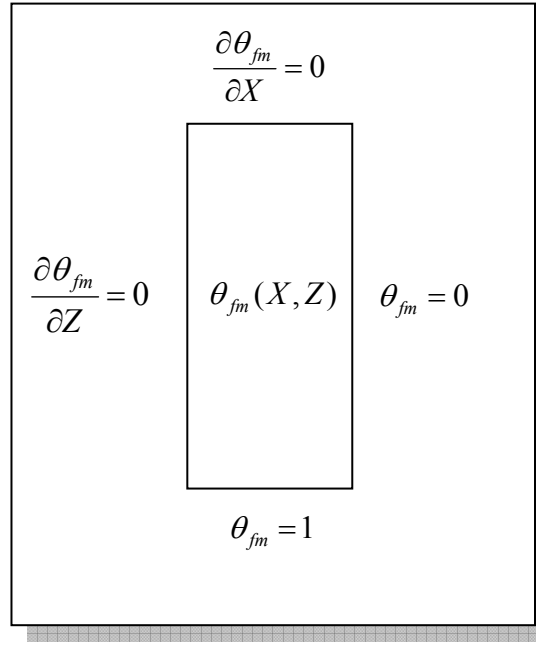


**Figure 3.11 Two-dimensional model for the zero slope case.**

The final solution for this fourth case is obtained and is expressed by Eqn. 3.26.

Details of its derivation are given in Appendix B.

$$\theta_{fm}(X, Z) = \sum_{n=0}^{\infty} \frac{2}{\pi \left(n + \frac{1}{2}\right)} \left\{ \cosh \left[ \sqrt{M^2 + \frac{L^2 \pi^2 \left(n + \frac{1}{2}\right)^2}{t^2}} X \right] - \tanh \left[ \sqrt{M^2 + \frac{L^2 \pi^2 \left(n + \frac{1}{2}\right)^2}{t^2}} \right] \sinh \left[ \sqrt{M^2 + \frac{L^2 \pi^2 \left(n + \frac{1}{2}\right)^2}{t^2}} X \right] \right\} \sin \left[ \frac{L \pi \left(n + \frac{1}{2}\right)}{t} Z \right] \quad (3.26)$$

The comparisons between these solutions and the experimental results will be shown in Chapter 5 of this thesis. The model that best represents the heat transfer will be selected and in this way, a mathematical method to predict the heat transfer through metal foams under different forced convection conditions will be established.

## **CHAPTER 4**

### **EXPERIMENTAL WORK**

The objective of this Chapter is to show some of the most important aspects of the materials and equipment employed to carry out the research and the experimental methodology followed to validate the analytical model.

#### **4.1 MATERIALS AND EQUIPMENT**

The most important items employed in this research are the metal foam sample, a wind tunnel, heaters, a power supply and a data acquisition system. The metal foam sample is the heart of the entire research setup. Other equipment is used to generate the physical conditions described in the Chapter 3 (convective medium, heat, etc).

##### **4.1.1 Metal foam sample**

The foam sample used in the research is made of aluminum alloy 6101-T6 manufactured by ERG Materials and Aerospace Corporation. This alloy has a conductivity of 218 W/m K. The pore density can be found in several options, the most common are 5, 10, 20 and 40 pores per linear inch (*PPI*) and can be adjusted independently of the variation of the relative density. Figure 4.1 shows a picture of a 40 PPI foam sample.



**Figure 4.1 Metal foam sample.**

The metal foam sample employed in this research has a pore density of 40 PPI. The dimensions of the sample are 4"×9.5"×4", brazed to a solid aluminum base of 0.5"×4"×4". Figure 4.2 show a drawing of the foam sample with its respective dimensions. This figure shows also the coordinate system to which we are going to be reference in the entire thesis.

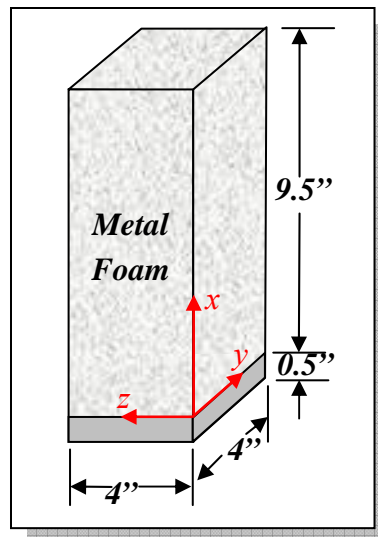


**Figure 4.2 Foam sample dimensions and coordinate system.**

The relative density  $\rho$  reported by the manufacturer is 6-8%. Since this value is of great importance to us because it is used to calculate the air velocity at the pores, an analysis is carried out in order to find a more exact value for  $\rho$ . Another important parameter used in the heat equation is the porosity,  $\epsilon$ , which is also calculated.

In the procedure employed, the sample was weighted and this value was translated to mass. The result was 1.946 lbs. Knowing that the density of the Al 6101-T6 is about 0.098 lb/in<sup>3</sup>, and having the dimensions of the solid base, it was possible to calculate the mass of the base and subtracted this value from the total mass of the sample. This was made because we were only interested in the mass of the metal foam. Once we had this value, it was divided by the volume of the foam in the following manner:

$$\rho_{foam} = \frac{m_{foam}}{V_{foam}} = \frac{1.946 \text{ lb} - (0.098 \text{ lb} / \text{in}^3)(4 \text{ in} \times 4 \text{ in} \times 0.5 \text{ in})}{4 \text{ in} \times 4 \text{ in} \times 9.5 \text{ in}} = 0.007644 \text{ lb} / \text{in}^3$$

The definition of the relative density is the ratio of the density of the foam to the density of the base material, which is aluminum alloy 6101. So, the relative density of our foam sample is:

$$\rho = \frac{\rho_{foam}}{\rho_{material}} = \frac{0.007644 \text{ lb} / \text{in}^3}{0.098 \text{ lb} / \text{in}^3} = 0.078 \quad \text{or} \quad 7.8\%$$

The porosity  $\varepsilon$  of the sample is the ratio of the volume that the air occupies in the sample to the total volume of the sample. To know the volume of the air, we calculate the volume of solid part of the foam. This can be known dividing the mass of solid part of the foam (mass of the foam) by the density of the base material.

$$V_{ss} = \frac{m_{foam}}{\rho_{material}} = \frac{1.1618 lb}{0.098 lb / in^3} = 11.85 in^3$$

The volume of the solid part of the sample ( $V_{ss}$ ) is subtracted from the total volume of the sample to get the volume of the air inside the foam sample. This value is then divided by the total volume of the sample and so the porosity of the foam is obtained.

$$\varepsilon = \frac{V_{air}}{V_{foam}} = \frac{V_{foam} - V_{ss}}{V_{foam}} = \frac{(4 in \times 4 in \times 9.5 in) - 11.85 in^3}{4 in \times 4 in \times 9.5 in} = 0.921$$

#### **4.1.2 Wind tunnel**

The wind tunnel employed was manufactured by TecQuipment. Its official name is TD.49 Multi-Purpose Air Duct. The apparatus consists of a rectangular duct which is designed and constructed in sections, clipped tightly together with snap-action fasteners and supported at four points along its length.

The duct section is 150 mm wide by 300 mm high inside measurement (6 in x 12 in), the cross sectional area of the duct is  $0.045 \text{ m}^2$  ( $0.485 \text{ ft}^2$ ) and the overall length of the duct section is 290 mm (11.4 in). The duct and its conical inlet are constructed in accordance with British Standard recommendations. Entry and exit duct-sections are separated by a plain centre-section which is easily removed. Figure 4.3 is a picture of the wind tunnel used in the research.



**Figure 4.3 Wind tunnel.**

The centrifugal fan is arranged to draw air along the duct and is provided with a throttle slide-plate at the fan delivery for varying the flow rate. The fan delivery is a single-inlet, overcast discharge flanged aperture 90 mm x 90 mm suction aperture approximates of 20 mm in diameter.

The motor specifications are as follows: 220/240 V., 1 ph., 50 Hz, 4.6 amps, 2850 rpm directly connected to the fan shaft. Determination of the air-flow rate and the air velocity profiles can be made by pitot-static tubes mounted in a traversing mechanism. Figure 4.4 shows a diagram where the major components of the wind tunnel are indicated.

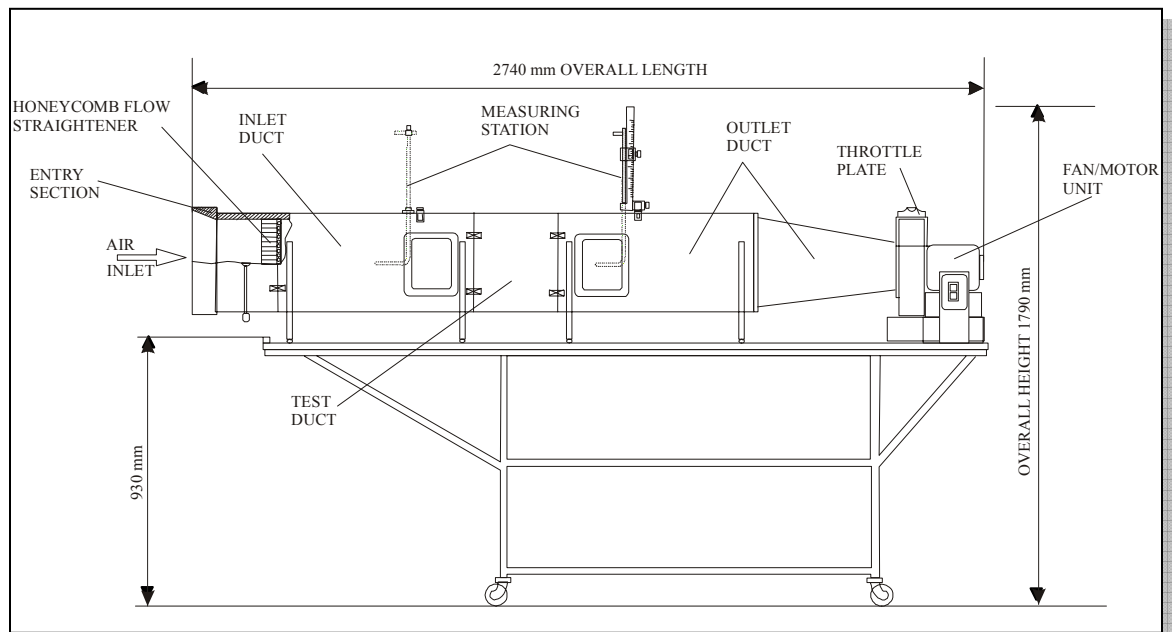


**Figure 4.4 Diagram of wind tunnel**

A pitot tube was used to take measurements of the dynamic pressure and these measurements are transduced to velocity measurements. Figure 4.5 shows a diagram of the Pitot tube used in the wind tunnel and its sliding mechanism.

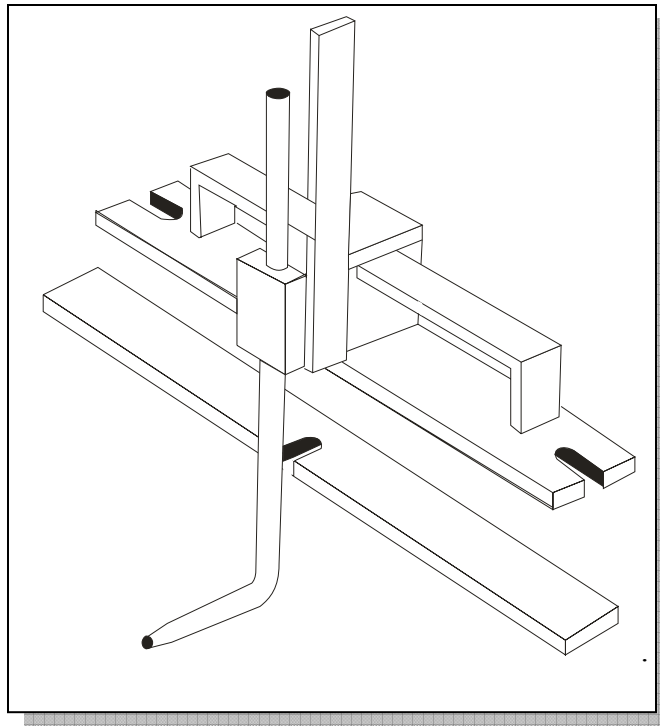


**Figure 4.5 Diagram of Pitot tube**

### **4.1.3 Heaters**

Several heaters manufactured by Minco, Inc. were used in this experimental work. They were made of Silicone Rubber, which is a rugged, flexible elastomer material with excellent temperature properties. Silicon Rubber heaters are ideal for applications with limitations in space, as in the case of the experimental set-up constructed for this research. The temperature range in which this kind of heaters can work is from -45 to 235°C (-50 to 455°F).

The heaters used in this work have a size that is identical to the size of the base of the foam (4" x 4"). They have an electric resistance of 42.9  $\Omega$  and the maximum power that this kind of heater can supply is 308 W at 115 VDC. The wires by which the heater is

fed have a diameter of 0.050" to support the necessary current for the power mentioned.

Figure 4.4 shows a picture of the heaters employed.

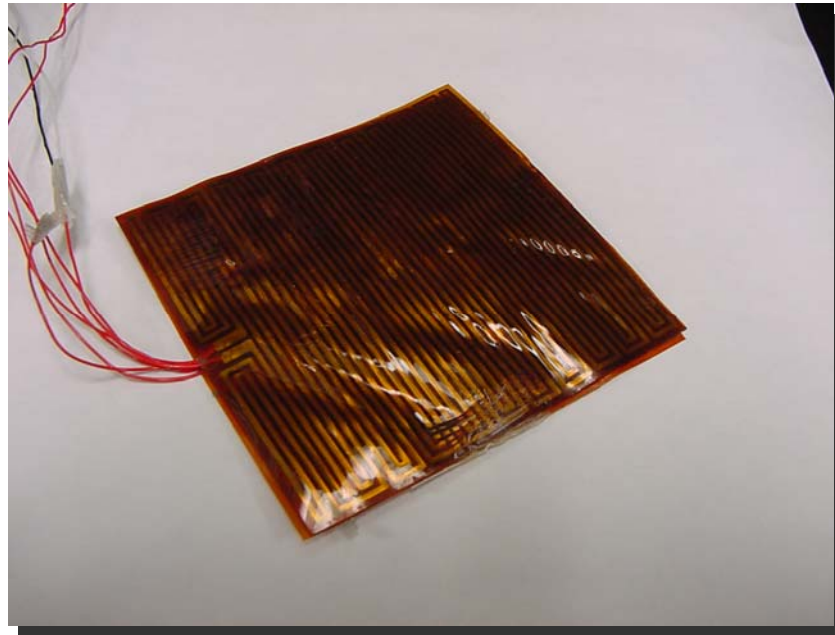


**Figure 4.6 Heaters.**

#### **4.1.4 Power Supplies**

Two pairs of power supply were used to feed the heaters. Two GP-4303TP DC power supply manufactured by EZ Digital Co. and two E3632A DC power supply manufactured by Hewlett Packard were employed in the research. The first pair has 0-30VDC as range of output voltage and a current range of 0-3 AMP. The maximum output power is then equal to 90 W. The second pair has two options of output power. The first option has a voltage range from 0 to 15 V with a maximum current of 7 A, and the second option has an output voltage range from 0 to 30 V reaching an output current of 4

A. The maximum power of this second kind of power supply is 120 W. So, these devices are connected in series in order to reach the necessary voltage to generate maximum required power. In the series connection, three of the power supplies are set to give their maximum output voltage (30 V) and the fourth power supply is set to give 25 V in order to obtain 115 V corresponding to the maximum power. Figure 4.7 shows a picture of the power supplies described in this Section.



**Figure 4.7 Power Supplies.**

#### **4.1.5 Data acquisition system**

The data acquisition system employed to take the temperature measurements was composed of the following elements:

- Computer
- SCXI 2000 chassis
- SCXI-1200 module DAQ device
- SCXI 1122 signal conditioning module

- SCXI-1322 terminal block
- Serial cable
- 7-inch Parallel-port cable adapter
- 14 Type T thermocouples

The computer used was a commercial PC in which LabView software from National Instruments was installed. The SCXI-2000 is a rugged, low-noise chassis that can hold up to four SCXI modules. This chassis powers SCXI module handles all timing, trigger, and signal routing between the digitizer and SCXI modules. SCXI-1200 is a device that can be used to acquire data and as a control module. It has eight analog input channels, 24 Lines of TTL-Compatible Digital I/O and 16-Bit Counter/Timer. The National Instruments SCXI-1122 is designed for a wide variety of sensor and signal inputs requiring isolation. This module can acquire strain, RTD, thermocouple, millivolt, volt, 250 V, 0 to 20 mA, and 4 to 20 mA current input signals. Terminal blocks, as the SCXI-1322, are devices designed for specific input types, such as thermocouples, strain gauges, and high-voltage inputs. SCXI-1322 terminal block is compatible with the SCXI-1122 module. The serial cable is a RS-232 communications cable. The 7-inch Parallel-port cable adapter is a small cable with serial ports that was used to connect the SCXI-2000 chassis to the SCXI-1200 DAQ device.

A total of fourteen thermocouples type T were employed. These thermocouples are made of Copper and Constantan, and they are employed in applications where the temperature is less than 400°C. Some subminiature thermocouple connectors were used

in order to connect the thermocouples to the SCXI-1322 terminal block. The elements were connected in the following manner. First, the SCXI-1200 module DAQ Device was inserted into the first slot of the SCXI-2000 chassis and the SCXI-1122 in the second slot. Then, the parallel-port cable was connected from the back of the SCXI-1200 to the parallel port (LPT1) on the back of the computer. While this connection was maintained, the SCXI-1200 module DAQ device was installed in the computer. This action could be made following the procedure described by National Instruments Company, who is the manufacturer of the SCXI chassis and DAQ device, signal conditioning module as well as the terminal block. Once that the DAQ device was recognized by the computer, the 7-inch parallel-port cable was connected from the back of the SCXI-1200 module to the back of the SCXI-2000 chassis and then the RS-232 serial cable was connected from the front of the SCXI-2000 chassis; to the serial port (COM1) of the computer. After that, all the steps remaining were related to the software. Once that the chassis, DAQ device, signal conditioning module and terminal block were settled, the fourteen thermocouples were attached to the terminal block. Connection of the thermocouples to the terminal block was careful because thermocouples have polarity and if this polarity is changed, problems in taking the data appear. The wire made of copper has a positive polarity, and the wire made of constantan has a negative polarity. The SCXI-1322 has indication of where the positive and negative terminals have to be connected.

A computer program to read the temperature measurements was developed in the LabView ambient. An important characteristic of this system is that the data was not

taken in real time, but this is not relevant since the temperature measurements were taken at steady state conditions.



**Figure 4.8 Data Acquisition System.**

## **4.2 EXPERIMENTAL METHODOLOGY**

### **4.2.1 Average tunnel velocity measurement**

The first step in the experiments carried out to validate the analytical model was to take measurements of the flow velocity inside the wind tunnel. To take these measurements a Pitot tube was employed. Figure 4.9 shows the Pitot tube mounted in the wind tunnel.



**Figure 4.9 Pitot tube**

The equation used to calculate the air velocity when a pitot tube is employed is,

$$U = \sqrt{\frac{2p_d}{\rho_a}} \quad (4.1)$$

where  $p_d$  is the  $\Delta p$  between the total pressure and the static pressure. The density of the air can be calculated measuring the air temperature inside the tunnel with a thermocouple and so, we will have all the data necessary to calculate the velocity of the air.

The methodology that was followed to find the average velocity along the wind tunnel follows Kaviany's [27] theory. It considers that the air velocity profile that exits the foam has a constant behavior. So, taking advantage of this velocity characteristic, it was assumed that the exit air velocity was equal to the average velocity along the wind tunnel. To find this constant velocity profile, the Pitot tube was set at different distances

from the face of the foam where the air exits. These distances were ½, 1, 1½ and 2 inches, as shown in Figure 4.10. For each distance, a set of measurements were taken to be sure that the data taken was good. This was made for different air flow rates. The air flow rates used in the experiments were 100%, 80%, 60%, 40% and 20%. These air flow rates were gotten sliding a throttle plate at the exit of the air from the wind tunnel. Figure 4.10 shows a schematic of the pressure measurement methodology used to find the average velocity.

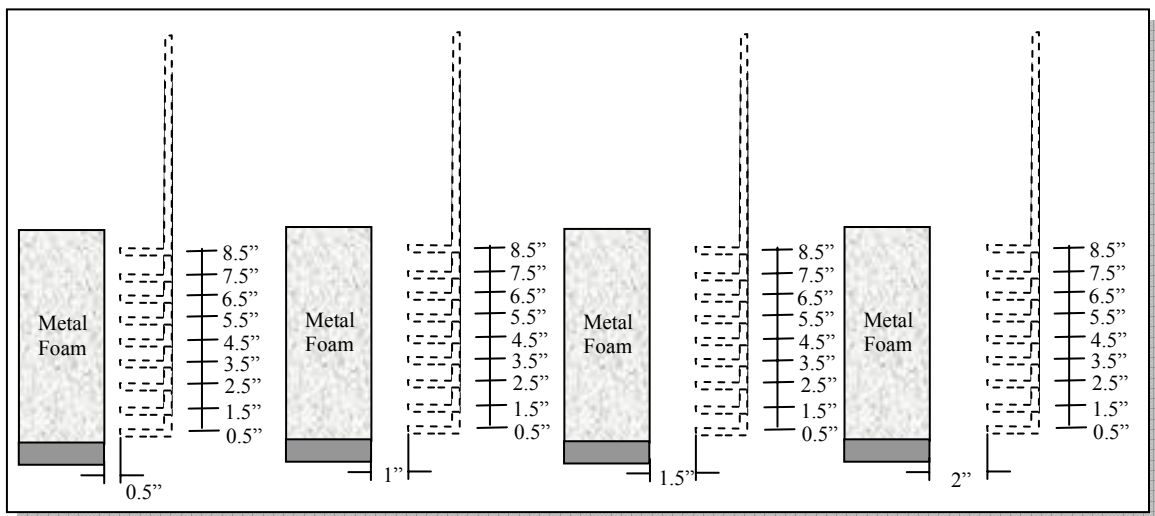


**Figure 4.10 Velocity measurement methodology**

Once that the last procedure was made, the velocity profiles were obtained using the Eqn. 4.1 It was found that the most constant velocity profile was reached taking measurements at 2 inches from the face where the air exists for all the flow rates. Table 4.1 presents the average velocity calculated for each flow rate.

Flow rate	Velocity (m/s)
100%	4.97
80%	4.39
60%	3.93
40%	2.90
20%	1.60

**Table 4.1 Average velocity in the wind tunnel for different flow rates**

#### **4.2.2 Temperature measurements**

Once the average velocity was determined, some Kapton heaters were used to supply the heat. The foam sample was provided with three thin thermfoil heaters that were attached to its solid aluminum base.

The heaters were connected in parallel in order to receive the same voltage. As previously stated, each one of these heaters has a maximum power of 80 W. The total power was 240 W with a power density of  $15.79 \text{ W/in}^2$ . Heaters needed to be connected to a source of 115 VDC in order to give the maximum power. So, the heaters were connected to the DC power supply to provide the electrical power. Figure 4.11 shows the experimental set-up used in this experimental work.

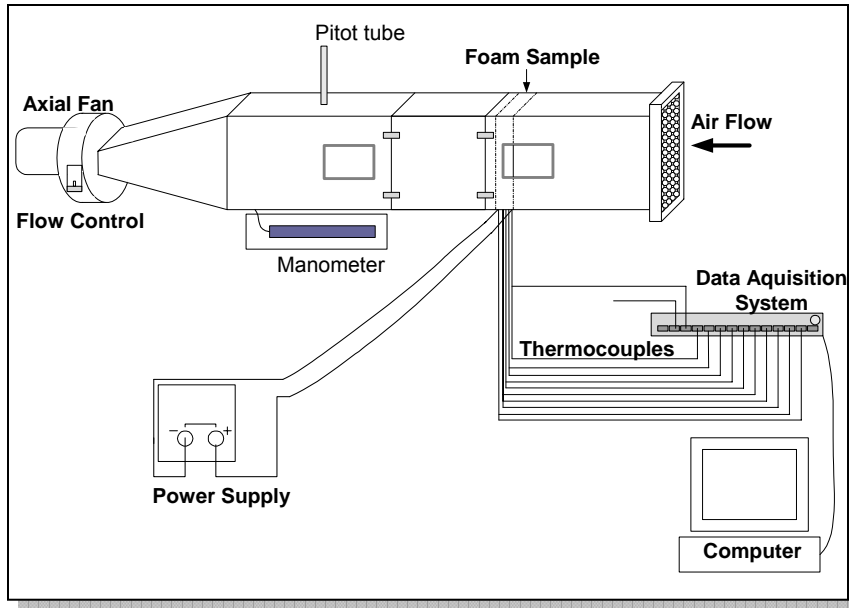


**Figure 4.11 Schematic of the experimental set-up**

The four sides of the foam sample that constituted its outer perimeter were insulated using one-inch thick Styrofoam insulation, and the sample was placed in the tunnel's test section. The other two sides were perpendicular to the flow direction and remain open to the airflow. The insulation material ensured that the flow travel through the foam only, allowing only a negligible flow between the insulation and the tunnel walls.

A total of fourteen thermocouples were used to measure the temperature at different strategic locations in the foam as well as the ambient and the base temperatures. The fourteen thermocouples were moved along the z direction to verify the temperature variation in this direction. The temperature measurement locations in the sample are listed in Table 4.2.

Smaller spacing of the thermocouples was used close to the base, to capture the anticipated steep drop in temperature. The thermocouples were attached to the channels of the automatic data acquisition system, which was connected to the computer, where the temperature readings were shown on the screen.

Thermocouple No.	Location, x, cm (inch) z = 25.4 (1.00)	Location, x, cm (inch) z = 50.8 (2.00)	Location, x, cm (inch) z = 76.2 (3.00)	Location, x, cm (inch) z = 95.25 (3.75)
1	Base	Base	Base	Base
2	0.64 (0.25)	0.64 (0.25)	0.64 (0.25)	0.64 (0.25)
3	1.27 (0.50)	1.27 (0.50)	1.27 (0.50)	1.27 (0.50)
4	1.91 (0.75)	1.91 (0.75)	1.91 (0.75)	1.91 (0.75)
5	2.54 (1.00)	2.54 (1.00)	2.54 (1.00)	2.54 (1.00)
6	3.18 (1.25)	3.18 (1.25)	3.18 (1.25)	3.18 (1.25)
7	3.81 (1.50)	3.81 (1.50)	3.81 (1.50)	3.81 (1.50)
8	4.44 (1.75)	4.44 (1.75)	4.44 (1.75)	4.44 (1.75)
9	5.08 (2.00)	5.08 (2.00)	5.08 (2.00)	5.08 (2.00)
10	6.35 (2.50)	6.35 (2.50)	6.35 (2.50)	6.35 (2.50)
11	8.89 (3.50)	8.89 (3.50)	8.89 (3.50)	8.89 (3.50)
12	13.97 (5.50)	13.97 (5.50)	13.97 (5.50)	13.97 (5.50)
13	19.05 (7.50)	19.05 (7.50)	19.05 (7.50)	19.05 (7.50)
14	Ambient	Ambient	Ambient	Ambient

**Table 4.2 Thermocouples locations**

The temperature measurements were read from the computer screen and these were introduced in Excel pages where the calculation of the dimensionless temperature was carried out using Eqn.A.20. Dimensionless temperature was plotted against dimensionless distance along x direction and these plots were used to compare with the theoretical data generated by the equations obtained in Chapter 3. More details about the results and comparisons will be given in Chapter 5. It will show how the analytical model proposed in this work was easily validated with very simple experiments.

### **4.3 UNCERTAINTY ANALYSIS**

The uncertainty analysis is used to quantify the data validity and accuracy of the experimental work. An uncertainty analysis was conducted for the length, air velocity and temperature measurements taken in this research.

#### **4.3.1 Uncertainty in length**

As it was explained before, some temperature measurements were taken in the metal foam at different locations. It must be noticed that in order to set the thermocouples to measure the temperature, we had to drill a hole to insert the thermocouple in the metal foam. These locations were determined using an appropriate length scale to set the distances. From an analysis of the variables and parameters that can affect the outcome of the length measurements, it was realized that the uncertainty in the length can be estimated using the ruler employed in the length measurement that has a resolution of 1/16 inch. However, there are other conditions that we must keep in mind to do a good uncertainty analysis, such as the structure of the metal foam. When we set the distance for the thermocouples, we tried to make the hole in the correct position, but the drill had the tendency to travel where the foam is more porous. Also, the thermocouple is made of flexible wires that can be easily bent and it can deviate from its original direction. All of these increase our uncertainty to at least 1/8 inch. The uncertainty can be expressed as a percentage, which is called relative uncertainty. The relative uncertainty in the length for our case is given by,

$$u_L = \frac{\pm 1/8 \text{ inch}}{3.75 \text{ inches}} = \pm 0.03333 \text{ or } u_L = \pm 3.333 \%$$

The value of 3.75 in corresponds to the mid value of the range in which we did length measurements (the range measured was 0 – 7.5 in). So, this uncertainty represents the average relative uncertainty of the length measurements.

#### 4.3.2 Uncertainty in air velocity

To calculate the uncertainty in the air velocity, an analysis of the propagation of the uncertainty in the calculations is made. In this analysis, the relative uncertainty of each independent measured quantity is estimated. The measurements are used to calculate some result  $R$  for the experiment. This result is a function of other measured variables, which are denoted by  $x_1, x_2, \dots, x_n$ . The effect that has a measuring error of a variable  $x_i$  on  $R$  is given by

$$\delta R_i = \frac{\partial R}{\partial x_i} \delta x_i \quad (4.2)$$

It is convenient to normalize this equation to obtain

$$\frac{\delta R_i}{R} = \frac{1}{R} \frac{\partial R}{\partial x_i} \delta x_i = \frac{x_i}{R} \frac{\partial R}{\partial x_i} \frac{\delta x_i}{x_i} \quad (4.3)$$

Equation 4.3 is used to estimate the uncertainty interval in the result due to variations in  $x_i$ .

$$u_{R_i} = \frac{x_i}{R} \frac{\partial R}{\partial x_i} u_{x_i} \quad (4.4)$$

To estimate the uncertainty in  $R$  due to the combined effects of uncertainty intervals in all the  $x_i$ s, Eqn. 4.5 is employed.

$$u_R = \pm \left[ \left( \frac{x_1}{R} \frac{\partial R}{\partial x_1} u_1 \right)^2 + \left( \frac{x_2}{R} \frac{\partial R}{\partial x_2} u_2 \right)^2 + \dots + \left( \frac{x_n}{R} \frac{\partial R}{\partial x_n} u_n \right)^2 \right]^{1/2} \quad (4.5)$$

The calculation of the air velocity was made employing a Pitot tube. Dynamic pressure measurements were taken with this device and Eqn. 4.1 was used to transduce the pressure measurements into velocity measurements. Partial derivations are obtained from Eqn. 4.1 with respect to the two variables involved in this:

$$\frac{p_d}{U} \frac{\partial U}{\partial p_d} = \frac{p_d}{U} \frac{1}{2} \left( \frac{2p_d}{\rho_a} \right)^{-1/2} \left( \frac{2}{\rho_a} \right)$$

$$\frac{p_d}{U} \frac{\partial U}{\partial p_d} = \frac{p_d}{U} \frac{1}{2} \frac{1}{U} \left( \frac{2}{\rho_a} \right) = \frac{1}{2} \left( \frac{2p_d}{\rho_a} \right) \frac{1}{U^2} = \frac{1}{2} \frac{U^2}{U^2} = \frac{1}{2}$$

$$\frac{\rho_a}{U} \frac{\partial U}{\partial \rho_a} = \frac{\rho_a}{U} \frac{1}{2} \left( \frac{2p_d}{\rho_a} \right)^{-1/2} \left( \frac{-2p_d}{\rho_a^2} \right)$$

$$\frac{\rho_a}{U} \frac{\partial U}{\partial \rho_a} = \frac{\rho_a}{U} \frac{1}{2} \frac{1}{U} \left( -\frac{U^2}{\rho_a} \right) = -\frac{1}{2} \frac{U^2}{U^2} \frac{\rho_a}{\rho_a} = -\frac{1}{2}$$

Applying Eqn. 4.5, the uncertainty in the air velocity can be estimated by

$$u_U = \pm \left[ \left( \frac{1}{2} u_{p_d} \right)^2 + \left( -\frac{1}{2} u_{\rho_a} \right)^2 \right]^{1/2}$$

The relative uncertainty of the pressure is calculated considering a calibration error of the manometer and the zero-order uncertainty of the same device. The most common calibration error for this kind of devices is about 1 mm H<sub>2</sub>O and the zero-order uncertainty is calculated taking one half of the instrument resolution. The resolution is 1 mm H<sub>2</sub>O, so one might estimate the probable measurement error as  $\pm 0.5$  mm H<sub>2</sub>O. However, it is very probable that a measurement could not be done with this type of accuracy. The meniscus in the barometer must be aligned by eye, and this has a least count of 2 mm. A measurement is made to the nearest millimeter, so the probable value of a single measurement would be expressed as  $30 \pm 1$  mm. Using the mid value of the range used to measure the average relative uncertainty (0 – 30 mm H<sub>2</sub>O), we have:

$$u_0 = \frac{\pm 1 \text{ mm H}_2\text{O}}{15 \text{ mm H}_2\text{O}} = \pm 0.0666$$

$$u_c = \frac{\pm 1 \text{ mm H}_2\text{O}}{15 \text{ mm H}_2\text{O}} = \pm 0.0666$$

These two uncertainties are combined in one to find the total uncertainty of the dynamic pressure.

$$u_{pd} = \sqrt{u_0^2 + u_c^2} = \sqrt{(\pm 0.0666)^2 + (\pm 0.0666)^2}$$

$$u_{pd} = 0.0942 \%$$

The uncertainty of the air density is negligible, so, the uncertainty of the air velocity is,

$$u_U = \pm \left[ \left( \frac{1}{2} (0.0942) \right)^2 \right]^{1/2}$$

$$u_U = \pm 0.0471 \quad \text{or} \quad u_U = \pm 4.71 \%$$

### **4.3.3 Uncertainty in temperature**

In the case of uncertainty in the temperature measurements, the procedure followed is the root-sum-squares (RSS) method. In this method, each elemental error is combined with other elemental errors to increase the uncertainty of the method. A realistic estimate of the uncertainty in the measurement,  $u_x$ , caused by these elemental errors can be computed by using the RSS method

$$u_x = \pm\sqrt{e_1^2 + e_2^2 + \dots + e_K^2}$$

$$u_x = \pm\sqrt{\sum_{j=1}^K e_j^2}$$

From the manufacturer, it was obtained the following data for the SCXI-1322 terminal block.

Accuracy: 1.2°C

Repeatability: 0.4°C

Using these data, it is possible to calculate an uncertainty for the terminal block.

$$u_B = \pm\sqrt{e_1^2 + e_2^2}$$

$$u_B = \pm\sqrt{(1.2^\circ C)^2 + (0.4^\circ C)^2}$$

$$u_B = \pm 1.265^\circ C$$

Knowing that the interval of the temperature measurement varied from 22°C to 85°C, the average relative uncertainty can be calculated.

$$u_B = \pm \frac{1.265^\circ C}{53.5^\circ C} = \pm 0.0236 \quad \text{or} \quad u_B = \pm 2.36 \%$$

The value 53.5°C is the mid value in the temperature range found when the temperature measurements were taken.

Also from the manufacturer of the thermocouples, it was found that these elements have a standard limit of error of 1.0°C. The resolution of the system used is equal to 0.01°C, so, the zero-order uncertainty is equal to ±0.005°C. The uncertainty of the thermocouples can be calculated as

$$u_{Th} = \pm\sqrt{e_1^2 + e_2^2}$$

$$u_{Th} = \pm\sqrt{(0.005^\circ C)^2 + (1.0^\circ C)^2}$$

$$u_{Th} = \pm 1.0^\circ C$$

The average relative uncertainty for the thermocouple is given by

$$u_{Th} = \pm \frac{1.0^\circ C}{53.5^\circ C} = \pm 0.0187 \quad \text{or} \quad u_{Th} = \pm 1.87 \%$$

The total uncertainty of the temperature measurement system is obtained applying the RSS method to all the data obtained.

$$u_T = \pm\sqrt{e_1^2 + e_2^2}$$

$$u_T = \pm\sqrt{(0.0236)^2 + (0.0187)^2}$$

$$u_T = \pm 0.0301 \text{ or } u_T = \pm 3.01 \%$$

So, it was shown that the measurements taken in this research have a good level of confidence, due to the small uncertainties found in this analysis.

## **CHAPTER 5**

### **RESULTS AND COMPARISONS**

In this Chapter, the experimental results generated in the research as well as comparisons between them and the theoretical results generated by the analytical solutions developed in Chapter 3 will be shown. Once all this work has been made and shown in this Chapter, a decision about which one of the theoretical models developed in the present work has the best prediction of the experimental data obtained. Following all the mentioned above, a very simple and practical way to predict the heat transfer in porous media will be obtained, which can be applied to the design of heat sinks and heat exchangers.

#### **5.1 COMPARISONS BETWEEN EXPERIMENTAL RESULTS AND ANALYTICAL SOLUTIONS**

In Chapter 4 we explained in detail the methodology used in the research in order to obtain the data presented here. Figure 5.1 and 5.2 present only experimental results which show the variation of the temperature distribution along the  $z$  axis (direction of the fluid flow) in the metal foam. These temperature distributions were obtained for different flow rates. Table 5.1 presents the air velocity that corresponds to each flow rate and the Reynolds number obtained with Eqn. 3.2. As it was explained in Chapter 4, the air velocity was obtained with an indirect method using a Pitot tube and measuring dynamic

pressure to transduce it to velocity. The different flow rates were obtained sliding a throttle plate that regulates the exit of the air.

Flow rate	Air velocity (m/s)	Pore Reynolds number
100%	5.386	84.735
80%	4.761	74.904
60%	4.258	66.994
40%	3.148	49.528
20%	1.74	27.378

**Table 5.1 Flow rates and air velocity**

Figure 5.1 shows the temperature distribution along the z axis when the Reynolds number at the pores is equal to 84.375, this is, when the flow rate is 100% of the total flow that is allowed to pass through the wind tunnel.

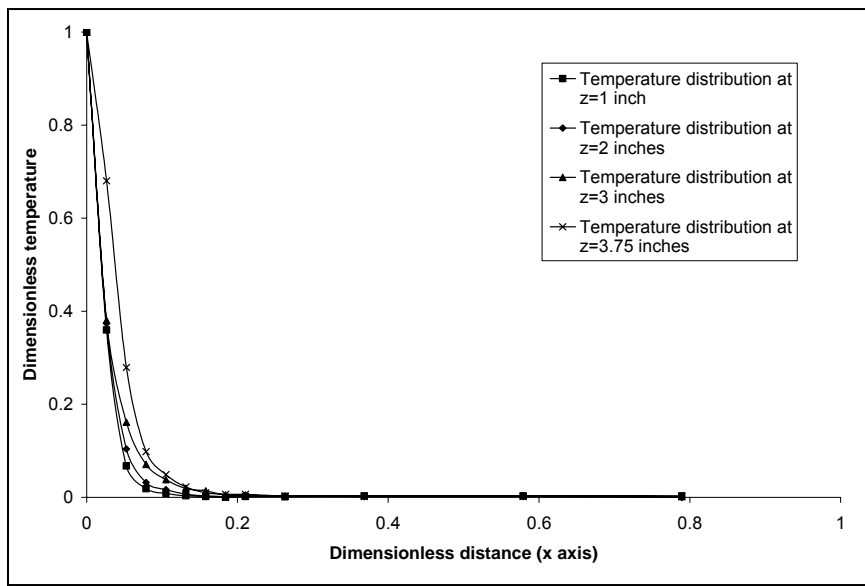


**Figure 5.1 Variation of the temperature distribution along z direction for Re=84.735**

The temperatures of the base and at the entrance of the foam, as well as the temperatures taken at different locations of the foam (Table 4.2), were substituted in Eqn. A.20. So, the dimensionless temperature was obtained for the different locations along the  $z$  axis. The distances shown along the  $x$  axis in Table 4.2 are divided between the total length of the metal foam in that direction. The dimensionless temperature was plotted versus the dimensionless distance along the  $x$  direction as given in the Figure 5.1. It can be seen how the temperature distribution is modified when the distance along the  $z$  direction is increased. When the position along  $z$  axis is close to the fluid entrance of the foam, the temperature drops faster, but when the position is far from the entrance, the temperature takes a little more distance in the  $x$  direction to drop. Figure 5.2 shows the same distributions, but when the flow rate is equal to 20% of the total flow rate allowed to pass by the wind tunnel, which corresponds to a pore Reynolds number of 27.378.

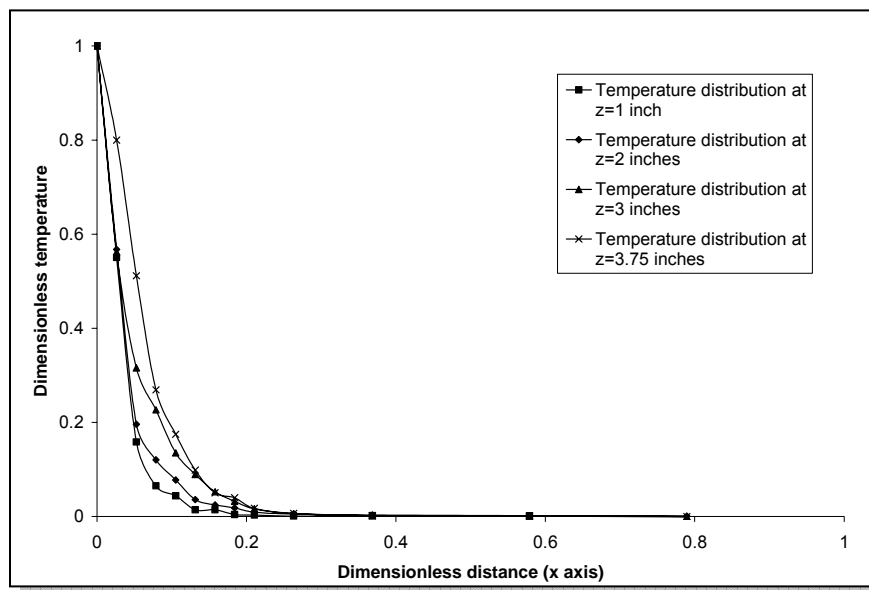
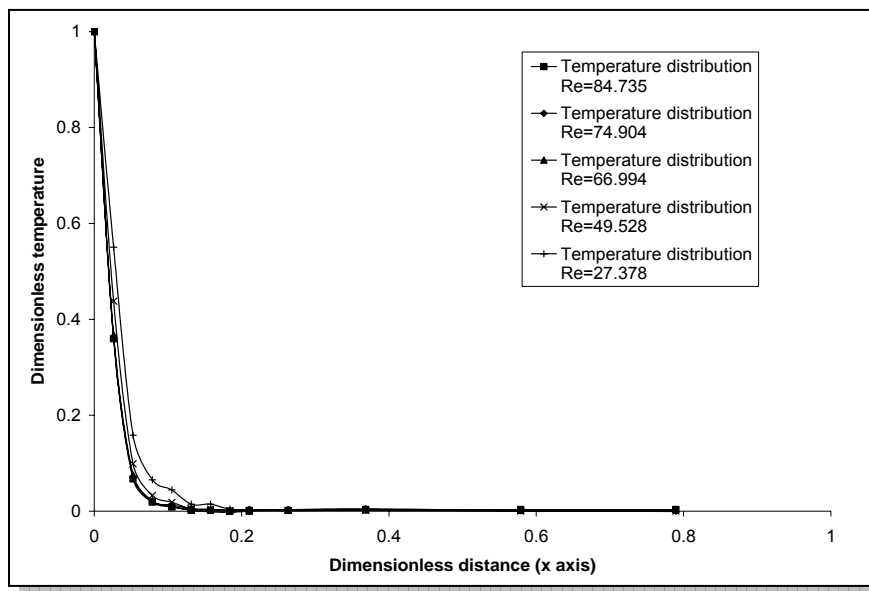


Figure 5.2 Variation of the temperature distribution along  $z$  direction for  $Re=27.378$

As it can be seen in the last figures, the variation of the temperature distribution is more notorious at low Reynolds numbers. If we compare the temperature distribution at 3.75 inches from the foam entrance to the temperature distribution at one inch from the entrance, it can be seen that these two distributions are more similar for the case presented in Figure 5.1 than the case shown in Figure 5.2. These comparisons were also made for the other Reynolds number presented in Table 5.1. When this was made, a relationship between the pore Reynolds number and the temperature distribution was found. This relation establishes that the lower the Reynolds number is, the higher is the variation in the temperature distribution along the  $z$  axis. Another way to analyze the temperature behavior is fixing the distance along the  $z$  direction and plotting the temperature distribution at different Reynolds numbers. Figure 5.3 shows the temperature distribution for different Reynolds numbers at one inch from the entrance.



**Figure 5.3 Variation of the temperature distribution for different Reynolds numbers at one inch from the entrance**

In the Fig, 5.3 it is observed how the temperature distribution drops in a small distance when the Reynolds number is high. For the next three Reynolds numbers, the temperature distribution is very similar, but it can be noticed that for  $Re=27.378$  the temperature takes more distance to drop, compared to other cases. Figure 5.4 shows the temperature distributions at different Reynolds numbers at a distance of 3.75 inches from the entrance. At this distance, it is more notorious that the temperature at  $Re=49.528$  and  $Re=27.378$  take more distance to reach a dimensionless temperature equal to zero.

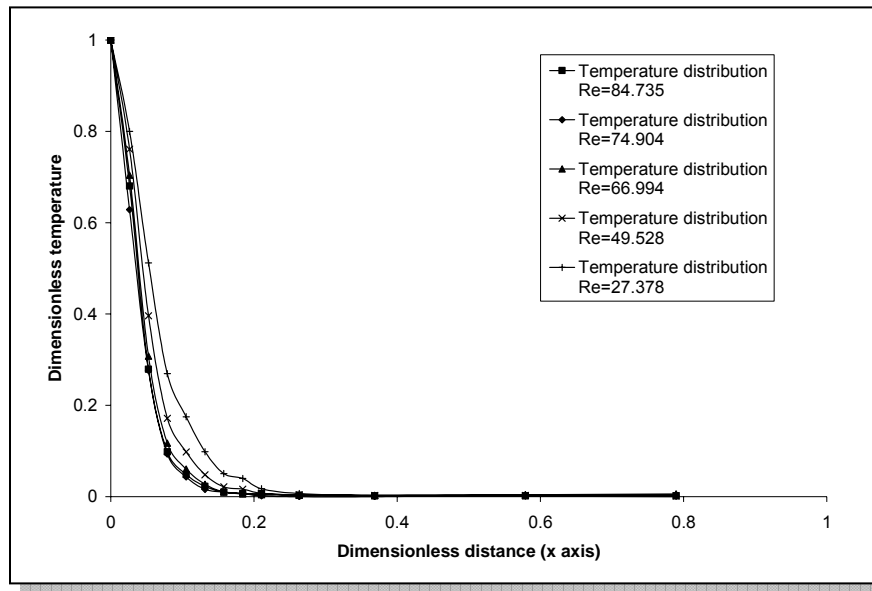


**Figure 5.4** Variation of the temperature distribution for different  $Re$  at 3.75 inches from the entrance

The analytical solutions obtained in Chapter 3 were plotted using Maple. Figure 5.5 shows the two-dimensional plotting of each case solved in Chapter 3.

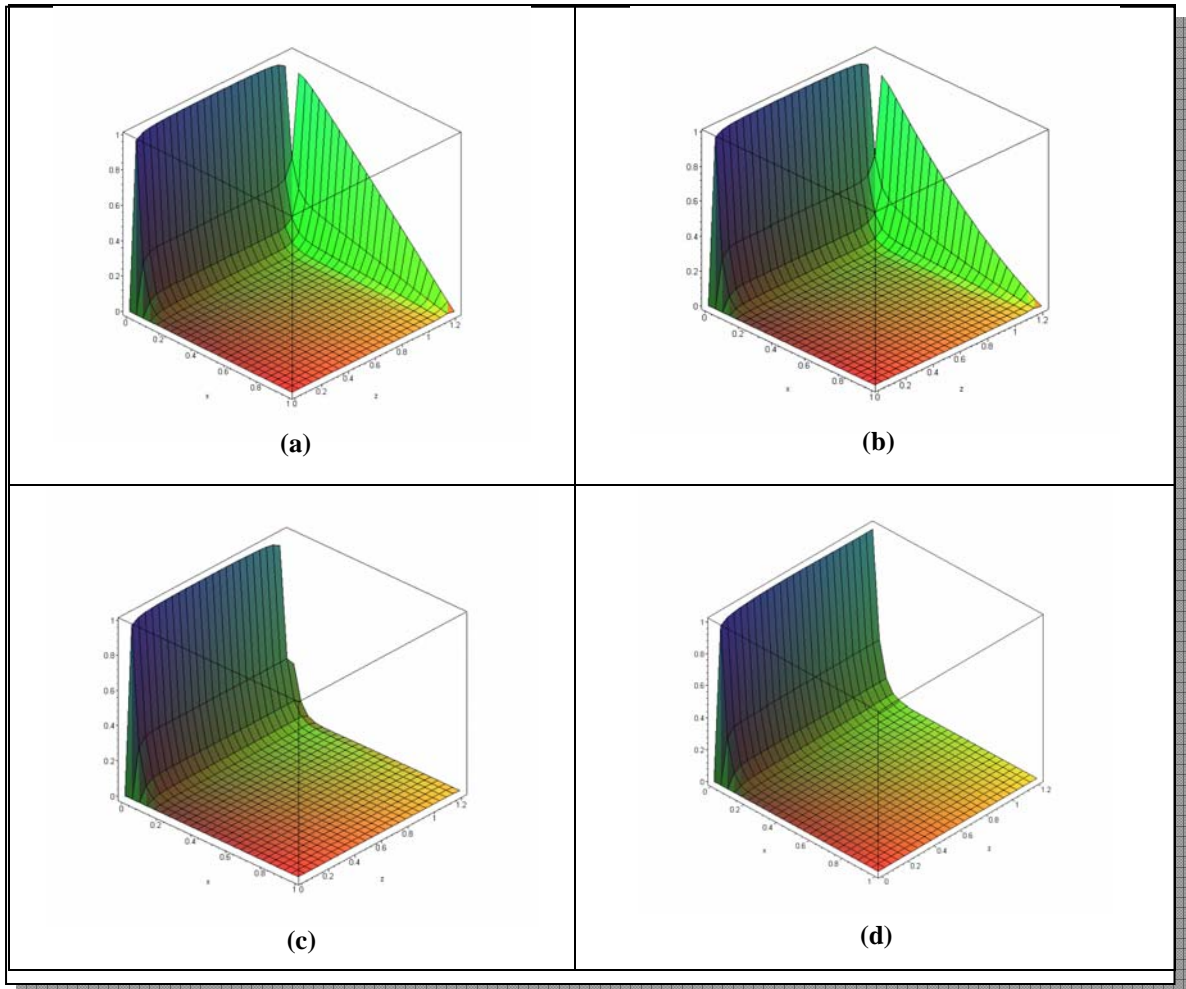


**Figure. 5.5 Two-dimensional plotting of proposed solutions. (a) Linear case. (b) Exponential case. (c) One-dimensional model case. (d) Zero slope case.**

We tried to determine how many terms of the infinite series solutions we need to obtain the dimensionless temperature distribution profiles. We begin obtaining the solution using a high number of terms, so, we choose 95 terms and obtained the temperature profiles. Then obtained the values of the temperature distribution for different number of terms, and we used 1, 5, 10, 25 and 45 terms.

The percentage of error between the values obtained with 95 terms and the values obtained with the numbers of terms mentioned was calculated. It would seem that we could use 25 terms to obtain a good solution, since that the maximum percentage of error found for this case was less than 1%. But when the graphs were plotted using this number, we realize that at  $x=0$ , the fluctuation of the temperature distribution on this border is high. As we know, the value of dimensionless temperature distribution at this border should be equal to one, but using 25 terms, we can visually determine that this value is still changing a lot along the  $z$  direction. Continuing increasing the number of terms and observing the resultant graphs, we determine that at 45 terms, the graph obtained is enough to consider the dimensionless temperature value good, this is due to at the border  $x=0$ , the temperature remains almost constant and equal to one. So, this number of terms (45) was used in the determination of the temperature profiles used in the graphs presented in this Chapter.

As it was explained before, these graphics were obtained using Maple. Using this program, it was possible to find some points belonging to the two-dimensional temperature distribution for the different cases. The distances in the  $z$  direction that were established in the experimental set-up were substituted in the equations and then the dimensionless temperature was calculated at different distances in the  $x$  direction. In that way, it was possible to compare the results given by the analytical modeling and the experiments. This was done for all the cases. Figure 5.6 shows the comparison between the results given by the analytical solution of the first case and the experiments. We used the convective heat transfer coefficient for  $Re=84.735$  in the analytical solution and the

data at the same Reynolds number for the temperature distribution generated by the experiments. The comparison was made for the data at one inch from the entrance. It can be appreciated that there is a good agreement between the two sets of data.

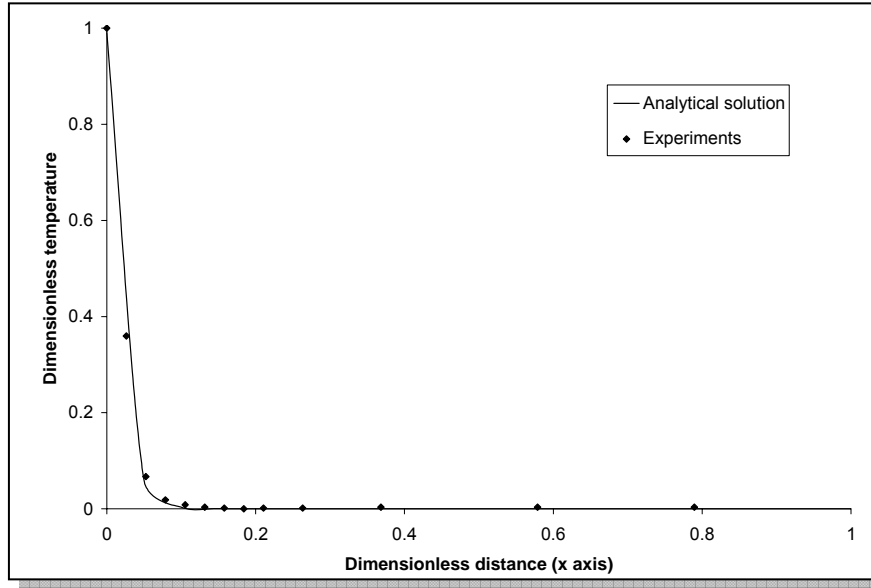


**Figure 5.6 Comparison between analytical and experimental data for  $Re=84.375$  at one inch from the entrance (first boundary condition case)**

The same comparison was made for the remaining four Reynolds numbers. All the comparisons showed a good agreement between the analytical solution and the experimental data at this distance from the fluid enhance (one inch). However, it was noticed a better adjustment for the cases in which the Reynolds number is greater. It can be shown comparing Figure 5.6 to Figure 5.7 which shows the comparison between the analytical solution and the experiments, at the same distance, and for the same case (first case, linear behavior), but at different flow velocity ( $Re=27.378$ ).

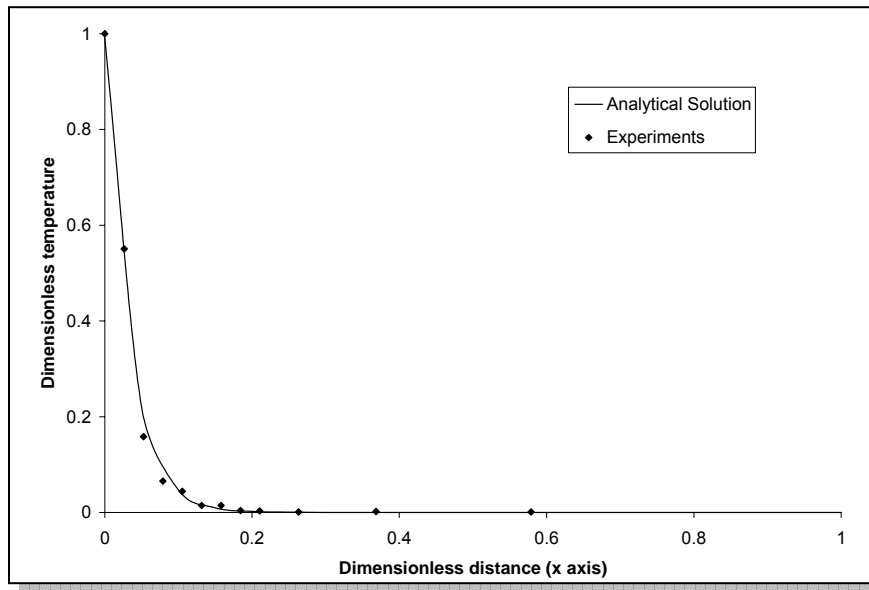


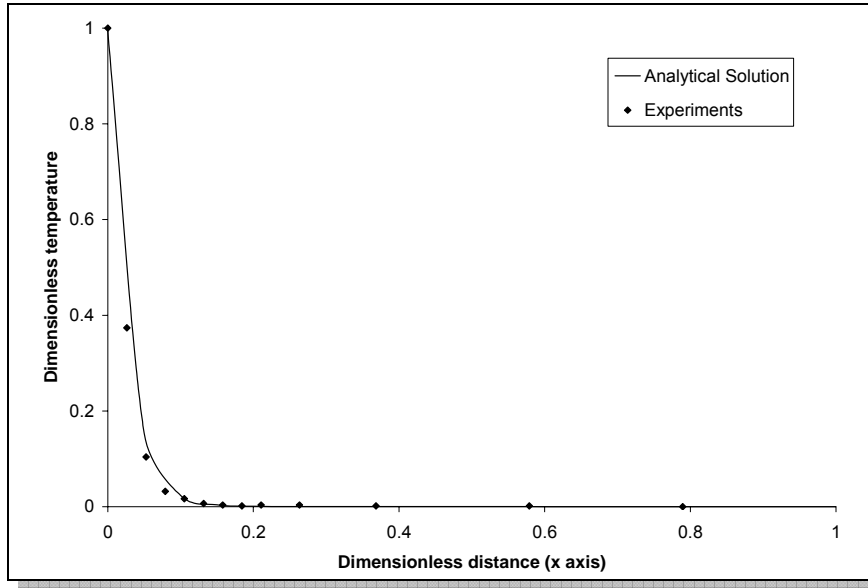
**Figure 5.7 Comparison between analytical and experimental data for  $Re=27.378$  at one inch from the entrance (first boundary condition case)**

It can be said that from the five cases corresponding to the different Reynolds number, the one presented in Figure 5.7 was the worst. However, the first case continues being a good approach.

The rest of the cases have a similar behavior. It means that at one inch from the entrance, none of the four cases analyzed in Chapter 3 had bad agreement, although all the cases gave evidence of better adjustment at high Reynolds numbers. The maximum error found between the analytical and experimental temperature distributions at this distance was 8% at  $Re=27.378$ .

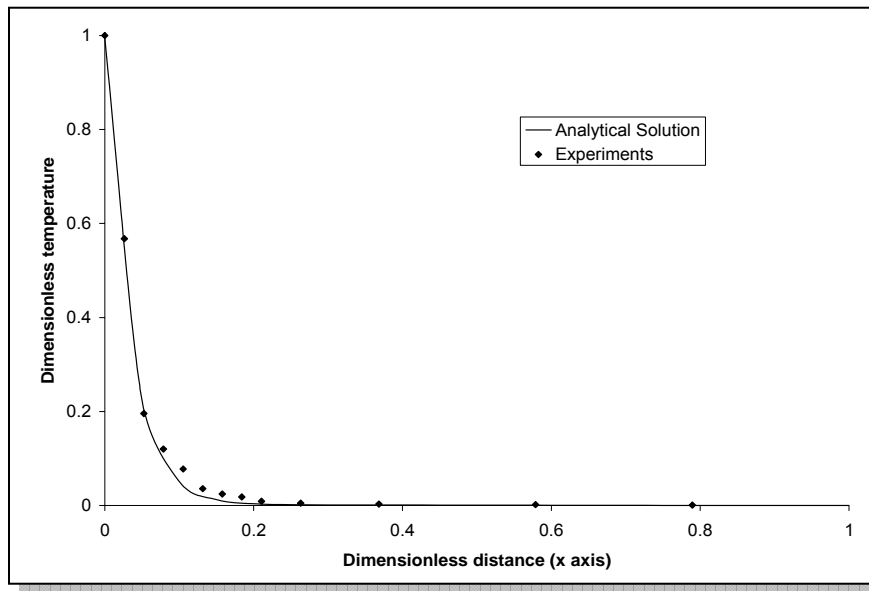
Analyzing the temperature distribution at two inches from the entrance, it was observed that the good agreement between analytical and experimental data continued, as

can be observed in Figure 5.8, which shows the comparison between the analytical and experimental data at two inches from the entrance, for a  $Re=84.735$  and having the linear behavior assumption at the boundary  $z=t$ .



**Figure 5.8 Comparison between analytical and experimental data for  $Re=84.735$  at two inches from the entrance (first boundary condition case)**

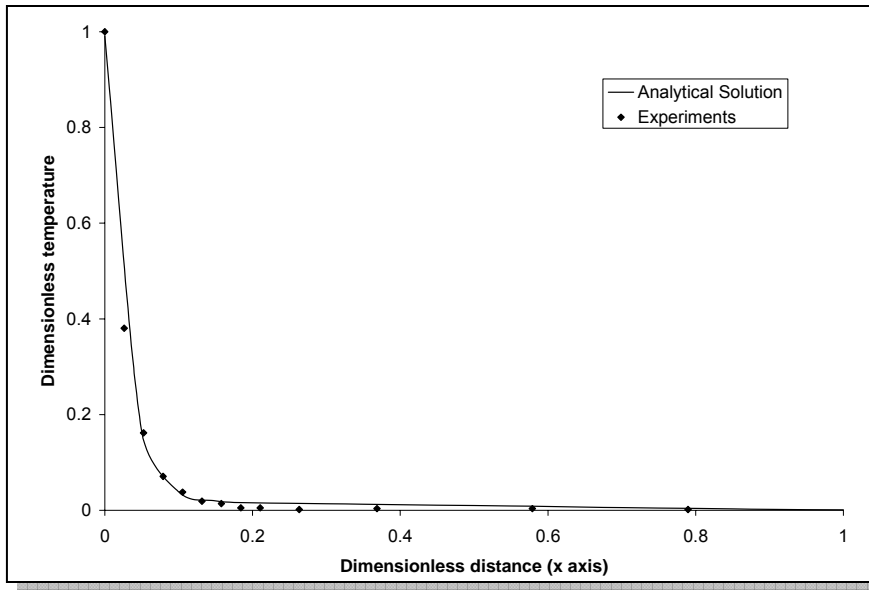
As the temperature distribution at one inch from the entrance, the analytic temperature distribution at two inches from the entrance has a better agreement with the experimental data at high Reynolds numbers. Figure 5.9 shows how the comparison between analytical and experimental data at  $Re=27.378$  has less concurrence than the comparison presented in Figure 5.8. It happens for all the different boundary conditions cases.



**Figure 5.9 Comparison between analytical and experimental data for  $Re=27.378$  at two inches from the entrance (first boundary condition case)**

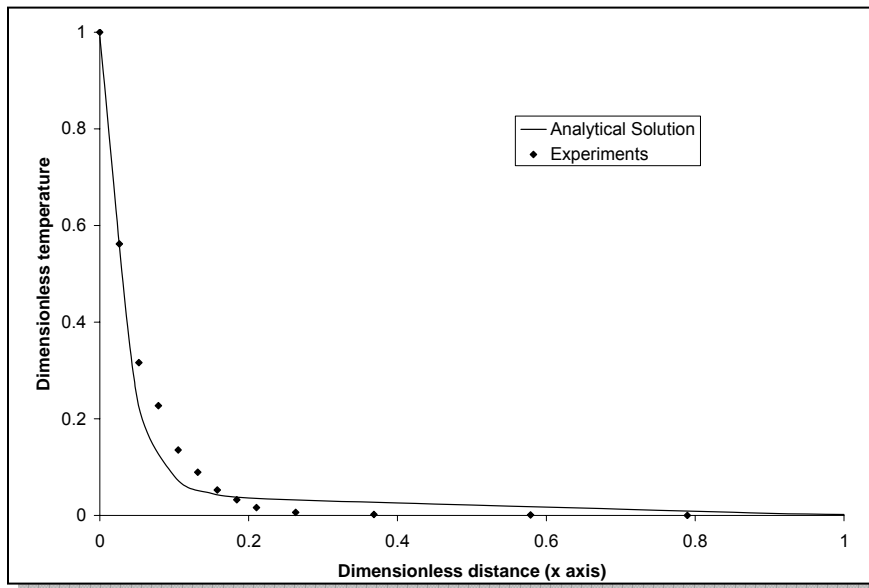
Until the moment the analytical solutions and the experimental data seem to be in agreement. However, it can be realized that things begin to change when the temperature distribution is studied at three inches from the air entrance.

At this distance (three inches), the analytical and experimental data do not have a concord as good as at the other distances. This behavior is shown in Figure 5.10 in which the analytical solution and the experimental data at three inches from the air entrance are compared for the linear boundary condition case and at a Reynolds number of 84.735.



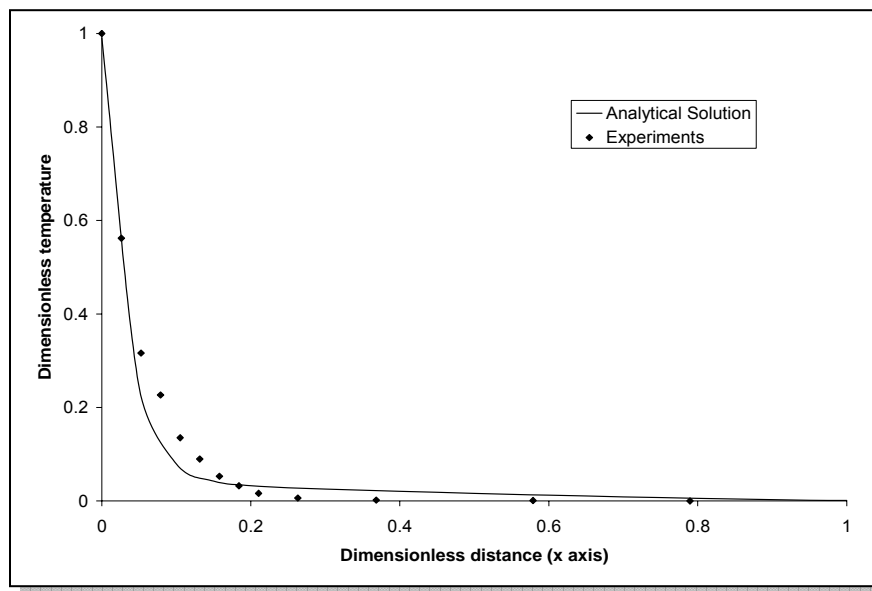
**Figure 5.10 Comparison between analytical and experimental data for  $Re=84.735$  at three inches from the entrance (first boundary condition case)**

The comparison shown by the Figure 5.10 shows still a good agreement. But when the Reynolds is diminished, the agreement is worst.



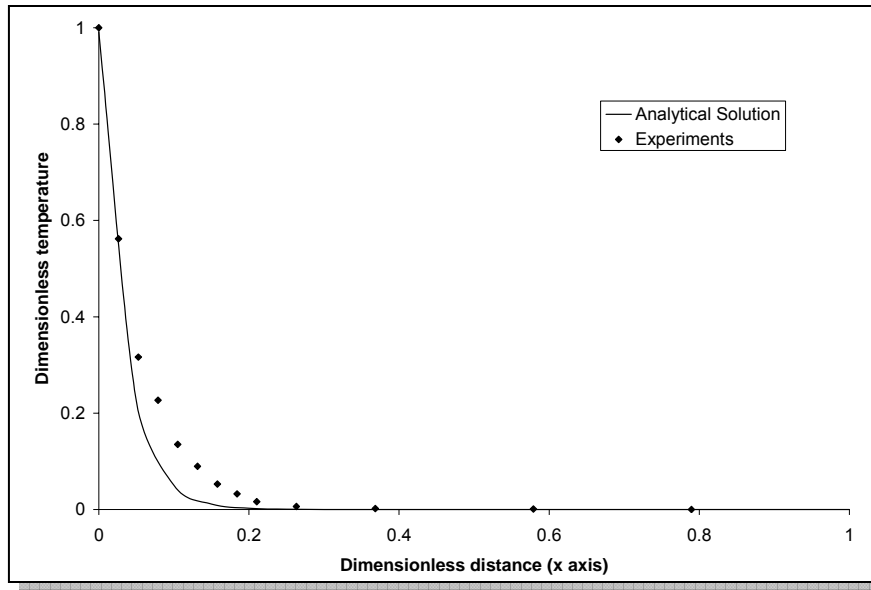
**Figure 5.11 Comparison between analytical and experimental data for  $Re=27.378$  at three inches from the entrance (first boundary condition case)**

Figure 5.11 shows the comparison at a Reynolds number of 27.378. At this distance, the cases for the different boundary condition at  $z=t$  begin to have poor agreement, mainly at low Reynolds numbers. Figure 5.12 show the behavior for the boundary condition with an exponential behavior.



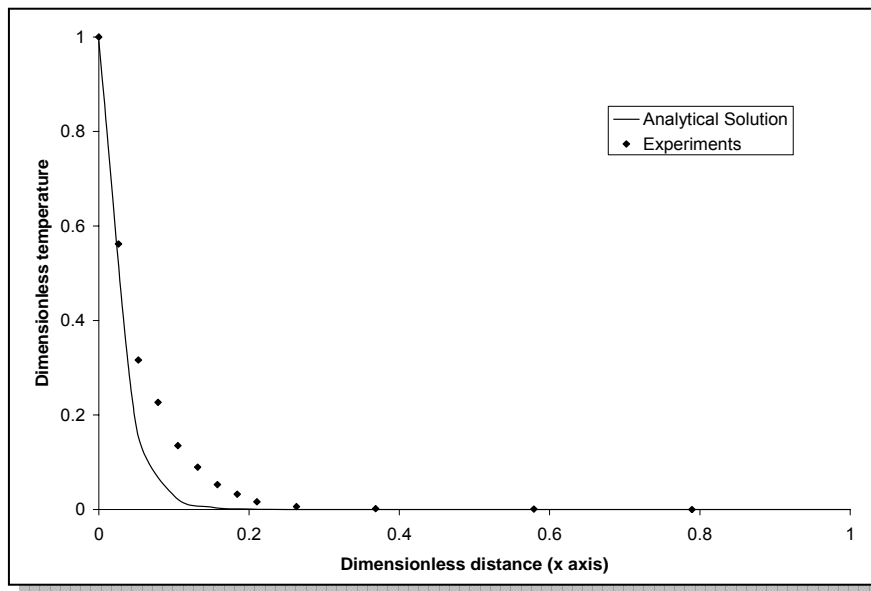
**Figure 5.12 Comparison between analytical and experimental data for  $Re=27.378$  at three inches from the entrance (second boundary condition case)**

Figure 5.13 shows the comparison at three inches from the entrance for the case in which the one-dimensional solution found by Dukhan and Quinones [21] is applied at the boundary  $z=t$ . It can be observed that this case shows a poorer agreement than the last two cases at this distance. The Reynolds number used in this comparison is equal to 27.378.



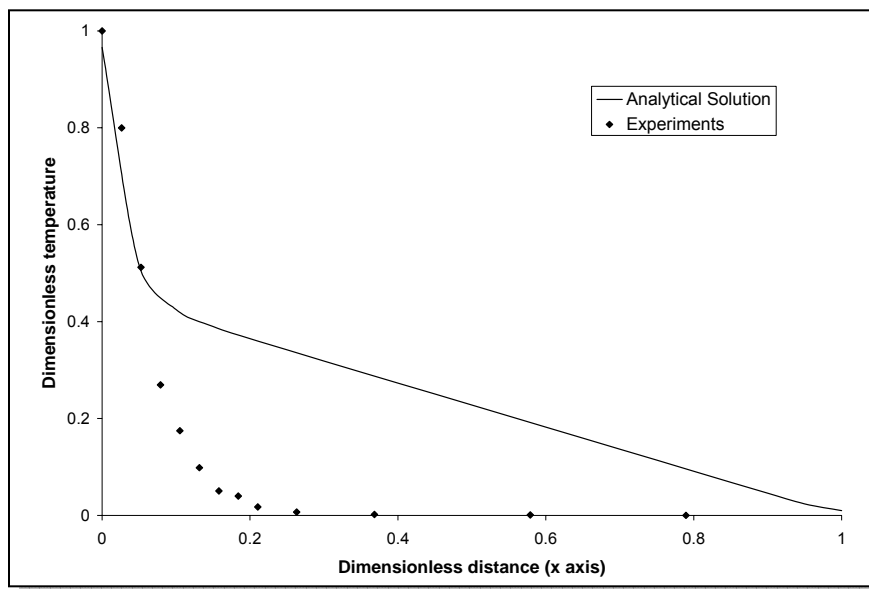
**Figure 5.13 Comparison between analytical and experimental data for  $Re=27.378$  at three inches from the entrance (third boundary condition case)**

For the fourth case in which it was proposed a zero slope at the boundary  $z=t$ , the comparison was similar to the last case presented.



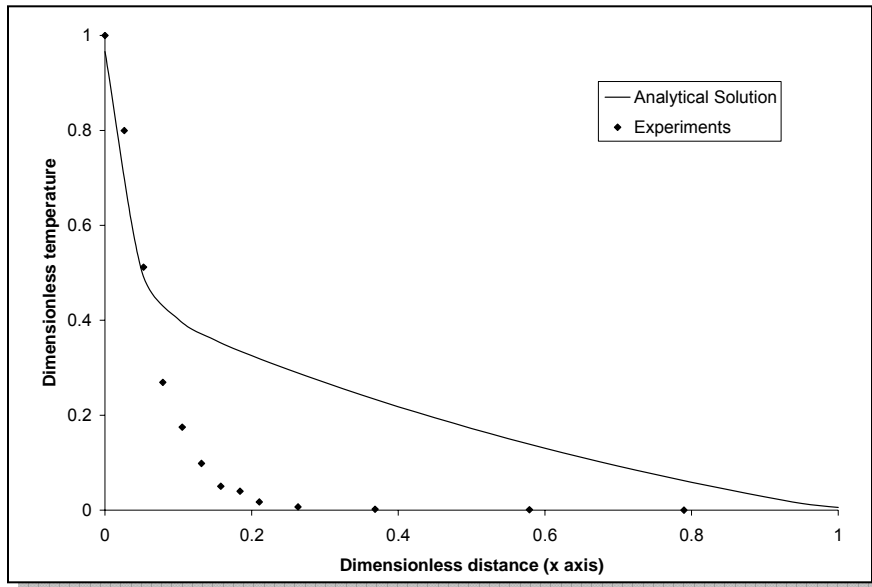
**Figure 5.14 Comparison between analytical and experimental data for  $Re=27.378$  at three inches from the entrance (fourth boundary condition case)**

Figure 5.14 shows the comparison for the fourth case at three inches from the entrance. This is the point in which it is arrived to the determination of the most appropriate boundary condition. The comparison between the analytical and experimental data is carried out at 3.75 inches from the face in which the air enters the foam. As it is remembered, the physical dimensions of the foam sample are 4" x 4" at the base, which means that the thermocouples are located at 0.25 inches from the air exit face. This distance is appropriate to determine the best boundary condition for the model developed in this research. Figure 5.15 shows the first case developed in the research at the distance mentioned. It is noticed a great difference between the distribution generated by the analytical solution and the experiments. This was made for  $Re=27.378$ , which was found to be the most critical condition. However, a very similar behavior was found for all the other temperature distribution generated at different Reynolds numbers.



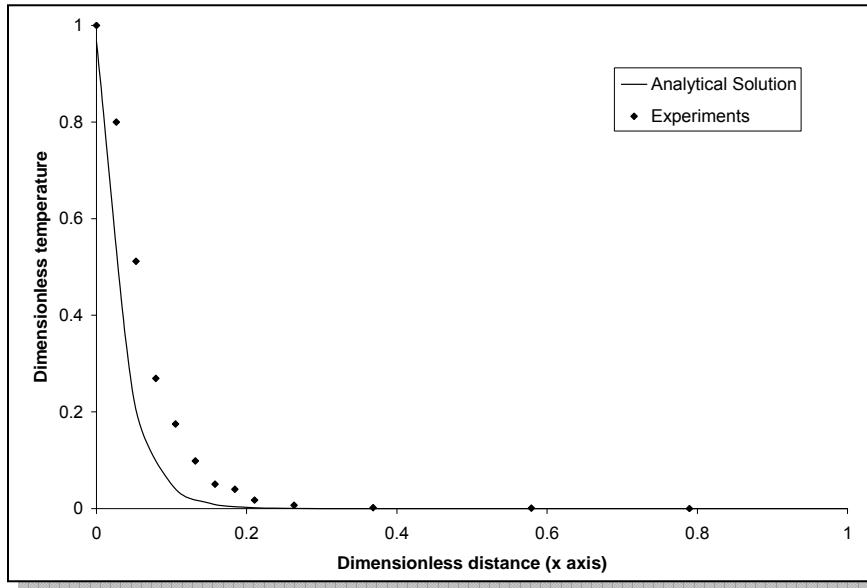
**Figure 5.15 Comparison between analytical and experimental data for  $Re=27.378$  at 3.75 inches from the entrance (first boundary condition case)**

Figure 5.16 shows the comparison under the same conditions as the last case, but for the case in which the boundary condition has an exponential behavior. Again, a poor agreement between the analytic and experimental results is observed.



**Figure 5.16 Comparison between analytical and experimental data for  $Re=27.378$  at 3.75 inches from the entrance (second boundary condition case)**

An improvement is observed for the remaining cases. For the third boundary condition case, a better adjustment than the last cases is observed. Figure 5.17 shows the comparison corresponding to this case.



**Figure 5.17 Comparison between analytical and experimental data for  $Re=27.378$  at 3.75 inches from the entrance (third boundary condition case)**

The Figure 5.18 represents the fourth case which has a similar behavior than the case presented before.

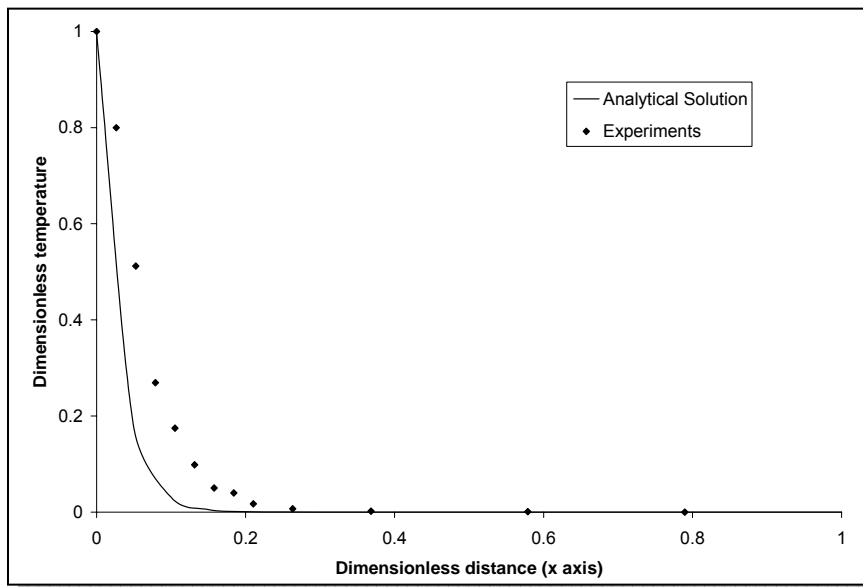


**Figure 5.18 Comparison between analytical and experimental data for  $Re=27.378$  at 3.75 inches from the entrance (fourth boundary condition case)**

## 5.2 DETERMINATION OF THE PARAMETER M VARIATION ALONG THE Z DIRECTION

As it can be seen, none of analytical solutions presented has a good fit with the experimental data. However, observing the graphs plotted and doing an error analysis, we can determine that the last case is the one that has the better approach to the experimental data. But the maximum error found is about 33% and it is an indicative that something is bad with the model employed. So, we had to focus on the parameters that cause the modification of the temperature distribution along the z direction. Doing this, we realize that the parameter that determines the modification of the temperature distribution is the convective coefficient  $h_{fm}$  in the foam sample. In our equations, we considered this coefficient as a constant value, and it generates that the temperature profile does not change along the z direction, as it can be observed in Figure 5.19.

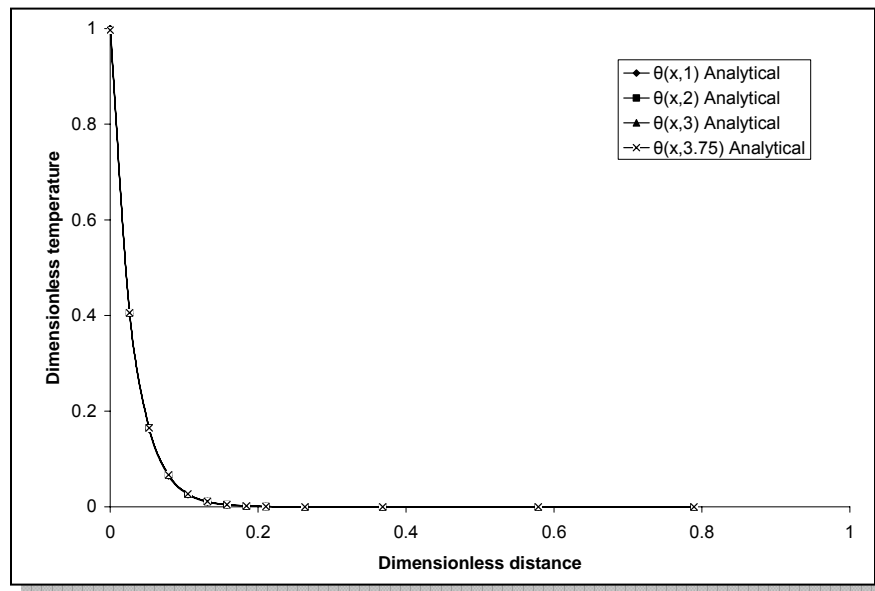


Figure 5.19 Plot of the analytical solution (fourth case) data for  $Re=27.378$

As we know, the convective coefficient inside the foam depends on the Nusselt number, that depends on the Reynolds number and the last depends on the velocity at the pores. But, how is this dependence? To know it, we use the data generated from the experiments and we applied a linear regression to these in order to study the temperature behavior at the boundary  $z=t$ . Then, the boundary condition at  $z=t$  is of the form

$$\theta_{fm} = e^{-a_{fm}X} \quad (5.1)$$

In order to linearize Eqn. 5.1, it was applied natural logarithm to both sides of the equation:

$$\ln \theta_{fm} = -a_{fm}X \quad (5.2)$$

It can be seen that Eqn. 5.2 has the form  $y = a_0 + a_1x$ . So,  $y = \ln \theta_{fm}$  and  $a_1 = -a_{fm}$ .

The objective of the linear regression analysis is to find the value of the coefficient  $a_{fm}$ . A linear regression analysis is applied to each set of data corresponding to a few flow rates. Table 5.2 shows the values for  $a_{fm}$  obtained.

Flow rate	Coefficient $a_{fm}$
100%	28
80%	28
60%	28
40%	23
20%	18

**Table 5.2 Coefficient  $a_{fm}$  for different flow rates**

By varying the temperature profile in the sample along the z direction, we establish a linear relation between the coefficient  $a_{fm}$  and the coefficient  $M$  derived from all the correlations presented in Chapter 3. Linear relation has the form  $M(Z) = a_0 + a_1Z$ , and the boundary conditions for this equation are @Z=0,  $M(Z)=M$  and @Z=t/L,  $M(Z)=a_{fm}$ . Once that the boundary conditions are applied to the equation

$$M(Z) = M + \frac{LZ}{t}(a_{fm} - M) \quad (5.3)$$

We have to keep in mind that this variation dependent on the variation of the coefficient  $h_{fm}$  and in turn the last dependent on the velocity at the pores. In that way, an important conclusion obtained during the comparison of the analytical and experimental results is that the velocity profile of the air at the pores is reduced when the air flow advances in the z direction. This is something logical, since the air encounters a lot of aluminum filaments in its way and it represent resistance to the flow. That's the reason by which the velocity is reduced in the z direction, and also the reason by which the

convective coefficient along the z direction is reduced too. Having made these conclusions and having obtained Eqn. 5.3, this is substituted in Eqn. 3.26.

$$\theta_{jm}(X, Z) = \sum_{n=0}^{\infty} \frac{2}{\pi \left(n + \frac{1}{2}\right)} \left\{ \cosh \left[ \sqrt{M(Z)^2 + \frac{L^2 \pi^2 \left(n + \frac{1}{2}\right)^2}{t^2}} X \right] - \tanh \left[ \sqrt{M(Z)^2 + \frac{L^2 \pi^2 \left(n + \frac{1}{2}\right)^2}{t^2}} \right] \sinh \left[ \sqrt{M(Z)^2 + \frac{L^2 \pi^2 \left(n + \frac{1}{2}\right)^2}{t^2}} X \right] \right\} \sin \left[ \frac{L \pi \left(n + \frac{1}{2}\right)}{t} Z \right] \quad (5.4)$$

Equation 5.4 is plotted at the distances in study. We can see in Figure 5.20 that now the temperature distribution is changing along the z direction and the behavior is very similar to the temperature behavior showed by the experiments. Equation 5.4 was plotted for the case in which  $Re=27.378$ .

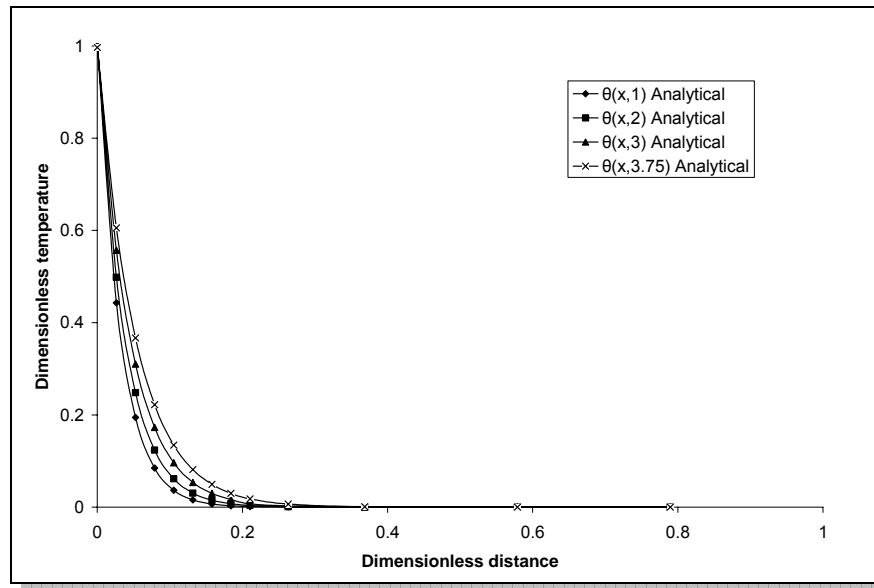


**Figure 5.20** Plot of the analytical solution (fourth case) with the parameter M varying along the z direction.

When we plot Eqn. 5.4 at the distances where the temperature distributions are studied, we found an excellent agreement for all the Reynolds number cases.

Figures 5.21 to 5.24 show the comparison between the new analytical solution and the experimental data at 1, 2, 3 and 3.75 inches from the entrance. All the comparisons showed in the mentioned figures were plotted for the case in which  $Re=27.378$ , but as we mentioned some lines before, the good agreement was observed for the five Reynolds number cases.

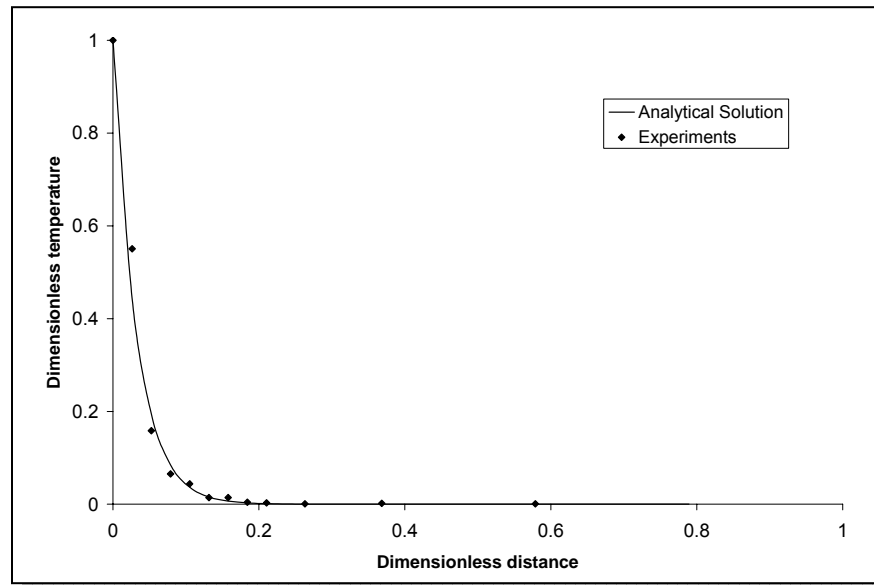


**Figure 5.21 Comparison between analytical and experimental data for  $Re=27.378$  at 1 inch from the entrance (fourth boundary condition case with  $M(Z)$ )**

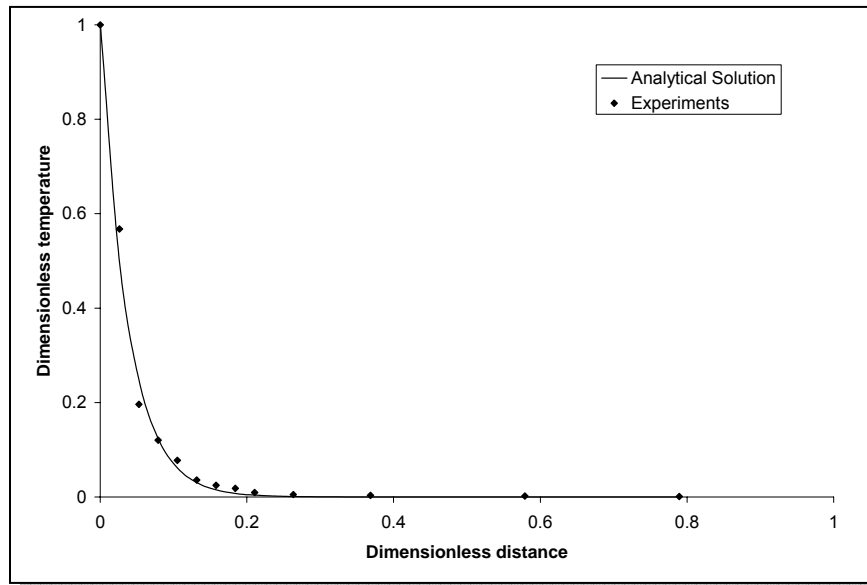


**Figure 5.22 Comparison between analytical and experimental data for  $Re=27.378$  at 2 inches from the entrance (fourth boundary condition case with  $M(Z)$ )**

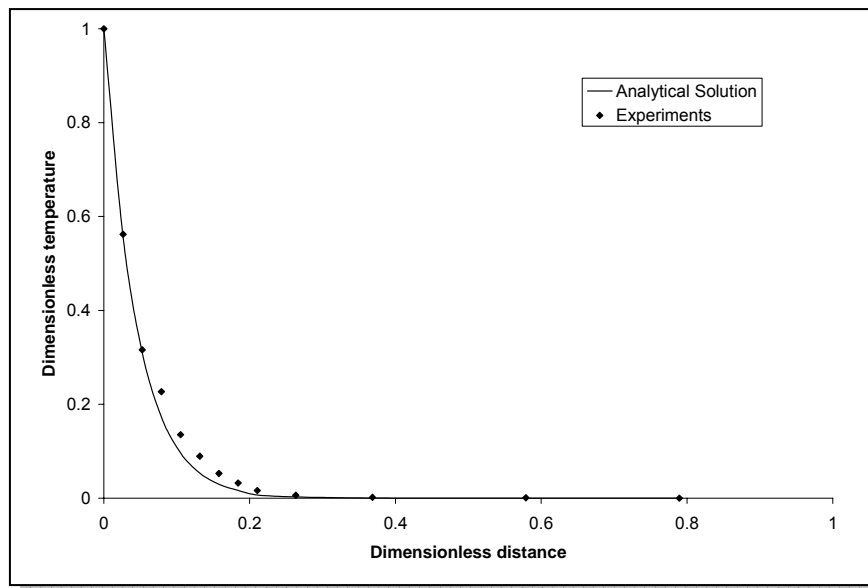


**Figure 5.23 Comparison between analytical and experimental data for  $Re=27.378$  at 3 inches from the entrance (fourth boundary condition case with  $M(Z)$ )**

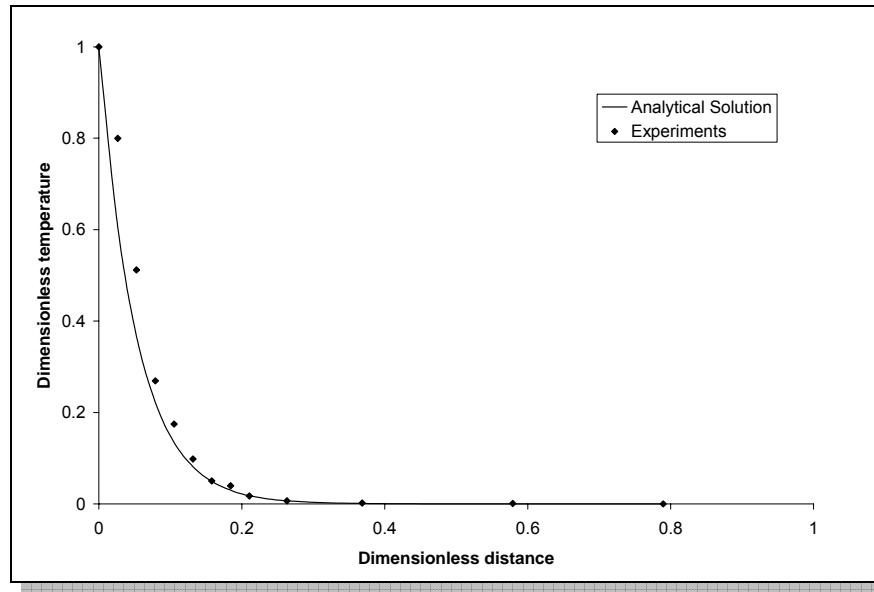


**Figure 5.24 Comparison between analytical and experimental data for  $Re=27.378$  at 3.75 inches from the entrance (fourth boundary condition case with  $M(Z)$ )**

The error analysis carried out showed a maximum error of less than 10% in all cases and the major part of the error oscillated between 0 and 3%, which means an excellent approach. So, we conclude that this model represents very well the temperature distribution in the foam sample.

It must be remembered that the coefficient  $a_{fm}$  used in this model depends on the flow velocity of the air incoming to the foam sample. When the Reynolds numbers are high, the coefficient remains almost constant, suffering only little variations, but when the Reynolds number decrease to 49.528, the coefficient begins to change. So, it can be said that the coefficient  $a_{fm}$  is function of the Reynolds number at low values of it.

$$\begin{aligned}
a_{fm} &= 28 & \text{Re} &\geq 67 \\
a_{fm} &= 0.2513\text{Re} + 10.948 & 0 &< \text{Re} < 67
\end{aligned}
\tag{5.5}$$

It is important to mention that these correlations were obtained with the experimental data generated from one sample of metal foam, so that; this correlation applies only to a sample with the characteristics described in Chapter 4. To obtain more general correlations, we would have to work with more than one sample with different dimensions.

### 5.3 SIMPLIFIED SEMI-ANALYTICAL SOLUTION FOR THE TEMPERATURE FIELD IN METAL FOAM

Once that we obtained an analytical model that could describe the heat transfer in an open cell metal foam sample, we were focused on obtaining a simplified semi-analytical solution for the temperature distribution inside the sample. The proposed pseudo two-dimensional solution for Eqn. 3.14 has the form

$$\frac{\theta_{fm}}{\theta_b} = e^{-m_{fm}x} f(z)
\tag{5.6}$$

Using the dimensionless parameters defined in Chapter 3 for temperature, distance and the foam parameter, Eqn. 5.6 is transformed to Eqn. 5.7.

$$\theta_{fm} = e^{-MX} f(Z) \quad (5.7)$$

Equation 5.7 is substituted in the two-dimensional derivation for heat transfer in dimensionless form represented by Eqn. 3.14.

Doing the derivations and working with the algebra, we obtain

$$M^2 e^{-MX} f(Z) + e^{-MX} f''(Z) - M^2 e^{-MX} f(Z) = 0$$

Doing simplification, it is found that:

$$f''(Z) = 0 \quad (5.8)$$

Solution of Eqn. 5.8 has the form,

$$f(Z) = AZ + B \quad (5.9)$$

From our experience deriving the two-dimensional model for the metal foam sample, it is observed that at the boundary  $Z=0$ , the dimensionless temperature has the form,

$$\theta_{fm} = e^{-MX} \quad (5.10)$$

And at the boundary  $Z=t/L$ , the dimensionless temperature distribution is obtained from a treatment of the experimental data, so

$$\theta_{fm} = e^{-a_{fm}X} \quad (5.11)$$

Substituting Eqn. 5.10 and Eqn. 5.11 in Eqn. 5.7 the boundary conditions to find the constants of Eqn. 5.9 are obtained. The boundary conditions are:

$$\begin{aligned} @Z=0; \quad e^{-MX} &= e^{-MX} f(Z) & f(Z) &= 1 \\ @Z=t/L; \quad e^{-a_{fm}X} &= e^{-MX} f(Z) & f(Z) &= e^{(M-a_{fm})X} \end{aligned}$$

Substituting the boundary conditions in Eqn. 5.9 the constants A and B are found.

$$A = \frac{L}{t} \left[ e^{(M-a_{fm})X} - 1 \right]; \quad B=1;$$

Substituting the constants in Eqn. 5.9:

$$f(Z) = \frac{LZ}{t} \left[ e^{(M-a_{fm})X} - 1 \right] + 1 \quad (5.12)$$

Finally, substituting Eqn. 5.12 in Eqn. 5.7, the simplified two-dimensional solution for the dimensionless heat transfer in the metal foam sample is found.

$$\theta_{fm} = \frac{LZ}{t} \left[ e^{-a_{fm}X} - e^{-MX} \right] + e^{-MX} \quad (5.13)$$

When we plot Eqn. 5.13 and compare these graphs with the experimental data, we found a very good agreement in which the maximum percentage error found was less than 10%, practically the same level of confidence as the total analytical solution. Figures 5.25 to 5.28 shows the comparisons between the semi-analytical solution and the experiments for a pore Reynolds number of 84.375 at different distances along the  $z$  direction.

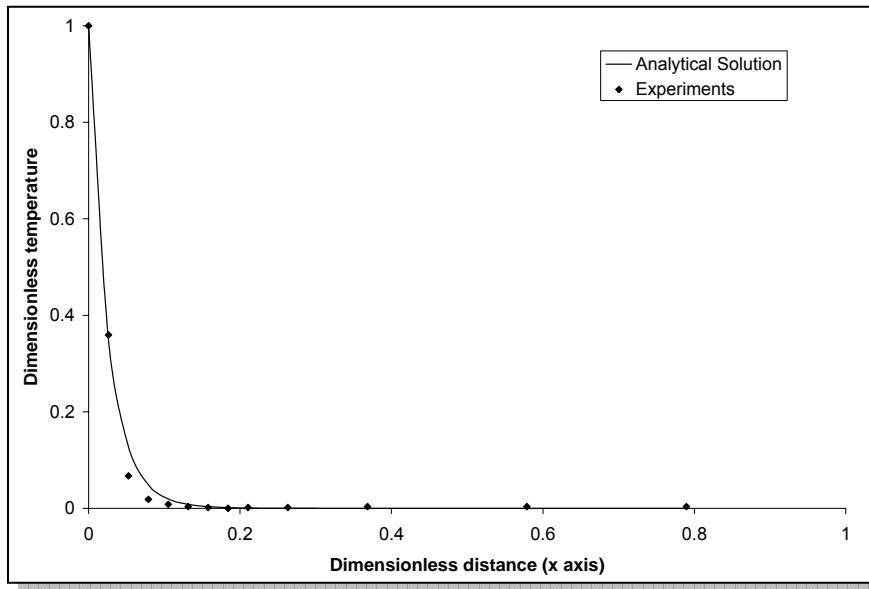


**Figure 5.25 Comparison between semi-analytical and experimental data for Re=84.375 at 1 inch from the entrance.**

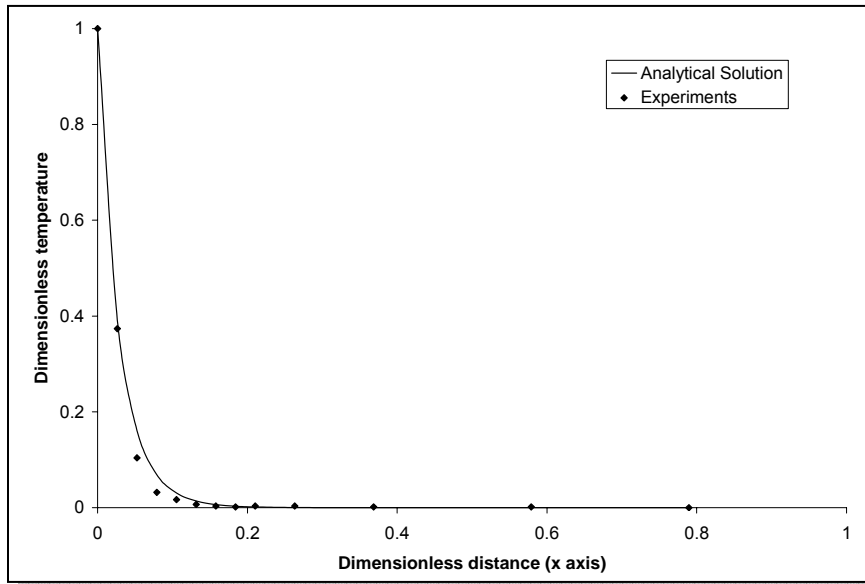


**Figure 5.26 Comparison between semi-analytical and experimental data for  $Re=84.375$  at 2 inches from the entrance.**

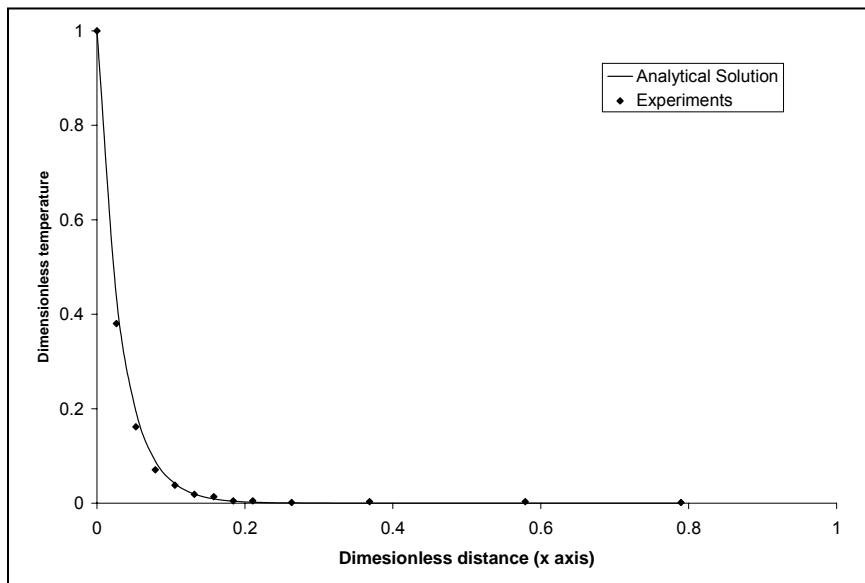


**Figure 5.27 Comparison between semi-analytical and experimental data for  $Re=84.375$  at 3 inches from the entrance.**

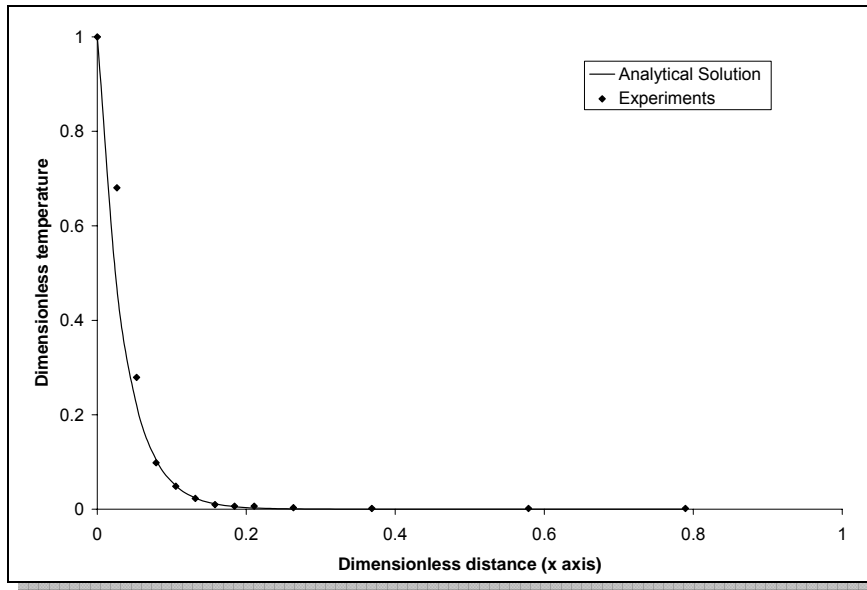


**Figure 5.28 Comparison between semi-analytical and experimental data for  $Re=84.375$  at 3.75 inches from the entrance.**

In Figs. 5.29 to 5.32 we present the comparison between the same semi-analytical solution and the experiments but at  $Re=27.378$ .

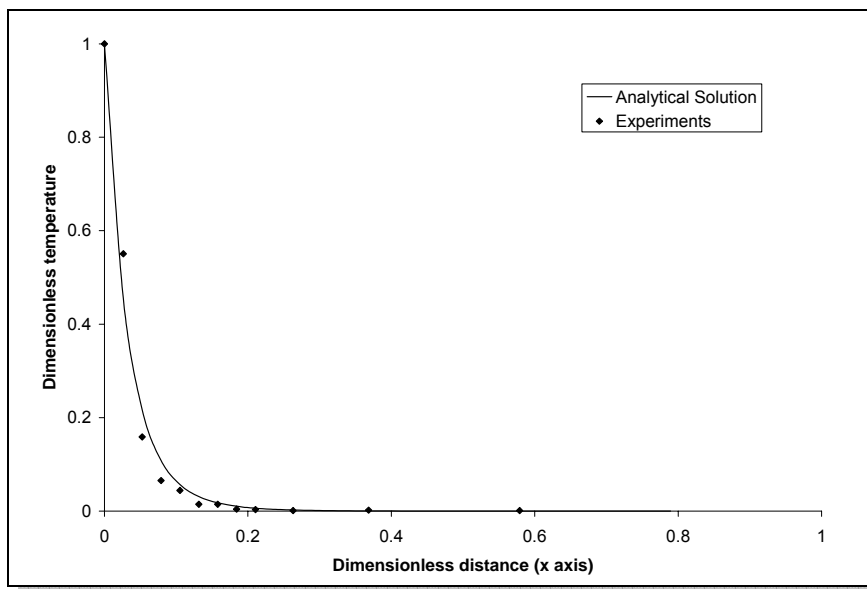


**Figure 5.29 Comparison between semi-analytical and experimental data for  $Re=27.378$  at 1 inch from the entrance.**

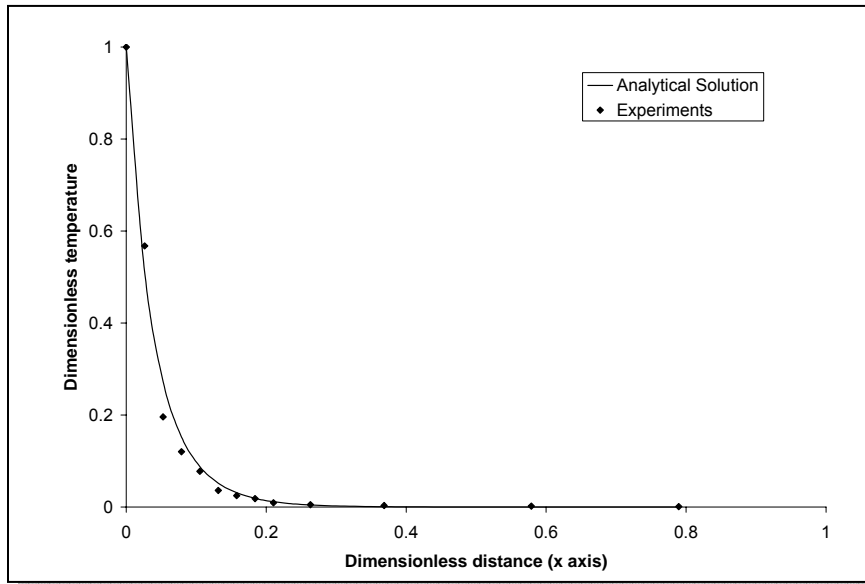


**Figure 5.30 Comparison between semi-analytical and experimental data for  $Re=27.378$  at 2 inches from the entrance.**

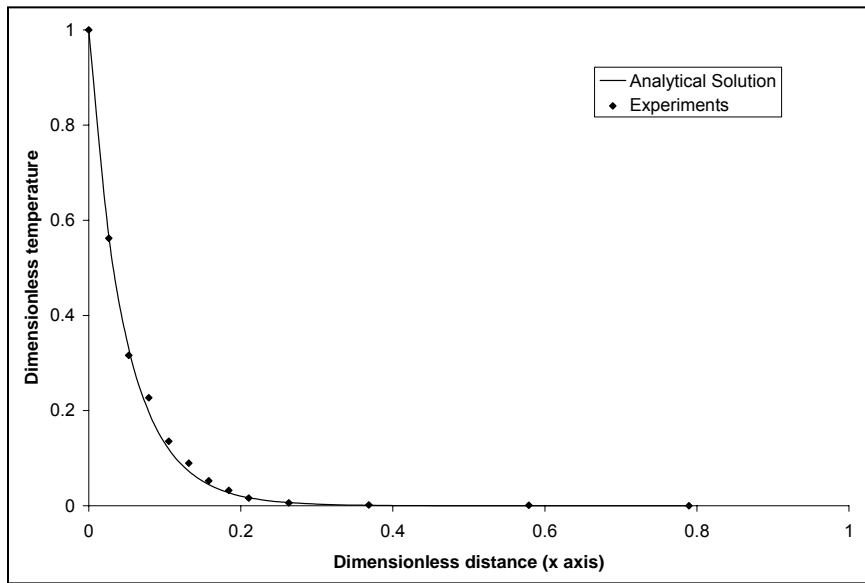


**Figure 5.31 Comparison between semi-analytical and experimental data for  $Re=27.378$  at 3 inches from the entrance.**

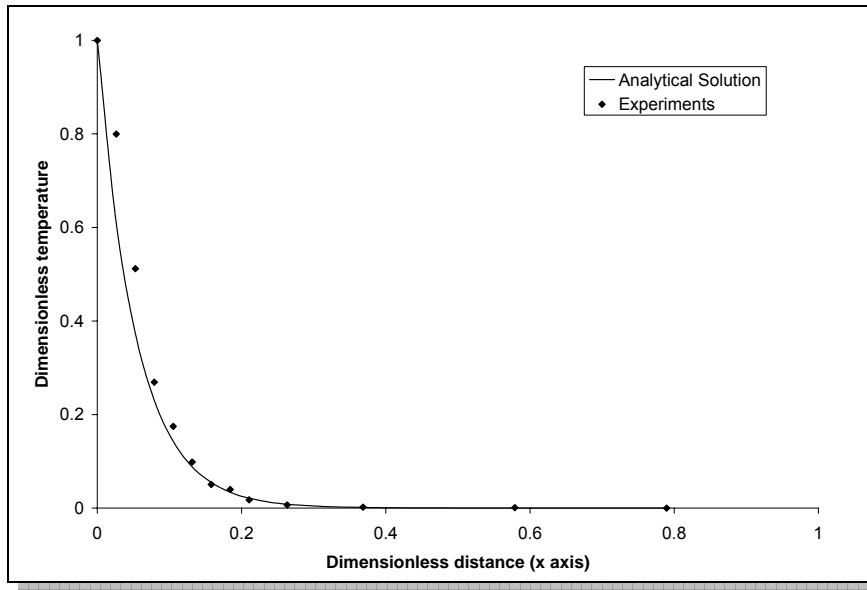


**Figure 5.32 Comparison between semi-analytical and experimental data for  $Re=27.378$  at 3.75 inches from the entrance.**

As it can be seen, the agreement is as good as the agreement reached at high Reynolds numbers. With these graphs, we have shown that the semi analytical solution developed in this Chapter can be also used to model the temperature distribution inside the foam sample.

## CHAPTER 6

### CONCLUSIONS AND RECOMMENDATIONS

The most important conclusions reached during this work are:

- It was found that the temperature distribution in a metal foam sample with the characteristics described in this thesis presents a modification along the direction of the flow that is used to dissipate the heat to which the sample is being exposed.
- It was found that the best way to find the temperature distribution inside the foam is to set the boundary condition where the air leaves the sample as a zero slope condition. This means that the temperature is increasing along the  $z$  direction and it reaches its maximum value at the boundary where the air leaves the foam.
- The convective coefficient derivated from the correlations referenced in this thesis is not constant throughout the whole sample. It is varying along the  $z$  direction and this is precisely the parameter that modifies the temperature distribution along the mentioned direction.
- The variation of the convective coefficient is attributed to a reduction in the velocity at the pores when the air advances in the  $z$  direction and it is due to the resistance that the foam structure presents to the air to flow.

- The analytical solution to model the temperature distribution includes a parameter  $a_{fm}$  determined from experimental data. This parameter is a function of the Reynolds number when the value of this is low. This relationship between the coefficient  $a_{fm}$  and the Reynolds number is expressed by Eqn. 5.5.

The study of materials as the metal foam is exciting and very interesting. With this research we have learned a lot about how others have modeled the heat transfer in this kind of materials, and we have realized by ourselves that there are a lot of parameters that could affect the heat transfer in the metal foams under convection. The experience gained along the development of this research allows us to make some recommendations for future work related to this topic. Some recommendations are:

- As we have explained, until this moment we only have had the opportunity to work with one foam sample. The correlations founded worked well with our analytical solution and our experiments. However, it is necessary to extend the correlations obtained developing more experiments with more samples of different sizes and physical structure, like the pore density, pore size, filament diameter, relative density, etc. If it would be possible to work with samples larger in the z direction, it would be possible to obtain correlations for the parameter  $a_{fm}$  that could be a function of the thickness of the sample as well as the Reynolds number at the pores.
- As we explained in Chapter 5, we proposed a linear variation for the convective coefficient  $h_{fm}$  and therefore a linear variation for the parameter  $M$

since that  $M$  is function of  $h_{fm}$ . We conclude that this is good because the percentage of error results in less than 10%. Doing more experiments with different samples we could realize if it continues being true, that is, if the relation found for  $M$  continues to be linear or it takes a different form at some distance along the  $z$  direction.

- Another issue present in our research was the ambient conditions under which the experiments were run. May be it would be positive to run experiments in a more controlled ambient, specifically free of humidity. We can not be sure that this is affecting our results, but may be they could.
- Of course, we would like to propose our work to be applied to practical situations in which the metal foam are used as a heat sink to cool computer microprocessors or to construct heat exchangers.

## REFERENCES

- [1]. Bastawros, A. F., 1998, "Effectiveness of Open-Cell Metallic Foams for High Power Electronic Cooling", Proceeding Symposium on the Thermal Management of Electronics, IMECE. Anaheim, CA.
- [2]. Boomsma, K., Poulikakos, D. and Zwick, F., 2003, "Metal Foams as Compact high Performance Heat Exchangers", *Mechanics of Materials*. Vol. 35, pp. 1161-1176.
- [3]. Zhao, C.Y., Lu, T.J., Hodson, H.P. and Jackson, J.D., 2004, "The Temperature Dependence of Effective Thermal Conductivity of Open-Celled Steel Alloy Foams", Vol. 367, pp. 123-131.
- [4]. Vafai, K. and Tien, C. L., 1982, "Boundary and Inertia Effects on Convective Mass Transfer in Porous Media", *International Journal of Heat and Mass Transfer*. Vol. 25, pp. 1183-1190.
- [5]. Writz, R. A., 1997, "A Semi-Empirical Model for Porous Media Heat Exchanger Design", Proceedings of the American Society of Mechanical Engineers National Heat Transfer Conference, Baltimore, MD.
- [6]. Lu, T.J., Stone, H.A. and Ashby, M.F., 1998, "Heat Transfer in Open Cell Metal Foams", *Acta Metallurgica Inc*. Vol. 46, No. 10, pp. 3619-3635.
- [7]. Kiwan, S. and Al-Nimr, M.A., 2001, "Using Porous Fins for Heat Transfer Enhancement", *Journal of Heat Transfer*. Vol. 123, pp. 790-795.
- [8]. Younis, L.B. and Viskanta, R., 1993, "Experimental determination of the Volumetric Heat Transfer Coefficient Between Stream of Air and Ceramic Foam", *International Journal of Heat and Mass Transfer*. Vol. 36, pp. 1425-1434.
- [9]. Decker, S., Mößbauer, S., Nemoda, S., Trimis, D. and Zapf, T., 2000, "Detailed Experimental Characterization and Numerical Modeling of Heat and Mass Transport Properties of Highly Porous Media for Solar Receivers and Porous Burners", Lehrstuhl für Strömungsmechanik Universität Erlangen-Nürnberg Cauerstr. 4, D-91058 Erlangen, Germany.

- [10]. Calmidi, V.V. and Mahajan, R. L., 2000, "Forced Convection in High Porosity Metal Foams", *Journal of Heat Transfer*. Vol. 122, pp. 557 – 565.
- [11]. Phanikumar M. S. and Mahajan R.L., 2002, "Non-Darcy Natural Convection in high Porosity Metal Foams", *International Journal of Heat and Mass Transfer*. Vol. 45, pp. 3781-3793.
- [12]. Pan, H.L., Pickenacker, O., Pickenacker, K., Trimis, D., Moßbauer, S. Wawrzinek, K. and Weber, T., 1999, "Experimental Determination of Effective Heat Conductivities of Highly Porous Media", Institute of Fluid Mechanics, University of Erlangen-Nuremberg Cauerstr. 4, D-91058 Erlangen, Germany.
- [13]. Sullines, D. and Daryabeige, K., 2001, "Effective Thermal Conductivity of High Porosity Open Cell Nickel Foam", *Proceeding, 35<sup>th</sup> AIAA Thermophysics Conference*, Anaheim, CA.
- [14]. Zumbrennen, D.A., Viskanta, R. and Incropera F.P., 1986, "Heat Transfer through Porous Solids with Internal Geometries", *International Journal of Heat and Mass Transfer*. Vol. 29, pp. 275-284.
- [15]. Hunt, M. L. and Tien, C. L., 1988, "Effects of Thermal Dispersion on Forced Convection in Fibrous Media", *International Journal of Heat and Mass Transfer*. Vol. 31, pp. 301-309.
- [16]. Bastawros, A.F., Evans A.G. and Stone H.A., 1999, "Evaluation of Cellular Metal Heat Transfer Media", Division of Engineering and Applied Sciences. Harvard University. Cambridge, MA 02138.
- [17]. Boomsma, K. and Poulikakos, D., 2000, "On the Effective Thermal Conductivity of a Three-Dimensionally Structured Fluid-Saturated Metal Foams", *International Journal of Heat and Mass Transfer*. Vol. 44, pp. 827-836.
- [18]. Ozmat, B., Leyda, B. and Benson, B., 2002, "Applications of Open Cell Metal Foams", Personal communications with ERG Materials and Aerospace Corp. Oakland, CA.
- [19]. Bhattacharya, A., Calmidi, V. V. and Mahajan, R. L, 2002, "Thermophysical Properties of High Porosity Metal Foams", *International Journal of Heat and Mass Transfer*. Vol. 45, pp. 1017-1031.

- [20]. Bhattacharya, A. and Mahajan, R. L., 2002, “Finned Metal Foam Heat Sinks for Electronics Cooling in Forced Convection”, *Journal of Electronic Packaging*. Vol. 124, pp. 155 – 163.
- [21]. Dukhan, N. and Quinones, P., 2003, “Convective Heat Transfer Analysis of Open Cell Metal Foam for Solar Air Heaters”, *Proceeding International Solar Energy Conference*, Hawaii, USA.
- [22]. Dae-Young Lee and Vafai K., 1998, “Analytical characterization and conceptual assessment of solid and fluid temperature differentials in porous media”. , *International Journal of Heat and Mass Transfer*.
- [23]. Incropera, F. P. and De Witt, D. P., 2002, *Fundamentals of Heat and Mass Transfer*, John Willey & Sons. New York, USA. pp. 130-133.
- [24]. Ashby, M., Evans A., Fleck, N.A., Gibson, L.J., Hutchinson, J.W. and Wadley, H.N.G., 2000, *Metal Foams, a Design Guide*, Butterworth-Heinemann. United States. pp. 181-186.
- [25]. Arpaci, V. S., 1966, *Conduction Heat Transfer*, Addison-Wesley Publishing Company. Michigan, USA. pp. 126 – 128.
- [26]. Ozisik, M.N., 1993, *Heat Conduction*, John Wiley & Sons, Inc. New York, USA, pp. 1-94.
- [27]. Kaviany, M., 1999, *Principles of Heat Transfer in Porous Media*, Springer. New York USA. pp. 17-20.

**APPENDIX A**  
**DERIVATION OF ENERGY EQUATION**

Energy equation to model heat transfer inside the foam is derivate in next lines. Figure 3.6, shows the cross sectional areas for different heat fluxes. The heat conduction area in the solid part is given as,

$$A_{cond} = A_c - A_p \quad (\text{A.1})$$

where  $A_c$  is the total cross sectional area and  $A_p$  is the area occupied by the pores. This area was approximated by Sullines and Daryabeige [13]:

$$A_{cond} = A_c(1 - \varepsilon) \quad (\text{A.2})$$

where  $\varepsilon$  is the porosity of the foam and it is a property reported by the manufacturer. Following the last arrangement the conduction area for the solid part, the  $x$  direction is defined by Eqn. A.3 as,

$$dA_{cond(x)_s} = W(1 - \varepsilon)dz \quad (\text{A.3})$$

Air is also a heat conductor, although not as efficient. However, in order to get a good approximation, the heat conduction in the air is considered by defining the area occupied by the pores through Eqn. A.4

$$dA_{cond(x)_f} = W\varepsilon dz \quad (\text{A.4})$$

Similarly, in the  $z$  direction, the conduction areas for the solid aluminum filaments and the air are defined by Eqns. A.5 and A.6 respectively.

$$dA_{cond(z)_s} = W(1 - \varepsilon)dx \quad (A.5)$$

$$dA_{cond(z)_f} = W\varepsilon dx \quad (A.6)$$

The convective surface area is defined using the property of surface density ( $\sigma$ ), that is the surface area per unit volume. This property is specified by the manufacturer.

$$\sigma = \frac{A_{conv}}{Wdx dz} \quad (A.7)$$

where  $A_{conv}$  is the surface area through which heat transfer by convection takes place. Fourier's law of conduction is used to define the energy fluxes in the  $x$  and  $z$  directions, and it is considered for the solid part and the air present inside the foam. It must be noted that different conductivities are employed for heat conduction for the solid part and air. These conductivities are denoted by  $k_s$  and  $k_f$  respectively.  $T_{fm}$  is the local averaged temperature inside the foam. The heat flux entering the control volume in the  $x$  direction is,

$$q_x = -k_s A_{cond(x)_s} \frac{\partial T_{fm}}{\partial x} - k_f A_{cond(x)_f} \frac{\partial T_{fm}}{\partial x} \quad (A.8)$$

Using the conduction areas defined by Eqns. A.2 to A.6, Eqn. A.8 is modified to,

$$q_x = -k_s W dz \frac{\partial T_{fm}}{\partial x} + (k_s - k_f) W \varepsilon dz \frac{\partial T_{fm}}{\partial x} \quad (\text{A.9})$$

A similar analysis is made for the heat flux by conduction leaving the control volume:

$$q_{x+dx} = q_x + \frac{\partial q_x}{\partial x} dx \quad (\text{A.10})$$

Substituting Eqn. A.9 into Eqn. A.10, we obtain the heat flux that leaves the metal foam in the x direction:

$$q_{x+dx} = -k_s W dz \frac{\partial T_{fm}}{\partial x} + (k_s - k_f) W \varepsilon dz \frac{\partial T_{fm}}{\partial x} - k_s W dz \frac{\partial^2 T_{fm}}{\partial x^2} dx + (k_s - k_f) W \varepsilon dz \frac{\partial^2 T_{fm}}{\partial x^2} dx \quad (\text{A.11})$$

For the conduction heat fluxes in the z direction we followed the same procedure. The equations obtained in this way are

$$q_z = -k_s W dx \frac{\partial T_{fm}}{\partial z} + (k_s - k_f) W \varepsilon dx \frac{\partial T_{fm}}{\partial z} \quad (\text{A.12})$$

$$q_{z+dz} = -k_s W dx \frac{\partial T_{fm}}{\partial z} + (k_s - k_f) W \varepsilon dx \frac{\partial T_{fm}}{\partial z} - k_s W dx \frac{\partial^2 T_{fm}}{\partial z^2} dz + (k_s - k_f) W \varepsilon dx \frac{\partial^2 T_{fm}}{\partial z^2} dz \quad (\text{A.13})$$

Newton's law of cooling is employed for the convection heat transfer inside the pores. The effective convection coefficient defined by Eqn. 3.10 is introduced in the heat

transfer equations to calculate the temperature distribution in the metal foam. At this point, the convection area includes the property of surface density which is incorporated in the analysis.

$$q_{conv} = h_{fm} A_{conv} (T_{fm} - T_{\infty}) = h_{fm} \sigma \cdot W dx dz (T_{fm} - T_{\infty}) \quad (A.14)$$

Equations A.9 and A.11 to A.14 are substituted into Eqn. A.7 to obtain,

$$\begin{aligned} & -k_s W dz \frac{\partial T_{fm}}{\partial x} + (k_s - k_f) W \varepsilon dz \frac{\partial T_{fm}}{\partial x} - k_s W dx \frac{\partial T_{fm}}{\partial z} + (k_s - k_f) W \varepsilon dx \frac{\partial T_{fm}}{\partial z} = \\ & -k_s W dz \frac{\partial T_{fm}}{\partial x} + (k_s - k_f) W \varepsilon dz \frac{\partial T_{fm}}{\partial x} - k_s W dz \frac{\partial^2 T_{fm}}{\partial x^2} dx + (k_s - k_f) W \varepsilon dz \frac{\partial^2 T_{fm}}{\partial x^2} dx \\ & -k_s W dx \frac{\partial T_{fm}}{\partial z} + (k_s - k_f) W \varepsilon dx \frac{\partial T_{fm}}{\partial z} - k_s W dx \frac{\partial^2 T_{fm}}{\partial z^2} dz + (k_s - k_f) W \varepsilon dx \frac{\partial^2 T_{fm}}{\partial z^2} dz \\ & \quad + h_{fm} \sigma \cdot W dx dz (T_{fm} - T_{\infty}) \end{aligned} \quad (A.15)$$

which is simplified as,

$$\begin{aligned} & k_s W dz \frac{\partial^2 T_{fm}}{\partial x^2} dx - (k_s - k_f) W \varepsilon dz \frac{\partial^2 T_{fm}}{\partial x^2} dx + k_s W dx \frac{\partial^2 T_{fm}}{\partial z^2} dz - (k_s - k_f) W \varepsilon dx \frac{\partial^2 T_{fm}}{\partial z^2} dz \\ & \quad - h_{fm} \sigma \cdot W dx dz (T_{fm} - T_{\infty}) = 0 \end{aligned} \quad (A.16)$$

Dividing by  $W dx dz$  and making some algebraic arrangements, the heat transfer through the metal foam is expressed as,

$$\frac{\partial^2 T_{fm}}{\partial x^2} + \frac{\partial^2 T_{fm}}{\partial z^2} - \frac{h_{fm} \sigma}{k_s(1-\varepsilon) + k_f \varepsilon} (T_{fm} - T_\infty) = 0 \quad (\text{A.17})$$

The term relating the convective coefficient, the surface area and the conductivities of the solid and fluid, as well as the porosity of the metal foam is the foam parameter and is given by,

$$m_{fm}^2 = \frac{h_{fm} \sigma}{k_s(1-\varepsilon) + k_f \varepsilon} \quad (\text{A.18})$$

Substituting the foam parameter in Eqn. A.17, yields,

$$\frac{\partial^2 T_{fm}}{\partial x^2} + \frac{\partial^2 T_{fm}}{\partial z^2} - m_{fm}^2 (T_{fm} - T_\infty) = 0 \quad (\text{A.19})$$

In order to non-dimensionalize the equation and establish the proper boundary conditions, an analysis of the conditions to which the foam will be subjected during the experimentation is made. A constant heat flux will be applied to the base of the foam by means of a flat heater. In [22] is considered that applying a constant heat flux at the base of a metal foam sample, it causes that the entire base can be considered remain at a constant temperature  $T_b$ . Also, the experimental verification of this assumption was validated in our case taking measurements at different locations along the entire base. The inlet temperature of the fluid is denoted by  $T_\infty$ . So, a dimensionless temperature  $\theta_{fm}$  is

defined as the ratio of the difference between the local temperature in any point in the foam and the inlet temperature of the fluid and the difference between the constant temperature  $T_b$  at the base of the foam and  $T_\infty$ .

$$\theta_{fm}(x, z) = \frac{T_{fm}(x, z) - T_\infty}{T_b - T_\infty} \quad (\text{A.20})$$

The distance across the x and z direction are also non-dimensionalize as,

$$X = \frac{x}{L} \qquad Z = \frac{z}{L}$$

and, for the foam parameter

$$L^2 m_{fm}^2 = M^2$$

Thus, a dimensionless form of Eqn. A.19 is obtained as,

$$\frac{\partial^2 \theta_{fm}}{\partial X^2} + \frac{\partial^2 \theta_{fm}}{\partial Z^2} - M^2 \theta_{fm} = 0 \quad (\text{A.20})$$

**APPENDIX B**  
**MATHEMATICAL PROCEDURES**

### **Case 1. Temperature distribution with linear behavior**

We begin to solve this case substituting Eqn. 3.19 into Eqn. 3.16, two separate partial differential equations are obtained. The first equation is

$$\frac{\partial^2 \Psi}{\partial X^2} + \frac{\partial^2 \Psi}{\partial Z^2} - M^2 \Psi = 0 \quad (\text{B.1})$$

Equation B.1 corresponds to the first one of the two models presented in Figure 3.8. This means that the boundary conditions defined in the model of Figure 3.8 will be applied to the Eqn. B.1 in order to solve it to know the temperature distribution. Separation of variables is applied to the Eqn. B.1 to begin its solution, so

$$\Psi(X, Z) = X_1(X)Z_1(Z) \quad (\text{B.2})$$

substituting Eqn. B.2 in Eqn. B.1;

$$X_1'' Z_1 + X_1 Z_1'' - M^2 X_1 Z_1 = 0$$

Dividing by  $X_1 Z_1$

$$\frac{X_1''}{X_1} + \frac{Z_1''}{Z_1} - M^2 = 0 \quad (\text{B.3})$$

The terms of Eqn. B.3 can be represented as constants;

$$\frac{X_1''}{X_1} = -\beta^2 \quad \frac{Z_1''}{Z_1} = -\eta^2$$

then,

$$\frac{X_1''}{X_1} = M^2 + \eta^2 \quad (\text{B.4})$$

and the solution for Eqn. B.4 is:

$$X_1(X) = C_1 \cosh[\sqrt{(M^2 + \eta^2)}X] + C_2 \sinh[\sqrt{(M^2 + \eta^2)}X] \quad (\text{B.5})$$

On the other hand, for the variable  $Z_1$ , we have

$$\frac{Z_1''}{Z_1} = -\eta^2 \quad (\text{B.6})$$

and its solution is,

$$Z_1(Z) = C_3 \cos \eta Z + C_4 \sin \eta Z \quad (\text{B.7})$$

Substituting Eqn. B.5 and B.7 in Eqn. B.2, the general solution is found.

$$\Psi(X, Z) = \{C_1 \cosh[\sqrt{(M^2 + \eta^2)}X] + C_2 \sinh[\sqrt{(M^2 + \eta^2)}X]\} \{C_3 \cos \eta Z + C_4 \sin \eta Z\} \quad (\text{B.8})$$

To know the value of the constants of Eqn. B.8, the boundary conditions are applied. Starting with the B.C. at  $Z=0$  ( $\Psi=0$ );

$$0 = \{C_1 \cosh[\sqrt{(M^2 + \eta^2)}X] + C_2 \sinh[\sqrt{(M^2 + \eta^2)}X]\} \{C_3 \cos(0) + C_4 \sin(0)\}$$

$$\therefore C_3 = 0$$

At the boundary  $z=t/L$ ,  $\Psi=0$ ;

$$0 = \{C_1 \cosh[\sqrt{(M^2 + \eta^2)}X] + C_2 \sinh[\sqrt{(M^2 + \eta^2)}X]\} \{C_4 \sin \eta(\frac{t}{L})\}$$

As  $C_4 \neq 0$ ,  $\sin \eta(\frac{t}{L})=0$ . So, this is the eigenfunction. From this equation, the eigenvalues of the equations are obtained. These are,

$$\eta_n = \frac{Ln\pi}{t} \quad (\text{B.9})$$

The third boundary condition, at  $X=1$ , defines an adiabatic condition. So,

$\frac{\partial \Psi}{\partial X} = 0$ . Deriving Eqn. B.8 and substituting the corresponding values;

$$0 = \sqrt{(M^2 + \eta_n^2)} C_1 \sinh[\sqrt{(M^2 + \eta_n^2)}] + \sqrt{(M^2 + \eta_n^2)} C_2 \cosh[\sqrt{(M^2 + \eta_n^2)}] \quad (\text{B.10})$$

One of the constants of Eqn. B.10 can be expressed as a function of the other one;

$$C_2 = -C_1 \tanh[\sqrt{(M^2 + \eta_n^2)}]$$

Substituting the values of the constants  $C_2$  and  $C_3$  in Eqn. B.8 and gathering the values of the constants  $C_1$  and  $C_4$  as one in  $C_n$ ,

$$\Psi(X, Z) = \sum_{n=0}^{\infty} C_n \{ \cosh[\sqrt{(M^2 + \eta_n^2)} X] - \tanh[\sqrt{(M^2 + \eta_n^2)}] \sinh[\sqrt{(M^2 + \eta_n^2)} X] \} \sin \eta_n Z \quad (\text{B.11})$$

Applying boundary condition at  $X=0$  ( $\Psi=1$ ),

$$1 = \sum_{n=0}^{\infty} C_n \sin \eta_n Z$$

Applying orthogonality:

$$\int_0^{\frac{t}{L}} \sin \eta_n Z dZ = C_n \int_0^{\frac{t}{L}} \sin^2 \eta_n Z dZ$$

Solving to find the coefficient  $C_n$ , and applying the respective integration limits, it is found that,

$$C_n = \frac{2(1 - (-1)^n)}{n\pi}$$

Finally, the solution for the first model generated by superposition is obtained.

$$\Psi(X, Z) = \sum_{n=1}^{\infty} \frac{2(1 - (-1)^n)}{n\pi} \left\{ \cosh \left[ \sqrt{\left( M^2 + \frac{L^2 n^2 \pi^2}{t^2} \right)} X \right] - \tanh \left[ \sqrt{\left( M^2 + \frac{L^2 n^2 \pi^2}{t^2} \right)} \right] \sinh \left[ \sqrt{\left( M^2 + \frac{L^2 n^2 \pi^2}{t^2} \right)} X \right] \right\} \sin \left[ \frac{Ln\pi}{t} Z \right] \quad (\text{B.12})$$

The second equation generated in the substitution of Eqn. 3.36 into Eqn. 3.31 is Eqn. B.13. It corresponds to the second model shown in Figure 3.8

$$\frac{\partial^2 \Phi}{\partial X^2} + \frac{\partial^2 \Phi}{\partial Z^2} - M^2 \Phi = 0 \quad (\text{B.13})$$

Applying separation of variables:

$$\Phi(X, Z) = X_2(X)Z_2(Z) \quad (\text{B.14})$$

Substituting Eqn. B.14 in Eqn. B.13:

$$X_2''Z_2 + X_2Z_2'' - M^2X_2Z_2 = 0$$

Dividing by  $X_2Z_2$

$$\frac{X_2''}{X_2} + \frac{Z_2''}{Z_2} - M^2 = 0 \quad (\text{B.15})$$

The terms of Eqn. B.15 can be defined as;

$$\begin{array}{lll} \frac{X_2''}{X_2} = -\gamma^2 & \frac{Z_2''}{Z_2} = -\alpha^2 & -\gamma^2 - \alpha^2 - M^2 = 0 \\ & & -\alpha^2 = M^2 + \gamma^2 \end{array}$$

The same procedure used with the first part is followed and a general solution for Eqn. B.13 is given by Eqn. B.16.

$$\Phi(X, Z) = \{C_1 \cos \gamma X + C_2 \sin \gamma X\} \{C_3 \cosh[\sqrt{(M^2 + \gamma^2)}Z] + C_4 \sinh[\sqrt{(M^2 + \gamma^2)}Z]\} \quad (\text{B.16})$$

Applying the boundary conditions at  $X=0$  and at  $X=1$ , the eigenfunction  $\cos \gamma = 0$  and eigenvalues  $\gamma_n = \pi \left( n + \frac{1}{2} \right)$  of the solution are obtained.

Applying the boundary condition at  $Z=0$ ,

$$\Phi(X, Z) = \sum_{n=0}^{\infty} C_n \sin \gamma_n X \sinh[\sqrt{(M^2 + \gamma_n^2)} Z] \quad (\text{B.17})$$

where the constant  $C_n$  gathers the initial constants  $C_2$  and  $C_4$ .

Applying boundary condition at  $z=t$ , ( $Z=\frac{t}{L}$ )

$$1 - X = \sum_{n=0}^{\infty} C_n \sin \gamma_n X \sinh \left[ \sqrt{(M^2 + \gamma_n^2)} \left( \frac{t}{L} \right) \right] \quad (\text{B.18})$$

Orthogonality is then applied to Eqn. B.18

$$\int_0^1 \sin \gamma_m X dX - \int_0^1 X \sin \gamma_m X dX = C_n \int_0^1 \sin^2 \gamma_n X \sinh \left[ \sqrt{(M^2 + \gamma_n^2)} \left( \frac{t}{L} \right) \right] dX \quad (\text{B.19})$$

Integrating all the terms that compose Eqn. B.19 and applying the limit values to each one of them, it is possible to find the value of the constant  $C_n$ .

$$C_n = \frac{1 - \frac{(-1)^n}{\pi \left(n + \frac{1}{2}\right)}}{\sinh \left[ \sqrt{\left(M^2 + \pi^2 \left(n + \frac{1}{2}\right)^2\right) \left(\frac{t}{L}\right)} \right] \left[ \frac{\pi}{2} \left(n + \frac{1}{2}\right) \right]}$$

Substituting the value of  $C_n$  into Eqn. B.17;

$$\Phi(X, Z) = \sum_{n=0}^{\infty} \frac{1 - \frac{(-1)^n}{\pi \left(n + \frac{1}{2}\right)}}{\sinh \left[ \sqrt{\left(M^2 + \pi^2 \left(n + \frac{1}{2}\right)^2\right) \left(\frac{t}{L}\right)} \right] \left[ \frac{\pi}{2} \left(n + \frac{1}{2}\right) \right]} \sin \left[ \pi \left(n + \frac{1}{2}\right) X \right] \sinh \left[ \sqrt{\left(M^2 + \pi^2 \left(n + \frac{1}{2}\right)^2\right) Z} \right]$$

(B.20)

The final solution for the dimensionless temperature for this case is given as,

$$\theta_{fm}(x, z) = \sum_{n=0}^{\infty} \frac{2(1 - (-1)^n)}{n\pi} \left\{ \cosh \left[ \sqrt{\left(M^2 + \frac{L^2 n^2 \pi^2}{t^2}\right) X} \right] - \tanh \left[ \sqrt{\left(M^2 + \frac{L^2 n^2 \pi^2}{t^2}\right)} \right] \sinh \left[ \sqrt{\left(M^2 + \frac{L^2 n^2 \pi^2}{t^2}\right) X} \right] \right\} \sin \left[ \frac{Ln\pi}{t} Z \right] +$$

$$\frac{1 - \frac{(-1)^n}{\pi \left(n + \frac{1}{2}\right)}}{\sinh \left[ \sqrt{\left(M^2 + \pi^2 \left(n + \frac{1}{2}\right)^2\right) \left(\frac{t}{L}\right)} \right] \left[ \frac{\pi}{2} \left(n + \frac{1}{2}\right) \right]} \sin \left[ \pi \left(n + \frac{1}{2}\right) X \right] \sinh \left[ \sqrt{\left(M^2 + \pi^2 \left(n + \frac{1}{2}\right)^2\right) Z} \right]$$

(B.21)

## Case 2. Temperature distribution with exponential behavior

As we mentioned in the main part of this document, and observing Figure 3.9, the first individual model corresponds to the solution of the Eqn.B.1, which was given above. We focus then in the solution of the second individual model, which follows a behavior again Eqn. B.13 but, as we know, the boundary condition at  $z=t$  is different now. So, applying separation of variables:

$$\Phi(X,Z) = X_2(X)Z_2(Z)$$

Substituting the last equation inn Eqn. B.13:

$$X_2''Z_2 + X_2Z_2'' - M^2X_2Z_2 = 0$$

Dividing by  $X_2Z_2$

$$\frac{X_2''}{X_2} + \frac{Z_2''}{Z_2} - M^2 = 0$$

Two individuals differential equations are generated;

$$\frac{X_2''}{X_2} = -\gamma^2 \qquad \frac{Z_2''}{Z_2} = -\alpha^2$$

Solving the last equations, a general solution for Eqn. B.13 is founded and given by,

$$\Phi(X, Z) = \{C_1 \cos \gamma X + C_2 \sin \gamma X\} \{C_3 \cosh[\sqrt{(M^2 + \gamma^2)}Z] + C_4 \sinh[\sqrt{(M^2 + \gamma^2)}Z]\}$$

Applying the boundary conditions at  $X=0$  and at  $X=1$ , the eigenfunction  $\cos \gamma = 0$  and eigenvalues  $\gamma_n = \pi \left( n + \frac{1}{2} \right)$  of the solution are obtained.

Applying the boundary condition at  $Z=0$ ,

$$\Phi(X, Z) = \sum_{n=0}^{\infty} C_n \sin \gamma_n X \sinh[\sqrt{(M^2 + \gamma_n^2)}Z]$$

where the constant  $C_n$  gathers the initial constants  $C_2$  and  $C_4$ .

Applying boundary condition at  $z=t$ , ( $Z=\frac{t}{L}$ )

$$\frac{(e^{1-X} - 1)}{(e - 1)} = \sum_{n=0}^{\infty} C_n \sin \gamma_n X \sinh \left[ \sqrt{(M^2 + \gamma_n^2)} \left( \frac{t}{L} \right) \right] \quad (\text{B.22})$$

Orthogonality is then applied to Eqn. B.22

$$\int_0^1 \frac{e^{1-X} - 1}{e-1} \sin \gamma_m X dX = \int_0^1 \sum_{n=0}^{\infty} C_n \sin^2 \gamma_n X \sinh \left[ \sqrt{(M^2 + \gamma_n^2)} \left( \frac{t}{L} \right) \right]$$

$$\frac{1}{e-1} \int_0^1 (e^{1-X} \sin \gamma_m X - \sin \gamma_m X) dX = C_n \sinh \left[ \sqrt{(M^2 + \gamma_n^2)} \left( \frac{t}{L} \right) \right] \int_0^1 \sin^2 \gamma_n X dX \quad (\text{B.23})$$

Integrating all the terms that compose Eqn. B.23 and applying the limit values to each one of them, it is possible to find the value of the constant  $C_n$ .

$$C_n = \frac{\frac{2}{e-1} \left\{ \frac{1}{\pi^2 \left( n + \frac{1}{2} \right)^2 + 1} \left[ e\pi \left( n + \frac{1}{2} \right) - (-1)^n \right] - \frac{1}{\pi \left( n + \frac{1}{2} \right)} \right\}}{\sinh \left[ \sqrt{(M^2 + \pi^2 \left( n + \frac{1}{2} \right)^2)} \left( \frac{t}{L} \right) \right]}$$

Substituting the value of  $C_n$ ;

$$\Phi(X, Z) = \sum_{n=0}^{\infty} \frac{\frac{2}{e-1} \left\{ \frac{1}{\pi^2 \left( n + \frac{1}{2} \right)^2 + 1} \left[ e\pi \left( n + \frac{1}{2} \right) - (-1)^n \right] - \frac{1}{\pi \left( n + \frac{1}{2} \right)} \right\}}{\sinh \left[ \sqrt{(M^2 + \pi^2 \left( n + \frac{1}{2} \right)^2)} \left( \frac{t}{L} \right) \right]} \sin \left[ \pi \left( n + \frac{1}{2} \right) X \right] \sinh \left[ \sqrt{(M^2 + \pi^2 \left( n + \frac{1}{2} \right)^2)} Z \right]$$

(B.24)

The final solution for the exponential variation case is given as,

$$\theta_{f_m}(x, z) = \sum_{n=0}^{\infty} \frac{2(1-(-1)^n)}{n\pi} \left\{ \cosh \left[ \sqrt{\left( M^2 + \frac{L^2 n^2 \pi^2}{t^2} \right)} X \right] - \tanh \left[ \sqrt{\left( M^2 + \frac{L^2 n^2 \pi^2}{t^2} \right)} \right] \sinh \left[ \sqrt{\left( M^2 + \frac{L^2 n^2 \pi^2}{t^2} \right)} X \right] \right\} \sin \left[ \frac{Ln\pi}{t} Z \right] +$$

$$+ \frac{2}{e-1} \left\{ \frac{1}{\pi^2 \left( n + \frac{1}{2} \right)^2 + 1} \left[ e^{\pi \left( n + \frac{1}{2} \right)} - (-1)^n \right] - \frac{1}{\pi \left( n + \frac{1}{2} \right)} \right\} \frac{\sin \left[ \pi \left( n + \frac{1}{2} \right) X \right] \sinh \left[ \sqrt{\left( M^2 + \pi^2 \left( n + \frac{1}{2} \right)^2 \right)} Z \right]}{\sinh \left[ \sqrt{\left( M^2 + \pi^2 \left( n + \frac{1}{2} \right)^2 \right)} \left( \frac{L}{t} \right) \right]}$$

(B.25)

**Case 3. Temperature distribution for a one dimensional model of Dukhan and Quiñones**

It case present same conditions as last one, this is, the first individual model shown in Figure 3.10 corresponds to the solution of the Eqn.B.1, which was derivated in the first case. Again, we will show how was obtained the solution of the second individual model with the third boundary condition. Applying separation of variables:

$$\Phi(X, Z) = X_2(X)Z_2(Z)$$

Substituting the last equation inn Eqn. B.13:

$$X_2'' Z_2 + X_2 Z_2'' - M^2 X_2 Z_2 = 0$$

Dividing by  $X_2 Z_2$

$$\frac{X_2''}{X_2} + \frac{Z_2''}{Z_2} - M^2 = 0$$

Two individual differential equations are generated;

$$\frac{X_2''}{X_2} = -\gamma^2 \qquad \frac{Z_2''}{Z_2} = -\alpha^2$$

Solving the last equations, a general solution for Eqn. B.13 is founded and given by,

$$\Phi(X, Z) = \{C_1 \cos \gamma X + C_2 \sin \gamma X\} \{C_3 \cosh[\sqrt{(M^2 + \gamma^2)}Z] + C_4 \sinh[\sqrt{(M^2 + \gamma^2)}Z]\}$$

Applying the boundary conditions at  $X=0$  and at  $X=1$ , the eigenfunction  $\cos \gamma = 0$  and eigenvalues  $\gamma_n = \pi \left( n + \frac{1}{2} \right)$  of the solution are obtained.

Applying the boundary condition at  $Z=0$ ,

$$\Phi(X, Z) = \sum_{n=0}^{\infty} C_n \sin \gamma_n X \sinh[\sqrt{(M^2 + \gamma_n^2)}Z]$$

where the constant  $C_n$  gathers the initial constants  $C_2$  and  $C_4$ .

Applying boundary condition at  $z=t$ , ( $Z=\frac{t}{L}$ )

$$\frac{\cosh M(1-X)}{\cosh M} = \sum_{n=0}^{\infty} C_n \sin \gamma_n X \sinh \left[ \sqrt{(M^2 + \gamma_n^2)} \left( \frac{t}{L} \right) \right] \quad (\text{B.26})$$

Orthogonality is then applied to Eqn. B.26

$$\frac{1}{\cosh M} \int_0^1 \cosh M(1-X) \sin \gamma_m X dX = C_n \sinh \left[ \sqrt{(M^2 + \gamma_n^2)} \left( \frac{t}{L} \right) \right] \int_0^1 \sin^2 \gamma_n X dX \quad (\text{B.27})$$

Integrating all the terms that compose Eqn. B.27 and applying the limit values to each one of them, it is possible to find the value of the constant  $C_n$ .

$$C_n = \frac{2 \left[ \pi \left( n + \frac{1}{2} \right) \right]}{\left( \pi^2 \left( n + \frac{1}{2} \right)^2 + M^2 \right) \sinh \left[ \sqrt{\left( M^2 + \pi^2 \left( n + \frac{1}{2} \right)^2 \right)} \left( \frac{t}{L} \right) \right]}$$

Substituting the value of  $C_n$ ;

$$\Phi(X, Z) = \sum_{n=0}^{\infty} \frac{2 \left[ \pi \left( n + \frac{1}{2} \right) \right]}{\left( \pi^2 \left( n + \frac{1}{2} \right)^2 + M^2 \right) \sinh \left[ \sqrt{\left( M^2 + \pi^2 \left( n + \frac{1}{2} \right)^2 \right)} \left( \frac{t}{L} \right) \right]} \sin \left[ \pi \left( n + \frac{1}{2} \right) X \right] \sinh \left[ \sqrt{\left( M^2 + \pi^2 \left( n + \frac{1}{2} \right)^2 \right)} Z \right] \quad (\text{B.28})$$

The final solution for the exponential variation case is given as,

$$\theta(X, Z) = \sum_{n=0}^{\infty} \frac{2(1-(-1)^n)}{n\pi} \left\{ \cosh \left[ \sqrt{\left( M^2 + \frac{L^2 n^2 \pi^2}{t^2} \right)} X \right] - \tanh \left[ \sqrt{\left( M^2 + \frac{L^2 n^2 \pi^2}{t^2} \right)} \right] \sinh \left[ \sqrt{\left( M^2 + \frac{L^2 n^2 \pi^2}{t^2} \right)} X \right] \right\} \sin \left[ \frac{Ln\pi}{t} Z \right] +$$

$$+ \frac{2 \left[ \pi \left( n + \frac{1}{2} \right) \right]}{\left( \pi^2 \left( n + \frac{1}{2} \right)^2 + M^2 \right) \sinh \left[ \sqrt{\left( M^2 + \pi^2 \left( n + \frac{1}{2} \right)^2 \right)} \left( \frac{t}{L} \right) \right]} \sin \left[ \pi \left( n + \frac{1}{2} \right) X \right] \sinh \left[ \sqrt{\left( M^2 + \pi^2 \left( n + \frac{1}{2} \right)^2 \right)} Z \right]$$

(B.29)

#### **Case 4. Temperature distribution with zero-slope**

As observed from Figure 3.11, for this case it is not necessary to use superposition principle. The method of separation of variables is directly used since it case presents only one non-homogenous boundary condition. So,

$$\theta_{fm}(X, Z) = \chi(X)\kappa(Z) \tag{B.30}$$

Substituting Eqn. B.30 into Eqn. 3.14,

$$\chi''\kappa + \chi\kappa'' - M^2\chi\kappa = 0$$

Dividing by  $XZ$

$$\frac{\chi''}{\chi} + \frac{\kappa''}{\kappa} - M^2 = 0 \quad (\text{B.31})$$

The terms of Eqn. B.31 can be defined as:

$$\frac{\chi''}{\chi} = -\beta^2 \quad \frac{\kappa''}{\kappa} = -\eta^2 \quad \begin{aligned} -\beta^2 - \eta^2 - M^2 &= 0 \\ -\beta^2 &= M^2 + \eta^2 \end{aligned}$$

Substituting the above constants in the Eqn. B.31, Eqn. B.32 is obtained.

$$\frac{\chi''}{\chi} = M^2 + \eta^2 \quad (\text{B.32})$$

The general solution of equation B.32 is:

$$\chi(X) = C_1 \cosh[\sqrt{(M^2 + \eta^2)}X] + C_2 \sinh[\sqrt{(M^2 + \eta^2)}X] \quad (\text{B.33})$$

Solution for variable  $\kappa$  of Eqn. B.30 is obtained by solving Eqn. B.34.

$$\frac{\kappa''}{\kappa} = -\eta^2 \quad (\text{B.34})$$

Solution of Eqn. B.34 has the form of Eqn. B.35.

$$\kappa(Z) = C_3 \cos \eta Z + C_4 \sin \eta Z \quad (\text{B.35})$$

A solution for  $\theta_{fm}$  employing Eqn. B.33 and B.35 is given by Eqn. B.36.

$$\theta_{fm}(X, Z) = \{C_1 \cosh[\sqrt{(M^2 + \eta^2)}X] + C_2 \sinh[\sqrt{(M^2 + \eta^2)}X]\} \{C_3 \cos \eta Z + C_4 \sin \eta Z\} \quad (\text{B.36})$$

The boundary conditions at  $Z=0$  and  $Z=\frac{t}{L}$  are applied to the Eqn. B.36. The eigenfunction and eigenvalues of the solution are obtained and defined by Eqn. B.37 and Eqn. B.38.

$$\cos \eta \left(\frac{t}{L}\right) = 0 \quad \text{eigen function} \quad (\text{B.37})$$

$$\eta_n = \frac{L\pi}{t} \left(n + \frac{1}{2}\right) \quad \text{eigen values} \quad (\text{B.38})$$

The boundary condition at  $X=1$  is applied next. Once that is done, a general solution that describes the dimensionless temperature inside the foam under this proposed conditions is obtained and is given by Eqn. B.39.

$$\theta_{fm}(X, Z) = \sum_{n=0}^{\infty} C_n \{ \cosh[(M^2 + \eta_n^2)X] - \tanh[(M^2 + \eta_n^2)] \sinh[(M^2 + \eta_n^2)X] \} \sin \eta_n Z \quad (\text{B.39})$$

Finally, the last boundary condition is applied ( $X=0$ ). Orthogonality theorem is applied to find the value of the constant  $C_n$ . When this is made, the constant is substituted in Eqn. 3.71 and the final solution for this fourth case is obtained and is expressed by Eqn. B.40.

$$\theta_{jm}(X, Z) = \sum_{n=0}^{\infty} \frac{2}{\pi \left(n + \frac{1}{2}\right)} \left\{ \cosh \left[ \sqrt{M^2 + \frac{L^2 \pi^2 \left(n + \frac{1}{2}\right)^2}{t^2}} X \right] - \tanh \left[ \sqrt{M^2 + \frac{L^2 \pi^2 \left(n + \frac{1}{2}\right)^2}{t^2}} \right] \sinh \left[ \sqrt{M^2 + \frac{L^2 \pi^2 \left(n + \frac{1}{2}\right)^2}{t^2}} X \right] \right\} \sin \left[ \frac{L \pi \left(n + \frac{1}{2}\right)}{t} Z \right]$$

(B.40)